PLASMA-ASSISTED ATOMIC LAYER DEPOSITION OF III-NITRIDE THIN FILMS

A DISSERTATION SUBMITTED TO
MATERIALS SCIENCE AND NANOTECHNOLOGY PROGRAM
OF THE GRADUATE SCHOOL OF ENGINEERING AND SCIENCE
OF BILKENT UNIVERSITY
IN PARTIAL FULFILLMENT OF THE REQUIREMENTS
FOR THE DEGREE OF
DOCTOR OF PHILOSOPHY

By
Çağla Özgit-Akgün
February, 2014

I certify that I have read this thesis and that in my opinion it is fully adequate, in scope and in quality, as a dissertation for the degree of Doctor of Philosophy.

Assist. Prof. Dr. Necmi Bıyıklı (Advisor)

I certify that I have read this thesis and that in my opinion it is fully adequate, in scope and in quality, as a dissertation for the degree of Doctor of Philosophy.

Assist. Prof. Dr. Ali Kemal Okyay

I certify that I have read this thesis and that in my opinion it is fully adequate, in scope and in quality, as a dissertation for the degree of Doctor of Philosophy.

Prof. Dr. Macit Özenbaş

I certify that I have read this thesis and that in my opinion it is fully adequate, in scope and in quality, as a dissertation for the degree of Doctor of Philosophy.

Assoc. Prof. Dr. Mehmet Bayındır

I certify that I have read this thesis and that in my opinion it is fully adequate, in scope and in quality, as a dissertation for the degree of Doctor of Philosophy.

Prof. Dr. Raşit Turan

Approved for the Graduate School of Engineering and Science:

Prof. Dr. Levent Onural
Director of the Graduate School

ABSTRACT

PLASMA-ASSISTED ATOMIC LAYER DEPOSITION OF III-NITRIDE THIN FILMS

Çağla Özgit-Akgün
Ph.D. in Materials Science and Nanotechnology
Supervisor: Assist. Prof. Dr. Necmi Bıyıklı
February, 2014

III-nitride compound semiconductors and their alloys have emerged as versatile and high-performance materials for a wide range of electronic and optoelectronic device applications. Besides possessing very unique material properties individually, members of the III-nitride family with wurtzite (hexagonal) crystal structure also exhibit direct band gaps, which cover a wide range with values of 6.2, 3.4 and 0.64 eV for AlN, GaN and InN, respectively. In this respect, ternary and quaternary alloys of this family are particularly important since their bandgaps can easily be tuned by adjusting the alloy composition. Although high quality III-nitride thin films can be grown at high temperatures (>1000 °C) with significant rates, deposition of these films on temperature-sensitive device layers and substrates necessitates the adaptation of low-temperature methods such as atomic layer deposition (ALD). ALD is a special type of chemical vapor deposition, in which the substrate surface is exposed to sequential pulses of two or more precursors separated by purging periods. When compared to other low-temperature thin film deposition techniques, ALD stands out with its self-limiting growth mechanism, which enables the deposition of highly uniform and conformal thin films with sub-angstrom thickness control. Moreover, alloy thin films can be easily deposited by ALD, where film composition is digitally controlled by the relative number of subcycles.

In this thesis, we report on the development of plasma-assisted ALD (PA-ALD) processes for III-nitrides, and present detailed characterization results for the deposited thin films and fabricated nanostructures. PA-ALD of polycrystalline wurtzite AlN thin films was realized at temperatures ranging from 100-500 °C using trimethylaluminum ($AlMe_3$) as the Al precursor. Films deposited at temperatures within the ALD window (100-200 °C for both ammonia (NH_3) and N_2/H_2 plasma processes) were C-free and had relatively low O concentrations

(<3 at.%). We also demonstrated the conformality of $AlMe_3$-NH_3 plasma process by fabricating high surface area AlN hollow nanofibers using electrospun nylon nanofiber mats as sacrificial templates. Our initial efforts for depositing GaN and InN resulted in thin films with high O concentrations. Although - at first - the most probable source of this contamination was presumed as the O-containing impurities in the unpurified 5N-grade NH_3 gas, subsequent experiments revealed the true source as the quartz tube of inductively coupled RF-plasma (ICP) source itself. In view of these circumstances, the choice of N-containing plasma gas (NH_3, N_2/H_2 or N_2) determined the severity of O incorporation into AlN and GaN films deposited by PA-ALD. As an effort to completely avoid this plasma-related oxygen contamination problem, we replaced the original quartz-based ICP source of the ALD system with a stainless steel hollow cathode plasma (HCP) source. Thereby we demonstrated the low-temperature hollow cathode PA-ALD (HCPA-ALD) of crystalline AlN, GaN and $Al_xGa_{1-x}N$ thin films with low impurity concentrations (O, C <1 at.%) using $AlMe_3$ and trimethylgallium ($GaMe_3$) as the Al and Ga precursors, respectively. Optical band edge values of the $Al_xGa_{1-x}N$ films shifted to lower wavelengths with the increasing Al content, indicating the tunability of band edge values with alloy composition. HCPA-ALD of InN was also investigated within the scope of this study. Initial results revealed the possibility to obtain single-phase wurtzite InN thin films using cyclopentadienyl indium (CpIn) as the In precursor.

Keywords: atomic layer deposition, aluminum nitride, gallium nitride, indium nitride, thin film, digital alloying, plasma-related oxygen contamination, inductively coupled plasma, hollow cathode plasma, hollow nanofiber, template-based synthesis, trimethylaluminum, triethylgallium, trimethylgallium, trimethylindium, cyclopentadienyl indium, ammonia, nitrogen, hydrogen.

ÖZET

III-NİTRÜR İNCE FİLMLERİN PLAZMA-DESTEKLİ ATOMİK KATMAN BİRİKTİRME YÖNTEMİ İLE BÜYÜTÜLMESİ

Çağla Özgit-Akgün
Malzeme Bilimi ve Nanoteknoloji, Doktora
Tez Yöneticisi: Yrd. Doç. Dr. Necmi Bıyıklı
Şubat, 2014

III-nitrür bileşik yarı iletkenler ve alaşımları geniş bir elektronik ve optoelektronik cihaz uygulama yelpazesi için çok yönlü ve yüksek performanslı malzemeler olarak ortaya çıkmıştır. Ayrı ayrı çok benzersiz malzeme özelliklerine sahip olmalarının yanı sıra, III-nitrür ailesinin vürtzit (hekzagonal) kristal yapıya sahip üyeleri, AlN, GaN ve InN için sırasıyla 6.2, 3.4 ve 0.64 eV olan değerlerle geniş bir mezili kapsayan direkt bant aralıkları sergilerler. Bu bakımdan, bu ailenin üçlü ve dörtlü alaşımları, bant aralıkları alaşım bileşimi ile kolayca ayarlanabildiği için, özellikle önemlidir. Yüksek kaliteli III-nitrür ince filmler yüksek sıcaklıklarda (>1000 °C) kayda değer hızlar ile büyütülebiliyor olsada, bu filmlerin sıcaklığa duyarlı cihaz katmanları ve alttaşlar üzerine biriktirilmesi atomik katman biriktirme (AKB) gibi düşük sıcaklıklarda gerçekleşen yöntemlerin adaptasyonunu gerektirmektedir. AKB, alttaş yüzeyinin iki ya da daha çok öncü maddenin arındırma periyotları ile ayrılmış ardışık atımlarına maruz bırakıldığı özel bir kimyasal buhar biriktirme türüdür. Diğer düşük sıcaklık ince film biriktirme teknikleriyle karşılaştırıldığında, AKB, son derece muntazam ve konformal ince filmlerin angstrom-altı kalınlık kontrolü ile biriktirilmesini sağlayan, kendi kendini sınırlayan büyütme mekanizması ile dikkat çeker. Üstelik, film bileşiminin alt döngülerin nispi sayısı ile dijital olarak kontrol edildiği alaşım ince filmler de AKB ile kolayca biriktirilebilmektedir.

Bu tezde, III-nitrürler için plazma-destekli AKB (PD-AKB) işlemlerinin geliştirilmesini rapor etmekte, biriktirilen ince filmler ve üretilen nanoyapılar için detaylı karakterizasyon sonuçları sunmaktayız. Polikristal vürtzit AlN ince filmlerin PD-AKB yöntemi ile büyütülmesi 100 ile 500 °C arasında değişen sıcaklıklarda, trimetilalüminyum ($AlMe_3$) kullanılarak gerçekleştirilmiştir. AKB penceresi içerisinde kalan sıcaklıklarda (amonyak (NH_3) ve N_2/H_2 plazma

işlemlerinin her ikisi için de 100-200 °C) büyütülen filmlerin karbonsuz olduğu ve nispeten düşük O konsantrasyonları (<3 at.%) içerdiği belirlenmiştir. $AlMe_3$-NH_3 plazma işleminin konformalitesi, elektro lif çekimi yöntemi ile elde edilmiş naylon nanolif matrislerin tükenir şablonlar şeklinde kullanılmasıyla üretilen yüksek yüzey alanına sahip içi boş AlN nanolifler aracılığıyla gösterilmiştir. GaN ve InN biriktirmek için gösterdiğimiz ilk çabalar yüksek O konsantrasyonlarına sahip ince filmler ile sonuçlanmıştır. Başta bu bulaşımın en olası kaynağı, daha ileri bir saflaştırma işlemine tabi tutulmadan kullanılan 5N kaliteye sahip NH_3 gazındaki O içeren safsızlıklar olarak varsayılmış olsada, daha sonraki deneyler gerçek kaynağın endüktif eşleşmiş RF-plazma (EEP) kaynağında bulunan kuvars tüp olduğunu ortaya koymuştur. Bu şartlar altında, N içeren plazma gazının (NH_3, N_2/H_2 ya da N_2) seçimi oksijenin PD-AKB ile biriktirilmiş AlN ve GaN filmlerin içine dahil olma şiddetini belirlemiştir. Plazmaya bağlı oksijen bulaşımını tamamen engelleme çabası olarak, AKB sisteminin orijinal kuvars esaslı EEP kaynağı paslanmaz çelik oyuk katod plazma (OKP) kaynağı ile değiştirilmiş; bu sayede düşük safsızlık konsantrasyonlarına (O, C <1 at.%) sahip AlN, GaN ve $Al_xGa_{1-x}N$ kristal ince filmler $AlMe_3$ ve trimetilgalyum ($GaMe_3$) kullanılarak düşük sıcaklıklarda oyuk katod PD-AKB (OKPD-AKB) yöntemi ile büyütülmüştür. $Al_xGa_{1-x}N$ filmlerin optik bant kenarı değerlerinin artan Al içeriği ile düşük dalga boylarına kayması bant kenarı değerlerinin alaşım bileşimi ile ayarlanabildiğini belirtmektedir. InN filmlerin OKPD-AKB ile büyütülmesi de bu çalışma kapsamında incelenmiş, elde edilen ilk sonuçlar siklopentadienil indiyum (CpIn) kullanılarak tek fazlı vürtzit InN ince filmlerin büyütülebilme ihtimali olduğunu ortaya çıkarmıştır.

Anahtar sözcükler: atomik katman biriktirme, alüminyum nitrür, galyum nitrür, indiyum nitrür, ince film, dijital alaşımlama, plazmaya bağlı oksijen bulaşımı, endüktif eşleşmiş plazma, oyuk katod plazma, içi boş nanolif, şablona dayalı sentez, trimetilalüminyum, trietilgalyum, trimetilgalyum, trimetilindiyum, siklopentadienil indiyum, amonyak, nitrojen, hidrojen.

Acknowledgement

First and foremost I would like to express my sincere gratitude to my supervisor Assist. Prof. Dr. Necmi Bıyıklı for his invaluable guidance, continuous support, motivation, and confidence throughout this research. He encouraged me to work in diverse research projects, which extended my knowledge and vision. I am also indebted to the members of my thesis committee, Assoc. Prof. Dr. Mehmet Bayındır, Assist. Prof. Dr. Ali Kemal Okyay, Prof. Dr. Macit Özenbaş, and Prof. Dr. Raşit Turan for their insightful comments.

My sincere gratitude goes to Dr. Ritwik Bhatia, Bob Kane and Dr. Mark Sowa from Ultratech/Cambridge Nanotech Inc., Dr. Eric Deguns from Oerlikon Leybold Vacuum USA Inc., and Dr. Scott Butcher from Meaglow Ltd. for sharing their expertise and extensive knowledge with willingness whenever needed.

I would like to thank our collaborators, Assoc. Prof. Dr. Aykutlu Dâna and Assist. Prof. Dr. Ali Kemal Okyay, and their students Sami Bolat, Feyza Bozkurt-Oruç, Deniz Kocaay, Ayşe Özcan, and Burak Tekcan for their efforts in the fabrication and characterization of charge-trapping flash memories, memristors, thin film transistors, and UV photodetectors using AlN and GaN thin films reported in this work. Gratitude extends to Assoc. Prof. Dr. Tamer Uyar and Fatma Kayacı not only for their collaboration in research projects where we combined electrospinning and ALD processes to produce novel materials, but also providing the electrospun nanofiber mats that have been used for the template-based synthesis of AlN hollow nanofibers.

Mustafa Güler and Mustafa Ürel are gratefully acknowledged for their help during TEM sample preparation and imaging, and AFM measurements, respectively. I would also like to thank Assoc. Prof. Dr. Mustafa Alevli and Dr. Eda Goldenberg for the optical transmission measurements. Many thanks to UCF engineers Fikret Piri and Semih Yaşar for their essential and generous support on technical issues related to the cleanroom and PA-ALD system.

I would also like to express my deep appreciation to the founder and former director of UNAM, Prof Dr. Salim Çıracı, who envisioned and established a world-class interdisciplinary research environment. I am very grateful for having the opportunity to work in the cleanroom facility and characterization laboratories, all of which equipped with the state-of-the-art equipments.

I am sincerely thankful to İnci Dönmez not only for her generous help and contributions during the first two years of this work, but also for her kind friendship. I could not have imagined a better collaborator.

Many thanks to the former members of the Bıyıklı Research Group, Engin Çağatay and M. Alican Noyan, former and current UNAM engineers Enver Kahveci, Mustafa K. Ruhi and Adem Saraç, as well as former and present residents of the Student Office Z-07, Fatih B. Atar, Levent Aygün, Temmuz Ceyhan, Furkan Çimen, Gürkan Polat, Ahmet D. Usta, and Alper Yeşilyurt for their friendship. I would also like to extend many thanks to Dr. Handan Acar, Dr. Can Ataca, O. Öner Ekiz, Merve Kaplan, Melis Şardan, Sıla Toksöz, and Adem Yıldırım.

Finally, I would like to thank my family and friends, especially to my parents and grandparents, for their love and support. I am especially grateful to two of my dearest friends, Dr. E. Ayşe Özşuca and Dr. Deniz Keçik - who were also Ph.D. students until recently - for the moral support they provided starting from the very beginning of this study. Very special thanks go to my husband, Barış Akgün, for his endless support, understanding and patience.

Financial support from TÜBİTAK BİDEB Ph.D. Fellowship Program is gratefully acknowledged.

To my family and friends.

Contents

1 Introduction **1**

2 Background **4**

2.1 Atomic Layer Deposition 4

2.1.1 Basic Principles 5

2.1.2 Selection of Precursors 8

2.1.3 Optimization of Deposition Parameters 10

2.1.4 Opportunities and Challenges 11

2.2 ALD of III-Nitride Thin Films 14

2.2.1 Aluminum Nitride Thin Films 14

2.2.2 Gallium Nitride Thin Films 16

2.2.3 Indium Nitride Thin Films 21

2.3 Template-Based Synthesis of Nanostructures via ALD: AlN Hollow Nanofibers 22

3 Experimental Details **25**

3.1 Preparation of Substrates 25

3.1.1 Planar Substrates 25

3.1.2 Nanofiber Templates Prepared by Electrospinning 25

3.2 Plasma-Assisted Atomic Layer Deposition of III-Nitride Thin Films 26

3.2.1 Precursors and Plasma Gases 26

3.2.2 The Reactor 27

3.2.3 Synthesis of AlN Hollow Nanofibers 29

3.3 Characterization Methods 30

3.3.1 Characterization of Thin Films 30

3.3.2 Characterization of AlN Hollow Nanofibers 35

4 Plasma-Assisted Atomic Layer Deposition of Aluminum Nitride Thin Films 36

4.1 Thermal ALD Using $AlMe_3$ and NH_3 37

4.2 PA-ALD Using $AlMe_3$ and NH_3 Plasma 38

4.2.1 Optimization of PA-ALD Parameters 38

4.2.2 Characterization of AlN Thin Films 41

4.2.3 Template-Based Synthesis of AlN Hollow Nanofibers 56

4.3 PA-ALD Using $AlMe_3$ and N_2/H_2 Plasma 65

4.3.1 Optimization of PA-ALD Parameters 65

4.3.2 Characterization of AlN Thin Films 67

5 The Indication of Plasma-Related Oxygen Contamination in III-Nitride Thin Films 71

5.1 PA-ALD of GaN Thin Films 72

5.1.1 PA-ALD Using $GaMe_3$ and NH_3 Plasma 72

5.1.2 PA-ALD Using $GaEt_3$ and NH_3 Plasma 79

5.2 PA-ALD of InN Thin Films 82

5.2.1 PA-ALD Using $InMe_3$ and NH_3 Plasma 82

5.2.2 PA-ALD Using CpIn and NH_3 Plasma 82

5.3 GaN and AlN Thin Films Deposited Using Purified NH_3, N_2/H_2 and N_2 Plasma Gases 83

5.3.1 GaN Thin Films 84

5.3.2 AlN Thin Films 86

6 Hollow Cathode Plasma-Assisted Atomic Layer Deposition of III-Nitride Thin Films 90

6.1 AlN and GaN Thin Films Deposited Using Non-Optimized HCPA-ALD Parameters 91

6.2 Optimization of HCPA-ALD Parameters 97

6.2.1 AlN Thin Films 97

6.2.2 GaN Thin Films 100

6.3 AlN and GaN Thin Films Deposited Using Optimized HCPA-ALD Parameters 101

6.4 AlN and GaN Thin Films Deposited Using N_2 Plasma 107

6.5 Deposition of $Al_xGa_{1-x}N$ Thin Films by Digital Alloying 110

6.6 HCPA-ALD of InN Thin Films 115

7 Conclusions and Future Work **122**

List of Figures

2.1 (a) Variation of GPC with the increasing dose of precursor molecules. ALD and CVD regimes are indicated on the figure. (b) GPC as a function of temperature. ALD window, in which the process satisfies the requirements of self-terminating surface reactions, is depicted on the figure. 7

2.2 The dependency of GPC on the number of ALD cycles reveals different types of growth behavior: (a) linear, (b) substrate-enhanced, and (c) substrate-inhibited. 8

2.3 Vapor pressures of the metalorganic precursors used in this study as a function of temperature. 9

3.1 Schematics of the Fiji F200-LL PA-ALD system. 27

3.2 Representative photographs of (a) quartz-based ICP, and (b) stainless steel HCP sources. 29

3.3 Schematic representation of the fabrication procedure for MIS capacitor structures. 33

3.4 Cross-sectional schematic representation of the resulting MIS capacitor structure. 35

4.1 Thermal ALD experiments, where no self-limiting growth behavior was observed. (a) GPC of AlN at different deposition temperatures (■). GPC as a function of $AlMe_3$ and NH_3 doses at 450 °C (△). (b) GPC as a function of purge time at 450 °C. $AlMe_3$ pulse length, NH_3 flow rate and duration were 0.1 s, 150 sccm and 20 s, respectively. Dashed line is for visual aid. 38

4.2 (a) Precursor saturation curves at 185 °C: NH_3 flow duration was kept constant at 20 s for the $AlMe_3$ saturation curve (■), and $AlMe_3$ pulse length was kept constant at 0.05 s for the NH_3 saturation curve (△). (b) GPC as a function of purge time: $AlMe_3$ pulse length and NH_3 flow duration were constant at 0.1 and 40 s, respectively. Dashed line is for visual aid. 39

4.3 (a) Deposition rates of AlN thin films at different temperatures. (b) $AlMe_3$ saturation curves at 185, 250, 350, and 450 °C, where NH_3 flow duration was kept constant at 40 s. (c) NH_3 saturation curves at 185 and 450 °C. Dashed line is for visual aid. 40

4.4 (a) Film thickness vs. number of deposition cycles. (b) GPC of AlN as a function of plasma power. AlN thin films were deposited at 185 °C. 42

4.5 (a) Compositional depth profile of ~100 nm thick AlN thin film. (b) O 1s, (c) Al 2p, and (d) N 1s HR-XPS scans. 43

4.6 GIXRD patterns of ~33 nm thick AlN thin films deposited on Si (100), Si (111), *c*-plane sapphire, MOCVD-grown GaN on *c*-plane sapphire, and glass substrates. GIXRD patterns indicate a hexagonal wurtzite crystal structure. 44

4.7 XRD pattern of ~500 nm thick AlN thin film deposited at 200 °C on Si (111) substrate. 45

4.8 (a) Cross-sectional TEM image of ~100 nm thick AlN thin film deposited at 185 °C on Si (100). (b), (c) Cross-sectional HR-TEM images, and (inset) SAED pattern of the same sample. (d) Cross-sectional HR-TEM image of AlN thin film deposited on glass substrate. 46

4.9 (a) 2D and (b) 3D AFM images of ~33 nm thick AlN thin film deposited at 185 °C on Si (100). (c) 2D and (d) 3D AFM images of ~100 nm thick AlN thin film deposited at 185 °C on Si (100). . 47

4.10 (a) Optical constants (refractive index and extinction coefficient) of ~100 nm thick AlN film deposited on Si (100). (b) Optical transmission spectrum of the film deposited on double side polished sapphire. (Inset) Absorption spectrum of the same sample. 48

4.11 (a), (b), (c) C-V characteristics of the MIS capacitor structures with ~7, ~14 and ~47 nm thick AlN insulating layers, respectively. (d) I-V characteristics of the MIS capacitor structures. . . . 50

4.12 Optical microscope images of the MIS capacitor structures with ~7 nm thick AlN as the insulating layer. 50

4.13 Al 2p HR-XPS scans of AlN thin films deposited at different temperatures; (a) $t_{etch} = 0$ s (i.e., film surface) (b) $t_{etch} = 300$ s. Binding energy values denoted on each figure correspond to the Al-N bonding state. Dashed lines are for visual aid. 53

4.14 GIXRD patterns of ~100 nm thick AlN films deposited on Si (100) substrates at different temperatures. 54

4.15 Crystallite sizes, thicknesses, mass densities, and roughnesses of AlN thin films as a function of deposition temperature. 55

4.16 (Left) Schematic representation of an ALD cycle. (Right) Template-based synthesis of inorganic hollow nanofibers; preparation of the nanofiber template by electrospinning, conformal deposition on electrospun nanofibers via PA-ALD, and removal of the organic template by calcination. 56

4.17 SEM images of electrospun Nylon 6,6 nanofiber templates having (a) 70 nm, (b) 330 nm, and (c) 740 nm average fiber diameters. . . 57

4.18 SEM images of (a) Nylon 6,6 nanofibers (average fiber diameter 740 nm) coated with 400 cycles AlN, and (b), (c) inorganic hollow nanofibers synthesized by the *ex situ* calcination of coated nanofibers. 58

4.19 SEM images of hollow nanofibers synthesized by depositing 800 cycles AlN on Nylon 6,6 templates having (a) 740 nm, (b) 330 nm, and (c) 70 nm average fiber diameters. AlN-coated fibers were calcined *in situ*. 59

4.20 SEM images of AlN hollow nanofibers taken at different magnifications. Hollow nanofibers were synthesized by the deposition of 800 cycles AlN on a Nylon 6,6 template having 330 nm average fiber diameter, followed by *ex situ* calcination at air ambient. . . . 60

4.21 AlN hollow nanofibers synthesized by the deposition of 800 cycles AlN, followed by *in situ* calcination. (a) Bright field TEM image of hollow nanofibers synthesized using Nylon 6,6 template having an average fiber diameter of 70 nm. (b)-(d) TEM images of hollow nanofibers synthesized using templates with average fiber diameters of 70, 330 and 740 nm, respectively. (e) HR-TEM image, and (f) SAED pattern of AlN hollow nanofibers synthesized using a template having 330 nm average fiber diameter. 61

4.22 (a) Al 2p and (b) N 1s HR-XPS scans of AlN hollow nanofibers synthesized by depositing 800 cycles AlN on Nylon 6,6 templates having 70 and 740 nm average fiber diameters, which was followed by *in situ* calcination. N 1s HR-XPS scan of bare Nylon 6,6 nanofiber template having an average fiber diameter of 70 nm is also included. 64

4.23 Al 2p HR-XPS scans of AlN hollow nanofibers synthesized by the deposition of 800 cycles AlN on Nylon 6,6 nanofiber templates (average fiber diameter 70 nm), followed by *in situ* and *ex situ* calcinations. 65

4.24 Optimization of PA-ALD process parameters for AlN using $AlMe_3$ and N_2/H_2 plasma as the group-III and -V sources, respectively. (a) GPC as a function of N_2 or H_2 flow rate. (b) $AlMe_3$ (■) and N_2/H_2 (△) saturation curves at 185 °C. (c) GPC values for AlN thin films deposited at different temperatures. (d) Film thickness vs. number of deposition cycles at 175 °C. 66

4.25 GIXRD patterns of AlN thin films deposited at 185 °C on Si (100) substrates using $AlMe_3$-NH_3 and $AlMe_3$-N_2/H_2 PA-ALD processes. 69

4.26 Cross-sectional HR-TEM images of ~84 nm thick AlN thin film deposited at 185 °C on Si (100) substrate using $AlMe_3$-N_2/H_2 PA-ALD process. 70

4.27 (a) 2D and (b) 3D AFM images of ~84 nm thick AlN thin film deposited at 185 °C on Si (100) using $AlMe_3$-N_2/H_2 PA-ALD process. 70

5.1 (a) $GaMe_3$ saturation curves at 185 °C for different $GaMe_3$ temperatures. NH_3 flow rate was constant at 50 sccm. Dashed lines are for visual aid. (b) NH_3 saturation curve at 185 °C. $GaMe_3$ pulse length was 0.015 s. 73

5.2 (a) GPC values for GaN thin films deposited at different temperatures. (b) GPC as a function of purge time at 185 °C. Dashed lines are for visual aid. 74

5.3 Film thickness vs. number of deposition cycles plot for GaN thin films deposited at 250 °C using $GaMe_3$ and NH_3 plasma. 75

5.4 Compositional depth profile of ~17 nm thick GaN thin film deposited at 250 °C. 76

5.5 Photograph of the quartz tube of ICP source, which was etched all the way through its wall thickness. 77

5.6 (a), (b) Cross-sectional HR-TEM images of ~42 nm thick GaN thin film deposited at 185 °C on Si (111) substrate. (c) GIXRD pattern of ~17 nm thick GaN thin film deposited at 250 °C on Si (100) substrate. 78

5.7 (a) $GaEt_3$ saturation curves at 150 and 250 °C. NH_3 flow rate and duration were constant at 50 sccm and 90 s, respectively. Purge time between the exposures was 10 s. (b) Deposition rate as a function of purge time. Dashed line is for visual aid. 80

5.8 (a) NH_3 saturation curve at 250 °C. $GaEt_3$ pulse length was constant at 0.5 s, purge time between the exposures was 10 s. (b) GPC values for GaN thin films deposited at different temperatures. . . . 80

5.9 Film thickness vs. number of deposition cycles plot for GaN thin films deposited at 150 °C using $GaEt_3$ and NH_3 plasma. 81

5.10 Ellipsometric spectra of the Si (111) substrate before and after the sequential $InMe_3$-NH_3 plasma depositions. The angle of incidence was 75°. 83

5.11 GIXRD pattern of a ~22 nm thick GaN thin film deposited at 200 °C by PA-ALD using $GaMe_3$ and N_2/H_2 plasma. 86

6.1 Photograph of a 81.5 nm thick AlN thin film deposited on 4 in. Si (100) substrate using $AlMe_3$ and NH_3 plasma. Wafer-level uniformity was measured as ±1.23%. 92

6.2 Impurity concentrations determined by SIMS depth profiling for (a) AlN, and (b) GaN thin films deposited using NH_3 plasma. Silicon is not quantified in the layers, only plotted as the substrate layer marker. 94

6.3 GIXRD patterns of (a) AlN, and (b) GaN thin films deposited on Si (100) substrates using NH_3 plasma. GIXRD pattern of the AlN thin film deposited using quartz-based ICP source is also shown in (a) for comparison. 95

6.4 Cross-sectional (a) TEM, and (b) HR-TEM images of 21 nm thick GaN thin film deposited on Si (100) substrate using NH_3 plasma. FIB-induced SiO_2 damage layer formed at the GaN/Si interface during TEM sample preparation. (c) SAED pattern of the same sample. 97

6.5 (a) $AlMe_3$, and (b) N_2/H_2 saturation curves at 200 °C. For the $AlMe_3$ saturation curve, N_2/H_2 flow rate and flow duration were kept constant at 50 + 50 sccm and 40 s, respectively. $AlMe_3$ pulse length was 0.06 s for the N_2/H_2 saturation curve. (c) AlN film thickness plotted as a function of number of deposition cycles. . . . 98

6.6 (a) $GaMe_3$, and (b) N_2/H_2 saturation curves at 200 °C. For the $GaMe_3$ saturation curve, N_2/H_2 flow rate and flow duration were kept constant at 50 + 50 sccm and 40 s, respectively. $GaMe_3$ pulse length was 0.03 s for the N_2/H_2 saturation curve. (c) GPC plotted as a function of the number of deposition cycles. Data suggests substrate-enhanced growth of GaN thin films. 101

6.7 (a) Al 2p, and (b) N 1s HR-XPS scans of 59.2 nm thick AlN thin film deposited on Si (100) substrate using optimized HCPA-ALD parameters. 103

6.8 (a) Ga 3d, and (b) N 1s HR-XPS scans of 20.1 nm thick GaN thin film deposited on Si (100) substrate using optimized HCPA-ALD parameters. 104

6.9 GIXRD pattern of 20.1 nm thick GaN thin film deposited on *c*-plane sapphire substrate using optimized HCPA-ALD parameters. 106

6.10 Surface morphologies of (a) 59.2 nm thick AlN, and (b), (c) 20.1 nm thick GaN thin films deposited on Si (100) substrates using optimized HCPA-ALD parameters. 108

6.11 GIXRD patterns of (a) AlN, and (b) GaN thin films deposited on Si (100) substrates using N_2/H_2 (50 + 50 sccm), N_2/H_2 (50 + 25 sccm) and N_2 (50 sccm) plasmas. 110

6.12 GIXRD patterns of AlN, GaN and $Al_xGa_{1-x}N$ thin films deposited on Si (100) substrates. 111

6.13 Cross-sectional (a) bright-field STEM, and (b) HR-TEM images of 25.4 nm thick $Al_{0.68}Ga_{0.32}N$ thin film deposited on Si (111) substrate using N_2/H_2 plasma. 114

6.14 (a) Spectral refractive indices, and (b) optical transmission spectra of AlN, GaN and $Al_xGa_{1-x}N$ thin films deposited Si (100) and double side polished *c*-plane sapphire substrates, respectively. . . . 115

6.15 GIXRD patterns of the thin films deposited on Si (100) and AlN/Si (100) substrates using CpIn-NH_3 and CpIn-N_2/H_2 plasma processes.117

6.16 (a)-(c) TEM and (d), (e) HR-TEM images, and (f) SAED pattern of the thin film deposited on a AlN/Si (100) substrate using CpIn-N_2/H_2 HCPA-ALD process. Deposited material was labeled as "InN" for convenience. 118

6.17 Photographs of the HCPA-ALD-AlN/Si (100) substrate (a) before and (b) after the CpIn-N_2/H_2 HCPA-ALD process. 119

6.18 GIXRD patterns of the InN thin films deposited on Si (100), Si (111) and AlN/Si (100) substrates using the CpIn-N_2/H_2 HCPA-ALD process. GIXRD patterns indicate a hexagonal wurtzite crystal structure. 120

6.19 500 nm × 500 nm 2D AFM image of InN deposited on Si (111) substrate using CpIn and N_2/H_2 plasma. Line profiles are also shown in the figure. 121

6.20 (a) 1 μm × 1 μm, and (b) 500 nm × 500 nm 2D AFM images of the InN thin film deposited on AlN/Si (100) substrate using CpIn and N_2/H_2 plasma. 121

List of Tables

2.1 Characteristic features of ALD with the consequent advantages [15]. 12

2.2 An overview of the literature reporting ALD (or ALE) of GaN. . . 17

3.1 Details regarding to the Fiji F200-LL PA-ALD system: Backing pumps, flow rates of the metalorganic precursor carrier, plasma gas carrier and door purge, turbo speed, and the resulting base pressure. 28

4.1 SE results of AlN thin films deposited at different temperatures. . 51

4.2 Elemental compositions of AlN thin films deposited at different temperatures. 52

4.3 Properties of Nylon 6,6 solutions and the resulting electrospun nanofibers. 57

4.4 SAED results, theoretical values and corresponding crystallographic planes. 62

4.5 XPS survey scan results. Eight hundred cycles AlN were deposited on a template having 330 nm average fiber diameter. 63

5.1 Details of the sequential $InMe_3$-NH_3 plasma depositions. 82

5.2 Deposition details for GaN thin film samples. 84

5.3 Elemental compositions of GaN thin film samples as determined by XPS survey scans. Data were collected after 60 s Ar ion etching. 85

5.4 Deposition details for AlN thin film samples. 87

5.5 Elemental compositions of AlN thin film samples as determined by XPS survey scans. 88

5.6 Thickness, mass density and roughness values for AlN thin film samples as estimated by XRR. Refractive index values, which were determined using SE, are also included. 89

6.1 SE results of AlN and GaN thin films deposited using non-optimized HCPA-ALD parameters. 92

6.2 SE results of AlN and GaN thin films deposited using N_2/H_2 plasma. 102

6.3 XRR results of AlN and GaN thin films deposited using optimized HCPA-ALD parameters. 107

6.4 SE results of AlN and GaN thin films deposited using N_2/H_2 and N_2 plasmas. 109

6.5 Lattice parameters, c/a ratios and alloy compositions of AlN, GaN and $Al_xGa_{1-x}N$ thin films. 113

6.6 XPS survey scan results of thin film samples deposited using CpIn-N_2/H_2 and CpIn-NH_3 HCPA-ALD processes. 116

Symbols and Abbreviations

Å	: Ångström, 10^{-8} cm or 10^{-10} m
AFM	: atomic force microscopy
ALD	: atomic layer deposition
ALE	: atomic layer epitaxy
°C	: degrees centigrade
C	: capacitance (F)
CVD	: chemical vapor deposition
DI	: deionized
ε	: relative permittivity (or dielectric constant)
ε_0	: permittivity of free space ($\simeq 8.8542\times10^{-12}$ F/m)
EDX	: energy dispersive X-ray analysis
FIB	: focused ion beam
GIXRD	: grazing-incidence X-ray diffraction
GPC	: growth per cycle
h	: hours
HCP	: hollow cathode plasma
HR	: high-resolution
I	: current (A)
ICP	: inductively coupled plasma
in.	: inches
IR	: infrared
J	: current density (A/cm^2)
k	: extinction coefficient
LPA	: line profile analysis
μm	: micrometer, 10^{-6} m
MBE	: molecular beam epitaxy
min	: minutes
MIS	: metal-insulator-semiconductor
mL	: milliliter
ML	: monolayer
MOCVD	: metalorganic chemical vapor deposition

n	: refractive index
n_{sub}	: number of subcycles
nm	: nanometer, 10^{-9} m
PA-ALD	: plasma-assisted atomic layer deposition
QCM	: quartz crystal microbalance
ρ	: mass density (g/cm^3)
rms	: root-mean-square
r	: surface roughness
s	: seconds
SAED	: selected area electron diffraction
SE	: spectroscopic ellipsometry
sccm	: standard cubic centimeter per minute
SEM	: scanning electron microscopy
t_{avg}	: average thickness
t_{etch}	: etch time
TEM	: transmission electron microscopy
UHV	: ultra high vacuum
UV	: ultraviolet
V	: voltage (V)
VIS	: visible
XPS	: X-ray photoelectron spectroscopy
XRD	: X-ray diffraction
XRR	: X-ray reflectivity

Chapter 1

Introduction

In the last few decades, considerable research has been devoted to the growth and characterization of III-nitride compound semiconductors (AlN, GaN, InN) and their alloys, which emerged as versatile and high-performance materials for a wide range of electronic and optoelectronic device applications. Wurtzite type III-nitrides exhibit direct band gaps, which extend from ultraviolet (UV) to the mid-infrared (IR) spectrum with values of 6.2, 3.4 and 0.64 eV for AlN, GaN and InN, respectively [1–8]. This feature allows the band gap of any ternary or quaternary III-nitride alloy to be easily tuned within the specified limits to adjust a particular application. Metalorganic chemical vapor deposition (MOCVD) [9, 10] and molecular beam epitaxy (MBE) [11] have already been proven to be successful techniques for achieving high-quality epitaxial III-nitride layers with low impurity concentrations and decent electrical properties. However, both of these methods employ high growth temperatures, which is neither compatible with the existing complementary metal-oxide-semiconductor (CMOS) technology nor suitable for temperature-sensitive device layers (e.g., In-rich $In_xGa_{1-x}N$) and substrates (e.g., glass, flexible polymers, etc.). This incompatibility necessitates the development of alternative low-temperature processes for the deposition of III-nitride thin films and their alloys.

In this respect, atomic layer deposition (ALD) is a low-temperature material growth method, which is based on self-terminating surface reactions [12]. Unlike chemical vapor deposition (CVD), in ALD, precursors are pulsed into the reactor one at a time, separated by purging and/or evacuation periods. Unless decomposition occurs, precursor molecules do not tend to react with themselves and hence reaction terminates when all the available reactive surface sites are occupied. This special growth mechanism is termed as *self-limiting* and results in highly uniform and conformal thin films, whose thicknesses can be controlled at the sub-angstrom scale. This makes ALD a powerful method especially for depositing films on nanostructured templates, which is considered as a successful approach for improving efficiency and/or sensitivity of devices through surface area enhancement. Moreover, alloy thin films can be easily deposited using ALD, either by controlling the relative vapor pressures of the precursors which are being pulsed into the reactor simultaneously during one of the half-cycles, or by designing a cycle that consists of subcycles of the constituent materials. The latter, which is generally named as *digital alloying*, is a unique and facile route for obtaining alloy thin films with well-defined compositions.

The motivation behind this study is, therefore, to develop ALD processes for AlN, GaN and InN thin films for

- low-temperature deposition of III-nitride thin films on sensitive device layers and substrates,
- deposition of the ternary and quaternary alloys of III-nitride family with desired composition and hence electrical/optical properties, and
- template-based synthesis of III-nitride nanostructures for improving efficiency and/or sensitivity in selected applications through surface area enhancement.

This dissertation is organized as follows. Following this brief introduction, in Chapter 2, basic background information is given. The first part of Chapter 2 is dedicated to the ALD technique. Basic principles of ALD, criteria for the selection of precursors, optimization of deposition parameters, as well as opportunities and

challenges are presented along with the terms and concepts that are necessary for the understanding of this study. In the second part of Chapter 2, an overview of research on the ALD of III-nitride thin films is given. The third and final part, on the other hand, focuses on the literature on template-based synthesis of nanostructures via ALD, with a special emphasis on AlN hollow nanofibers.

Detailed information regarding to the experimental procedure, i.e., substrate preparation, plasma-assisted ALD (PA-ALD) of III-nitride thin films and characterization methods employed, is provided in Chapter 3.

In Chapter 4, we report on the self-limiting growth of crystalline AlN thin films at low temperatures by PA-ALD using trimethylaluminum ($AlMe_3$) with ammonia (NH_3) or N_2/H_2 plasma, and present results of the optimization and characterization studies. We also demonstrate the conformality of $AlMe_3$-NH_3 PA-ALD process by presenting the characterization results of high surface area AlN hollow nanofibers fabricated using electrospun nylon nanofibers as sacrificial templates.

The problem of plasma-related oxygen contamination is addressed in Chapter 5. In this chapter, we present the results of our initial efforts to deposit GaN and InN thin films, which is followed by the exhibition of results evidencing the correlation between severity of O incorporation and choice of N-containing plasma gas (N_2, N_2/H_2 or NH_3) for AlN and GaN thin films.

In Chapter 6, we report on the effectiveness of hollow cathode plasma [13, 14] for the low-temperature deposition of crystalline AlN, GaN and $Al_xGa_{1-x}N$ thin films with low impurity concentrations. Preliminary results regarding to the hollow cathode PA-ALD (HCPA-ALD) of InN thin films are also presented within the scope of this chapter. Finally, the thesis concludes with a summary of achievements and future research directions.

Chapter 2

Background

2.1 Atomic Layer Deposition

Atomic layer deposition (ALD) is a special type of chemical vapor deposition (CVD) technique, which proceeds via sequential self-terminating gas-solid reactions. Being different from the other CVD techniques, ALD takes place in a cyclic manner, where precursors are pulsed into the reactor one at a time, separated by purging and/or evacuation periods. Each precursor exposure step saturates the substrate surface with a monomolecular layer of that precursor. This special growth mechanism is termed as *self-limiting* and results in highly uniform and conformal thin films, whose thicknesses can be simply controlled at the sub-angstrom scale.

Development of this technology has been majorly driven by the semiconductor industry, with an ultimate aim of simultaneously decreasing feature sizes, increasing aspect ratios, improving device architectures and adapting new materials. Applications of this method in device manufacturing include deposition of high-κ dielectric materials (such as Al_2O_3, HfO_2 and ZrO_2) as both alternative gate oxides in metal oxide semiconductor field effect transistors (MOSFETs) and capacitor dielectrics in dynamic random access memories.

Over the years, ALD was referred to with many different names, including: atomic layer epitaxy, atomic layer growth, molecular layer epitaxy, and molecular layering [12, 15]. The starting point of ALD is, however, controversial [12]. According to most sources, it was invented with the name of "atomic layer epitaxy (ALE)" in the late-1970s by Suntola and his co-workers in Finland [16–18]. The motivation behind its development was to grow high-quality ZnS films for thin film electroluminescent flat panel displays [19]. In the review article she authored, Puurunen [12] pointed out that the origin of ALD dates back to the work made in Soviet Union in the 1960s by the group of Professor Aleskovskii, who - in 1965 - described the $TiCl_4$-H_2O and $GeCl_4$-H_2O processes to grow TiO_2 and GeO_2 films, respectively. Puurunen further deduced that the Finnish and Russian groups were not aware of each other's research until the late-1980s.

Plasma-assisted ALD (PA-ALD), in which the surface is exposed to highly reactive radical species during one of the half-cycles, on the other hand, was first reported by de Keijser and van Opdorp in 1991 [20]. The method was then patented in 1996 by Sherman [21]. For comprehensive reviews on the histories of thermal and plasma-assisted ALD, readers may refer to Ref. [12] and [22], respectively.

2.1.1 Basic Principles

ALD is a thin film deposition technique, where two or more precursors are exposed to the substrate surface in a sequential manner, separated by purging and/or evacuation periods. Note that the separation of precursors can be temporal or spatial depending on the reactor being used. ALD is therefore a cyclic process, and one ALD cycle consists of at least four steps:

1. Exposure of the first precursor
2. Purge and/or evacuation to remove non-reacted precursor molecules and gaseous by-products
3. Exposure of the second precursor (occasionally referred as the *reactant*)

4. Purge and/or evacuation to remove non-reacted precursor (reactant) molecules and gaseous by-products

Unless decomposition occurs, precursor molecules do not tend to react with themselves, and hence the gas-solid reaction taking place at the substrate surface (steps 1 and 3) terminates when all the available reactive surface sites are occupied. This results in a unique self-limiting thin film growth mechanism, where same amount of material is deposited in each cycle, which is known as the *growth per cycle* (GPC). General characteristics of the surface chemistry of ALD, including the requirements for self-terminating reactions, adsorption kinetics, chemisorption mechanisms, factors causing saturation, growth of less than a monolayer (ML)/cycle, and growth mode were reviewed in detail by Puurunen in Ref. [12]. Readers may also refer to reviews authored by Ritala and Leskelä [15, 23], George [24] and Miikkulainen et al. [25].

The special growth mechanism of ALD ensures that GPC increases and eventually saturates at ≤1 ML/cycle with the increasing amount (dose) of precursor molecules. However it should be noted that at some point purging duration may become insufficient and dissimilar precursor molecules can meet at the gas phase, resulting in a CVD-like growth, where the self-limiting characteristic is destroyed (see Figure 2.1(a)).

The temperature range, in which an ALD process satisfies the requirements of self-terminating surface reactions, is known as the *ALD window*. Figure 2.1(b) shows the variation of GPC with temperature in its generally accepted form. It should be noted that the GPC does not need to be constant in the ALD window. GPC is known to have temperature dependency due to the effect of temperature on the number and type of reactive sites present on the surface before and after chemisorption, and due to the effect of temperature on the preferred reaction mechanism [12].

As mentioned in the previous paragraphs, ideally, same amount of material should be deposited in each cycle. However, GPC might be expected to vary with the number of ALD cycles as it depends on the number and type of reactive sites,

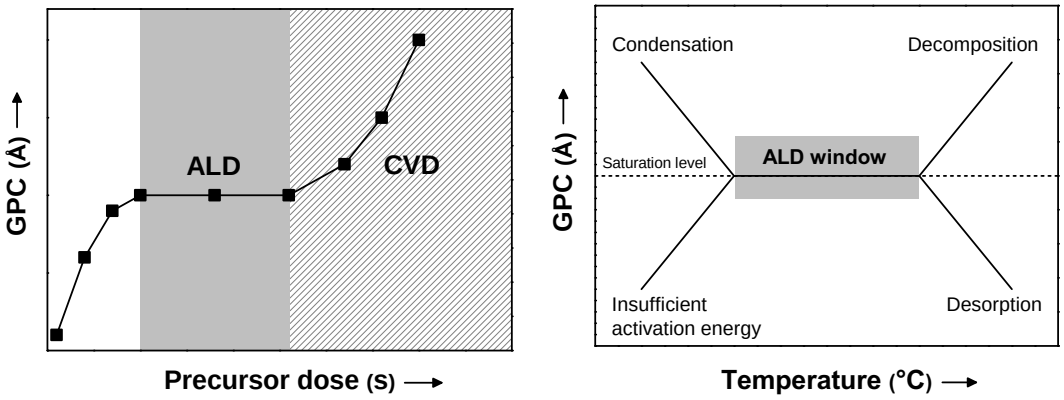

(a) (b)

Figure 2.1: (a) Variation of GPC with the increasing dose of precursor molecules. ALD and CVD regimes are indicated on the figure. (b) GPC as a function of temperature. ALD window, in which the process satisfies the requirements of self-terminating surface reactions, is depicted on the figure.

which might be different for the surfaces of original substrate and ALD-grown material. Therefore, ALD processes may exhibit different growth behaviors as shown in Figure 2.2, all of which expected to become linear after a sufficient number of ALD cycles.

More freedom in the processing conditions can be achieved by activating plasma during one of the half-cycles. Decreased process temperatures and increased GPC, as well as reduced purge steps and reduced/eliminated nucleation delay are some well-known characteristics of PA-ALD. The use of plasma radicals also increases the choice of precursors and materials by enabling lower reactivity precursors, and features processing versatility (e.g., *in situ* treatments of the substrate and deposited film). When compared to conventional thermal ALD, PA-ALD is known to be superior in terms of material properties (i.e., mass density, impurity content, etc.), stoichiometry and film composition [22, 26]. On the other hand, conformality (or step coverage) of PA-ALD is generally inferior to that of thermal ALD due to radical recombination [22, 26, 27]. Plasma-induced damage, especially in the case of direct plasma, is also commonly mentioned as a limitation of PA-ALD. A review on PA-ALD, including plasma basics, PA-ALD

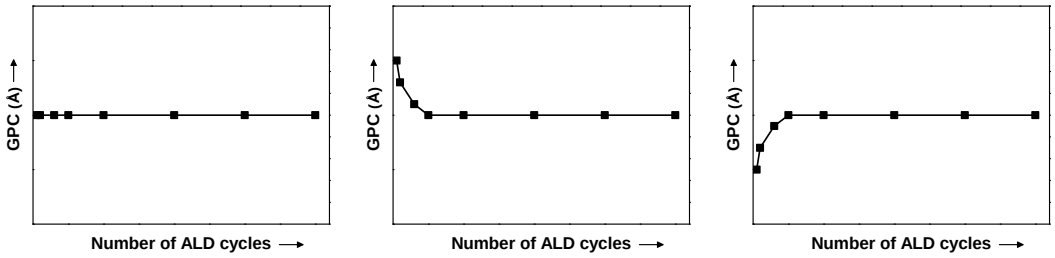

(a) (b) (c)

Figure 2.2: The dependency of GPC on the number of ALD cycles reveals different types of growth behavior: (a) linear, (b) substrate-enhanced, and (c) substrate-inhibited.

configurations, merits and challenges of PA-ALD with some selected applications has recently been published by Profijt et al. [22].

2.1.2 Selection of Precursors

A variety of inorganic and metalorganic precursors, which are generally classified according to their ligand groups, have been reported to be used in ALD processes [12, 15]. Volatility, stability, reactivity, and availability of the precursor, and inertness of its by-products, are commonly referred as the five requirements that a precursor must fulfill.

- *Volatility* - The selected precursor must be volatile either at room temperature or at higher temperatures. Although the required vapor pressure of precursor is reactor specific, 0.1 and 1 Torr are generally referred as the minimum and desired values, respectively. Vapor pressure curves of metalorganic precursors used in this study, as calculated from the equations given in Ref. [28–31], are given in Figure 2.3. Trimethylaluminum ($AlMe_3$), triethylgallium ($GaEt_3$) and trimethylindium ($InMe_3$) were used at room temperature as their vapor pressures range between 2.6-11.6 Torr at this temperature. As seen from Figure 2.3, trimethylgallium ($GaMe_3$) has a very high vapor pressure at room temperature (i.e. ~228 Torr). This precursor

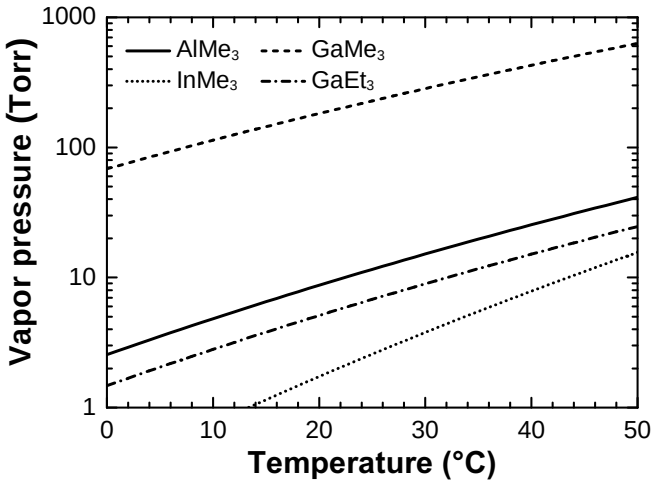

Figure 2.3: Vapor pressures of the metalorganic precursors used in this study as a function of temperature.

was therefore cooled down to ~6 °C in an effort to decrease its equilibrium vapor pressure. The vapor pressure of cyclopentadienyl indium (CpIn) was reported as 0.1 Torr at 40 °C [32]. We were able to see clear pulses of CpIn only at precursor temperatures ≥85 °C.

- *Stability* - The precursor molecules must be stable and not decompose thermally at the ALD processing temperature as their reaction with the substrate surface or growing film must be self-terminating. Self-decomposition of the precursor molecules would destroy the self-limiting thin film growth mechanism, and result in a CVD-like growth.

- *Reactivity* - Since precursor molecules do not meet at the gas phase, most aggressively reacting precursor combinations must be preferred in ALD. This would ensure short cycle times and effective precursor utilization via rapid completion of the gas-surface reactions.

- *Availability* - The selected precursor must be easy to synthesize and/or found in relatively abundant quantities.

- *Unreactive volatile by-products* - The selected precursors should preferably produce unreactive volatile by-products, which can be easily purged out

from the reactor. Reactive by-products may corrode the reactor parts and thereby decrease the lifetime of deposition system. Moreover, they may etch the growing film and/or compete with the following precursor for available reactive surface sites.

It should be emphasized that the process conditions (i.e., temperature, pulse and purge durations), residual contaminates (Cl, C, H, etc.) remaining in the ALD-grown film, as well as electrical and optical properties, and physical morphology of the film are governed by the choice of precursors. As semiconducting materials are more sensitive to impurities than any other material, the purities of the selected precursors and carrier gas are also important.

2.1.3 Optimization of Deposition Parameters

As the first step of optimization studies, saturation curves are obtained for both precursors. Saturation values should be determined depending on the uniformity of targeted substrate area. In this study, we performed experiments by gradually increasing the pulse length of a precursor, while keeping all other variables constant. We obtained GPC values by dividing the thickness values obtained from spectroscopic ellipsometry or X-ray reflectivity measurements by the number of ALD cycles. In a typical ALD process, GPC is expected to first increase and then reach saturation with increasing pulse length since it proceeds via self-terminating gas-solid reactions. It should be noted that the saturation behavior will not be observed if precursor molecules decompose at the deposition temperature and/or different types of precursor molecules meet at the gas phase as a result of insufficient purging.

As the following step, ALD temperature window (i.e., the temperature range at which film growth takes place in a self-limiting manner) is determined. For this purpose, thin films are deposited at different temperatures using saturation values of precursor pulse lengths and predetermined purge durations. It should be noted that the purging efficiency increases with temperature. Therefore predetermined purge durations may not apply at lower temperatures. Plotting the GPC values

as a function of deposition temperature is expected to reveal the ALD window. However, as also mentioned in Section 2.1.1, GPC may have temperature dependency. In such cases, the best approach would be to obtain saturation curves at different temperatures.

Finally, the growth behavior is determined by the deposition of different number of ALD cycles using optimized parameters, and then plotting the GPC (or film thickness) data as a function of number of cycles. Different types of growth behavior are shown in Figure 2.2.

Optimization of deposition parameters using *ex situ* characterization tools requires a significant number of thin film samples to be prepared. Although deposition experiments are generally done using minimum doses of precursors and minimum number of ALD cycles, still considerable amounts of time and source materials are needed. In this respect, ALD processes have been effectively studied using *in situ* characterization tools, such as spectroscopic ellipsometry [33–35], quartz crystal microbalance [32, 34, 36], mass spectroscopy [32, 34, 37], Fourier transform infrared spectroscopy [33, 36, 38], and optical emission spectroscopy [34], not only for the optimization of deposition parameters, but also for the investigation of early stages of ALD processes (i.e., nucleation and growth) and determination of reaction mechanisms.

2.1.4 Opportunities and Challenges

The self-limiting growth mechanism of ALD results in unique advantages including accurate and simple film thickness control, excellent conformality and uniformity over large areas, composition control, and repeatability. Characteristic features of ALD and the consequent advantages as summarized by Ritala and Leskelä in Ref. [15] are given in Table 2.1.

Table 2.1: Characteristic features of ALD with the consequent advantages [15].

Characteristic feature of ALD	Inherent implication on film deposition	Practical advantage
Self-limiting growth process	Film thickness is dependent only on the number of deposition cycles	Accurate and simple thickness control
	No need of reactant flux homogeneity	Large-area capability Large-batch capability Excellent conformality No problems with inconstant vaporization rates of solid precursors Good reproducibility Straightforward scale-up
	Atomic level control of material composition	Capability to produce sharp interfaces and superlattices Possibility to interface modification
Separate dosing of reactants	No gas phase reactions	Favors precursors highly reactive toward each other, thus enabling effective material utilization
	Sufficient time is provided to complete each reaction step	High quality materials are obtained at low processing temperatures
Processing temperature windows are often wide	Processing conditions of different materials are readily matched	Capability to prepare multilayer structures in a continuous process

Atomic level control of material composition enables the deposition of sharp interfaces, quantum wells [39], superlattices and nanolaminates [40–42], as well as graded [43], alloy [44] and doped [45, 46] thin films. Digital control of thickness, as well as conformal and non-line-of-site deposition, on the other hand, makes ALD a powerful method for coating particles [47] and synthesizing complex nanostructures using templates such as anodic aluminum oxide membranes [48], carbon nanotubes [49], etc. The low-temperatures used in ALD further allow deposition on temperature-sensitive organic substrates (flexible polymers [50], electrospun nanofibers [51, 52], self-assembled peptide nanofibers [53], etc.), even on biological templates such as butterfly wings [54] and tobacco mosaic viruses [55]. By taking advantage of the non-uniform deposition at the early stages of ALD, quantum dots and nanoparticles can also be deposited on various substrates [52, 56, 57]. For additional examples of novel applications, readers may refer to review articles authored by Knez et al. [58] and Kim et al. [59]. These articles also mention area-selective ALD, which is accomplished by the selective passivation of reactive surface sites by immobilizing molecules [60].

The slowness of the film growth is often considered as a major disadvantage of this process. However, in most cases, the low thickness requirement for films (typically <200 Å), together with the large-batch processing capability of ALD [61, 62] compensate this drawback and make ALD deposition rates sufficient to meet manufacturing requirements. It has been also shown that the cycle times can be reduced significantly by the use of novel reactor designs enabling roll-to-roll ALD via spatial separation of the precursors [62–64].

2.2 ALD of III-Nitride Thin Films

2.2.1 Aluminum Nitride Thin Films

Thermal ALD (or ALE) of aluminum nitride (AlN) has been extensively studied using ammonia (NH_3) and various Al precursors: aluminum trichloride ($AlCl_3$) [65, 66], dimethylethylamine alane ($Me_2EtN{:}AlH_3$) [67–70], triethylaluminum ($AlEt_3$) [71, 72], trimethylaluminum ($AlMe_3$) [66, 73–89], trimethylamine alane ($Me_3N{:}AlH_3$) (with deuterated ammonia (ND_3)) [90], and tris(dimethylamido)aluminum ($Al_2(NMe_2)_6$) [91–93]. Ti(Al)N thin films were also deposited using $AlMe_3$ and ND_3 precursors [37]. AlN thin films deposited using thermal ALD (or ALE) found applications as buffer layers for the growth of high-quality materials [77, 85], blocking layers against dopant diffusion [94, 95], insulating/passivating interfacial layers for MOSFETs [91, 92] and $In_{0.53}Ga_{0.47}As/ZrO_2$ interfaces [96], as well as surface passivation layers for surface channel field effect transistors [88], 4H-SiC devices [97, 98], tungsten nitride films [99], and photoactive magnetic nanoparticles [89]. ALD-grown AlN films were also used for the fabrication of annular photonic crystals [86].

Although there were publications on the PA-ALD of $Ti_xAl_{1-x}N$ [100–102] and AlON [103–105] films, PA-ALD of AlN was first reported in 2004 by Lee et al. [106], where AlN thin films were deposited at 350 °C using $AlCl_3$ and NH_3/H_2 plasma. Growth rate of this process saturated at ~0.42 Å/cycle, resulting with films composed of microcrystallites of wurtzite (100) in an amorphous AlN matrix [107]. Although $AlCl_3$ is a highly reactive and thermally stable precursor, which yielded good results in terms of achieving true ALD conditions, the use of halogenated precursors is in general not preferred due to several reasons. Most importantly, their reaction with hydrogen-containing nonmetals results in gaseous corrosive by-products (HCl in the case of chloride precursors), which can etch the deposited film, as well as the reactor components. Furthermore, halide ligands incorporate into the growing film and remain as impurities. They also create a memory effect in the chamber; i.e. residual halides in the system contaminate the subsequently deposited films for a long period of time following the use of a

halogenated precursor.

Among all the metalorganic Al precursors listed above, $AlMe_3$ is probably the most recognized one due to the well-known $AlMe_3$-H_2O thermal ALD process that is designed for depositing dielectric Al_2O_3 layers [12]. Unfortunately, thermal ALD of AlN using $AlMe_3$ and NH_3 is not possible since these two precursors only react at temperatures where $AlMe_3$ self-decomposition occurs [76]. Therefore, true ALD conditions for the deposition of AlN using $AlMe_3$ and NH_3 can only be achieved if the deposition temperature is lowered by enhancing the reactivity of NH_3 using an external energy source, such as plasma. PA-ALD of nitride thin films is not limited with the use of NH_3; alternatively, a mixture of N_2 and H_2 gases can also be employed to create similar plasma radicals.

It is worth mentioning that at the time we started this research there were only few publications reporting on the plasma- and UV-assisted ALD of AlN. Liu et al. [83] studied PA-ALD of AlN within the temperature range of 250-470 °C, using $AlMe_3$ and NH_3 plasma as the Al and N precursors, respectively; however they did not observe a clear self-limiting growth behavior. Eom et al. [108], on the other hand, demonstrated the UV-assisted ALD of AlN at 240-370 °C using the same precursor combination. Remote plasma ALD of amorphous AlN thin films using $AlMe_3$ and N_2/H_2 plasma was reported by Kim et al. [109]. In their study, growth rate saturated at ~1.25 Å/cycle within the range of 100-400 °C and then decreased with increasing temperature.

The number of publications focusing on the PA-ALD (or plasma-assisted ALE, PA-ALE) of AlN using $AlMe_3$ has increased considerably in the last few years [27, 110–115]. AlN films deposited using NH_3 [27, 111], NH_3/N_2 [112, 113], N_2/H_2 [113, 114], and N_2 [113] plasmas were reported to be either amorphous or polycrystalline. In a recent study, Nepal et al. [115] demonstrated the PA-ALE of AlN films at 200-650 °C using $AlMe_3$ and N_2 plasma, and emphasized the significance of *ex situ* and *in situ* surface pretreatments for promoting two-dimensional nucleation, and hence the epitaxial growth of AlN thin films. In their study, growth parameters were optimized for the highest quality material, which was achieved at 500 °C with a CVD component in the film growth

mechanism. PA-ALD and -ALE grown AlN thin films were used in resistive memories [116], transistors [117–124] and in other devices/structures for work function tuning [125, 126] and passivation [127–131]. AlN mask layers grown by low-temperature PA-ALD were also demonstrated [132]. Very recently, Choi et al. [133] reported on the applicability of Ru-AlN thin films prepared by PA-ALD as a novel multifunctional heating resistor film for non-passivated type thermal inkjet printer devices.

2.2.2 Gallium Nitride Thin Films

When compared to AlN, significantly less number of publications concentrated on the ALD of gallium nitride (GaN) thin films. Thermal and plasma-assisted ALE, as well as thermal ALD of GaN have been studied at temperatures >450 °C using triethylgallium ($GaEt_3$) [134, 135], trimethylgallium ($GaMe_3$) [136–141] and gallium trichloride ($GaCl_3$) [142, 143] precursors. Lower ALE growth temperatures (350-400 °C) were achieved when gallium chloride (GaCl) was used as the Ga precursor [144, 145]. Sumakeris et al. [146] used a novel reactor design that employs hot filaments to decompose the NH_3 and deposited epitaxial GaN films using $GaEt_3$ within the temperature range of 250-350 °C. Recently, Sharp et al. [147] presented their results on the PA-ALD of GaN thin films at 150-350 °C using $GaEt_3$ and N_2/H_2 plasma as the Ga and N precursors, respectively. In their study, the concentrations of O and C impurities in GaN films were reported as ≥3 at.%.

Table 2.2 summarizes the details of experimental investigations focusing on the ALD (or ALE) of GaN thin films. Note that some of these processes do not fully obey the requirements of ALD (e.g, gas phase reactions, decomposition of the precursors, etc.) although they were named as ALD (or ALE) by the authors. The most apparent ones are Ref. [141] and [148], where one of the precursors was continuously supplied during the entire process. It is worth mentioning that there is a significant number publications in literature reporting such processes, which have been not included in Table 2.2 intentionally.

Table 2.2: An overview of the literature reporting ALD (or ALE) of GaN.

Ga precursor	Reactant	Method	Growth conditions	Substrate/ buffer layer	Material and crystal structure	Growth rate	Ref.
$GaEt_3$	NH_3	SALE[1] using a LPMOCVD[3] system	450-900 °C 76-150 Torr	Al_2O_3 (0001)/ AlN	single crystal *h*-GaN	1 ML^2/pulse at 900 °C and 76 Torr	[134, 135]
		SALE[1]	76 Torr	Al_2O_3 (0001)/ GaN (or AlN)	single crystal GaN/ AlN short-period superlattices	1 ML^2 GaN/ cycle	[72]
	NH_3, thermally cracked	ALE using a rotating reactor	150-650 °C 0.5-50 Torr	α(6H)-SiC (0001)	amorphous GaN for T < 120 °C, single single crystal *h*-GaN for T = 250-350 °C	0.67 ML^2/cycle at 120 °C 0.87 ML^2/cycle at 380 °C	[146]
	N_2/H_2 plasma	PA-ALD	150-350 °C 5 mTorr H-rich plasma	Si	*h*-GaN[8]	0.44 Å/cycle	[147]
$GaMe_3$	N_2/H_2 plasma	PA-ALE[4] using a rotating disk ALE unit	580-750 °C 5 Torr	Al_2O_3 (0001)/ GaN[5]	highly *c*-oriented polycrystalline or single crystal *h*-GaN	1250 Å/h	[136]
	NH_3	ALE using a rotating susceptor	550-650 °C 700 Torr	Al_2O_3 (0001)/ AlN	single crystal GaN		[137]

$GaMe_3$	NH_3	ALE using a rotating susceptor	600-700 °C 100 Torr	Al_2O_3	single crystal $In_xGa_{1-x}N$[6]	0.2-1 Å/cycle	[149]
				Al_2O_3/AlN	single crystal GaN and $In_xGa_{1-x}N$[6]	0.1-2 Å/cycle	[138]
				Al_2O_3 (0001)/ AlN	single crystal GaInN		[77]
			650 °C		InGaN		[150]
		ALE	650-700 °C 760 Torr	Al_2O_3 (0001)/ AlN/AlGaN graded to GaN	single crystal *h*-InGaN		[151]
		ALE using an atmospheric pressure quartz reactor	500-650 °C 760 Torr	2° off GaAs (001)/ GaN	*h*-GaN with a cellular structure	1.1-2.4 Å/cycle at 550 °C	[139]
			500-950 °C 760 Torr	Al_2O_3 (0001)/ GaN	single crystal *h*-GaN		[140]
	NH_3, continuously supplied	ALD using a LPMOCVD[3] system	850 °C	*c*-plane Al_2O_3	AlGaN barrier of the AlGaN/GaN multiple quantum well structure	0.14 μm/h	[148]

$GaMe_3$, continuously supplied	NH_3	PALE[7] using a MOCVD reactor	1100 °C 50 Torr	*r*-plane Al_2O_3/ GaN	*a*-plane GaN	3.0 μm/h (max)	[141]
$GaCl_3$	NH_3	ALE	500 °C 760 Torr	GaAs (001), GaAs (111)/ GaAs	amorphous GaN, single crystal *h*-GaN		[142]
		ALD	500-750 °C 1 Torr	Si (100)	(0002) and (10-11) oriented *h*-GaN	2.1±0.5 Å/cycle; i.e., 29-47% of 1 ML²/cycle at 500-750 °C	[143]
GaCl	NH_3	ALE using a halogen-transport system	350-400 °C 760 Torr	GaAs (001)/ GaN	*c*-GaN with [001] direction perpendicular to the substrate	1 ML²/cycle at 350-400 °C 0.45 ML²/cycle at 410-550 °C	[144]
			400 °C 760 Torr	GaAs (001)/ GaN	amorphous GaN, *c*-GaN with [001] direction perpendicular to the substrate	1 ML²/cycle at 400 °C	[145]
Ga	N_2	ALE using a commercial MBE machine	730 °C	MOCVD-GaN on Al_2O_3/GaN/ AlN or AlGaN	*h*- and *c*-GaN films, quantum wells and quantum dots	2 ML²/cycle	[152]

Ga	N_2	ALE using a commercial MBE machine	740, 750 °C	MOCVD-GaN on Al_2O_3/AlN, quantum dot samples were grown on bulk 6H-SiC	GaN film, quantum well heterostructures, quantum dots	1.4±0.3 ML[2]/ cycle	[153]

[1]SALE is the abbreviation of *switched atomic layer expitaxy.*
[2]1 ML GaN is approximately 2.6 Å.
[3]LPMOCVD is the abbreviation of *low-pressure metalorganic chemical vapor deposition.*
[4]PA-ALE is the abbreviation of *plasma-assisted atomic layer epitaxy.*
[5]For polycrystalline samples.
[6]$0 \leq x \leq 0.27$.
[7]PALE is the abbreviation of *pulsed atomic layer epitaxy.*
[8]Sharp et al. [147] reported that the XRD analysis has shown a small peak attributable to GaN (002).

2.2.3 Indium Nitride Thin Films

The literature on the ALE of indium nitride (InN) is very limited. The first study was published in 1991 by Higuchi et al. [154], who reported the ALE of polycrystalline hexagonal wurtzite InN (*h*-InN) thin films using indium trichloride ($InCl_3$) and NH_3. In their study, InN films were deposited on quartz and *c*-plane sapphire substrates at temperatures ranging from 420 to 520 °C. The highest growth rate, which was observed at 460-480 °C, was >1 monolayer (ML)/cycle, suggesting the absence of a self-limiting characteristics. It is also worth mentioning that the grown surfaces had an island structure as reported by the authors. The optical and electrical properties, as well as phonon structure of the epitaxial *h*-InN thin films, which were deposited via UV-assisted ALE using $InCl_3$ and NH_3 precursors, were reported by Inushima et al. [155, 156]. For the film deposited at 440 °C, growth rate was determined as 2.8 Å/cycle, which corresponds to ~1 ML/cycle for *c*-axis oriented *h*-InN.

InN and $In_xGa_{1-x}N$ thin films were also deposited using ethyldimethylindium ($InEtMe_2$) and NH_3 [77, 138, 149–151, 157]. Boutros et al. [138, 149] demonstrated the ALE of single crystal $In_xGa_{1-x}N$ ($0 \leq x \leq 0.27$) thin films at 600-700 °C, where growth conditions were optimized to obtain high-quality films rather than to achieve a self-limiting characteristic. In their study, incorporation efficiency of In in the growing $In_xGa_{1-x}N$ film increased with decreasing growth temperature. McIntosh et al. [77] reported that the incorporation of In into the ternary alloy involves a complicated set of reaction pathways, which depend on the precursor In/Ga ratio, the absolute partial pressures of the In and Ga precursors above the growing film, and on the growth temperature. In their following articles, authors presented a model for the In incorporation during the growth of $In_xGa_{1-x}N$ films [150, 157]. They also studied the effect of hydrogen on the In incorporation [151]. ALE of epitaxial InN films was realized at 480 °C on AlN buffer layers grown by ALE on sapphire substrates [77, 157]. Lower growth temperatures resulted in polycrystalline films, while at higher temperatures the formation of InN was practically inhibited due to the reduced thermal stability. Authors also reported the formation of In metal on the surface of growing film

with the use of high $InEtMe_2$ fluxes.

In a recent study, InN thin films having either a novel cubic and/or a hexagonal phase were grown by PA-ALE [158]. In their study, Nepal et al. used trimethylindium ($InMe_3$) and N_2 plasma as the In and N precursors, respectively. They observed two distinct ALE windows for the samples deposited on both *ex situ* and *in situ* treated substrates; i.e., 175-185 °C and 220-260 °C. InN film deposited at 183 °C on *a*-plane sapphire substrate was epitaxial with a novel NaCl-type crystal structure. In the higher temperature window, on the other hand, InN grown on *a*-plane sapphire was dominated by the hexagonal structure, with a small component of the NaCl-type cubic phase.

2.3 Template-Based Synthesis of Nanostructures via ALD: AlN Hollow Nanofibers

AlN, which is the widest band gap compound of III-nitride family, exhibits attractive material properties such as wide and direct band gap of 6.2 eV (hexagonal AlN), small (even negative) electron affinity, significant piezoelectric response, good dielectric properties, chemical stability, high thermal conductivity, and low thermal expansion. Owing to this unique set of properties, nanostructures of AlN (e.g., nanotubes [159–164], hollow nanofibers [165], etc.) have recently attracted considerable attention as promising candidates for high surface area, high sensitivity chemical and biological sensor applications [166, 167]. Template-free or template-based approaches may be adopted for the syntheses of nanostructures. In most cases, template-free methods were reported for tubular AlN nanostructures. Polycrystalline cubic AlN (*c*-AlN) nanotubes were synthesized by gas-phase condensation using the solid-vapor equilibrium and their field emission properties were investigated [159]. Faceted hexagonal AlN (*h*-AlN) nanotubes were obtained by nitriding the aluminum powder in a horizontal tubular furnace [160]. *c*-AlN nanotubes were produced by reacting $AlCl_3$ and NH_3 gases at 1200 °C [161]. Nanotubes of AlN were obtained as the side product while synthesizing a bulk layer of AlN polycrystals [162]. Amorphous AlN nanotubes

filled with nickel nanoparticles were also realized through the reaction of NH_3 over Ni-Al thin film at 1000 °C [163]. Recently, synthesis of *h*-AlN nanotubes by a roll-up approach at 350 °C was reported, using AlP and NaN_3 as the Al and N sources, respectively [164]. Polycrystalline *h*-AlN hollow nanofibers were produced by carbothermal reduction and nitridation of precursor fibers obtained by electrospinning [165].

Methods reported in the above-mentioned studies generally require high temperatures (>1000 °C) and in some cases there exist additional morphologies such as nanoparticles or nanowires in the final product. The most obvious constraint of template-free synthesis is probably the limited control over the properties of resulting structure (e.g., crystal structure, dimensions, etc.). Template-based synthesis, on the other hand, is a straightforward way of producing nanostructures with controlled properties, which in general requires a suitable deposition method and a sacrificial substrate having the desired geometry. Selected template material should not only be resistant to the growth ambient (temperature, pressure, gases), but should be able to disappear with a simple post-deposition treatment as well, unless it has a function in the final structure. Yin et al. [168] reported on the synthesis of coaxial C-AlN-C composite nanotubes at 1600 °C using a chemical substitution reaction in a controllable two-stage process using multiwalled carbon nanotubes as templates. Another example was demonstrated by Stan et al. [169], in which epitaxial *h*-AlN shells were grown by metalorganic CVD (MOCVD) at 1000 °C around GaN nanowire templates. Templates were then removed by annealing at 1120 °C under H_2 atmosphere, leaving behind empty AlN shells. Temperatures used for the synthesis of AlN nanostructures can be lowered considerably by alternating the deposition method. Besides being a low-temperature process, ALD also offers precise thickness control as well as excellent uniformity and conformality with its self-limiting growth mechanism. These unique characteristics make ALD a powerful technique for synthesizing nanostructures through template-based methods.

Variety of templates can be used as the deposition temperature decreases. For instance, polymers are promising materials as sacrificial templates due to their availability, design flexibility and very low cost. Polymeric fibers having

diameters in the range of few micrometers to few hundred nanometers can be obtained via electrospinning, a basic process in which a polymer solution or melt pumped from syringe is subjected to high voltages. The shapes and dimensions of the electrospun nanofibers can be easily tuned by varying the polymer type, polymer concentration, solvent type, or controlling the electrospinning parameters including applied voltage, tip-to-collector distance, flow rate, etc. [170]. Very recently, electrospinning and ALD processes have been combined for synthesizing tubular nanostructures. Peng et al. [171] used electrospun polymeric fiber template for fabricating long and uniform metal oxide microtubes with precise wall thickness control. In their study, Al_2O_3 was deposited by ALD on electrospun polymeric microfibers; polymeric core was then selectively removed by calcination. This approach was also applied for the fabrication of hollow nanofibers (or nanotubes) of various sizes from various materials such as HfO_2 [172], SnO_2 [173, 174], TiO_2 [175, 176], and ZnO [177, 178] using different electrospun polymeric nanofiber templates. Moreover, $NiFe_2O_4$-TiO_2 [179], TiO_2-ZnO [180], SnO_2-ZnO [181], and nylon-ZnO [51, 52] core-shell nanofibers, as well as microtube-in-microtube $ZnAl_2O_4$ assemblies [182] were also fabricated successfully by combining electrospinning and ALD processes. To the best of our knowledge, synthesis of AlN hollow nanostructures by combining electrospinning and ALD has not yet been reported.

Chapter 3

Experimental Details

3.1 Preparation of Substrates

3.1.1 Planar Substrates

Si (100), Si (111), *c*-plane sapphire, MOCVD-grown GaN on *c*-plane sapphire, and glass (Pyrex) substrates were cleaned by sequential ultrasonic agitation in 2-propanol, acetone, methanol, and deionized (DI) water. For the native oxide removal, Si substrates were further dipped into dilute hydrofluoric acid solution (HF, 2 vol.%) for 1-2 min, then rinsed with DI water and dried with N_2. Substrates were then immediately loaded to the reactor using a load lock and kept at the deposition temperature for at least 20 min before the run was initiated.

3.1.2 Nanofiber Templates Prepared by Electrospinning

Electrospun Nylon 6,6 nanofiber templates having different average fiber diameters were produced using different solvent systems (1,1,1,3,3,3-hexafluoro-2-propanol (HFIP; ≥99%, Sigma-Aldrich) and formic acid (98-100%, Sigma-Aldrich)) and polymer concentrations. 8 wt.% Nylon 6,6 (relative viscosity

230.000-280.000) pellets were dissolved in formic acid; 5 wt.% and 8 wt.% Nylon 6,6 were dissolved in HFIP separately for 3 h. Prepared homogeneous clear solutions were loaded individually in a 3 mL syringe fitted with a metallic needle having 0.8 mm inner diameter. Syringe was fixed horizontally on the syringe pump (Model: KDS 101, KD Scientific) and polymer solutions were pumped with a feed rate of 1 mL/h during electrospinning. Electrospinning of the solutions was performed by applying a voltage of 15 kV to the metal needle tip by high voltage power supply (AU Series, Matsusada Precision). Tip-to-collector distance was set at 10 cm. On the way to the grounded stationary cylindrical metal collector (height: 15 cm, diameter: 9 cm) covered by a piece of aluminum foil, the solvents evaporated; and solid electrospun Nylon 6,6 nanofibers were deposited on the collector. The electrospinning setup was enclosed in a Plexiglas box, which allowed electrospinning process to be carried out at 24 °C and 30% relative humidity. Morphologies and fiber diameters of the electrospun nanofibers were analyzed by scanning electron microscopy (SEM; FEI Quanta 200 FEG SEM). Average fiber diameters of the samples were calculated by measuring diameters of ~100 different fibers from high magnification SEM images.

3.2 Plasma-Assisted Atomic Layer Deposition of III-Nitride Thin Films

3.2.1 Precursors and Plasma Gases

Metalorganic precursors, namely trimethylaluminum ($Al(CH_3)_3$ or $AlMe_3$), trimethylgallium ($Ga(CH_3)_3$ or $GaMe_3$), triethylgallium ($Ga(C_2H_5)_3$ or $GaEt_3$), trimethylindium ($In(CH_3)_3$ or $InMe_3$) (Sigma Aldrich, SAFC Hitech) and cyclopentadienyl indium (C_5H_5In or CpIn) (Strem Chemicals) were used as the group-III source materials. $AlMe_3$, $GaEt_3$ and $InMe_3$ were used at room temperature. $GaMe_3$ was cooled down to 6 °C using a home-made Peltier cooling system, whereas CpIn was heated to 85 °C.

5N-grade plasma gases, ammonia (NH_3), N_2 and H_2, and the carrier gas, Ar, were used without any further purification during the depositions described in Chapter 4, as well as Sections 5.1 and 5.2. NH_3, N_2, H_2, and Ar were further purified using MicroTorr gas purifiers during the depositions described in Section 5.3 and Chapter 6.

3.2.2 The Reactor

Plasma-assisted atomic layer deposition (PA-ALD) of III-nitride thin films was carried out at temperatures ranging from 100 to 500 °C in Fiji F200-LL ALD reactor equipped with an inductively coupled RF-plasma (ICP) source (Ultratech/Cambridge Nanotech). The configuration and main components of the PA-ALD system are depicted in Figure 3.1. Unless stated otherwise, the door and turbo Ar purges were on, former being set to 50 sccm. Metalorganic precursor pulses and plasma gases were carried from separate lines using Ar. Remote plasma (300 W) was activated at each PA-ALD cycle only during the flow of N-containing plasma gas.

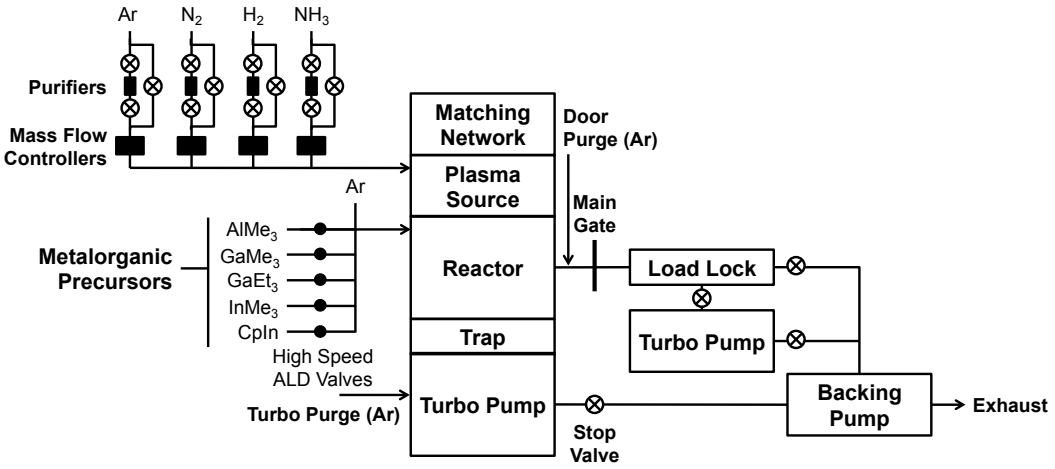

Figure 3.1: Schematics of the Fiji F200-LL PA-ALD system.

Due to the technical difficulties encountered, the original backing pump of the PA-ALD system (Adixen ACP 120G) was replaced with pumps having different pumping speeds. In order to obtain similar base pressures, flow rates of the metalorganic precursor carrier, plasma gas carrier and door purge, and speed of the Adixen ATH 400M turbo pump were adjusted. Table 3.1 summarizes these details for samples deposited within the context of this work.

Table 3.1: Details regarding to the Fiji F200-LL PA-ALD system: Backing pumps, flow rates of the metalorganic precursor carrier, plasma gas carrier and door purge, turbo speed, and the resulting base pressure.

Chapter/Section	4, 5.1, 5.2	5.3.1[a]	5.3	6
Backing pump	Adixen ACP 120G	Anest Iwata ISP-250C	Anest Iwata ISP-250C	Edwards nXDS20iC
Flow rates (sccm)				
Metalorganic carrier	60	45	30	30
Plasma carrier	200	150	100	100
Door purge	50	30	0	50
Turbo speed (rpm)	21500	31500	25000	25000
Base pressure (mTorr)	200-250	200-250	~150	~150

[a]Only for the $GaMe_3$-NH_3 plasma process described in Section 5.3.1.

During the GaN and AlN depositions described in Section 5.3, load lock of the PA-ALD system was temporarily disabled. Therefore, samples were loaded to the reactor through the main gate while the reactor was at atmospheric pressure. The gate was then closed using a custom-made aluminum lid and the reactor was evacuated. Reactor was baked out at 250 °C for ~12-18 h prior to each deposition. After these bake outs, the lowest vacuum level was measured as 8.2×10^{-6} Torr at 190 °C.

The depositions described in Chapter 6 were carried out in a modified Fiji F200-LL ALD reactor. In this modified configuration, the original quartz-based ICP source of the ALD system was replaced with a stainless steel hollow cathode plasma (HCP) source (Meaglow Ltd.) [13, 14]. The original RF power supply

(Seren IPS, R301), automatic matching network (Seren IPS, AT-3) and matching network controller (Seren IPS, MC2) units were used to activate the HCP discharge. Representative photographs of the quartz-based ICP and stainless steel HCP sources are given in Figures 3.2(a) and 3.2(b), respectively.

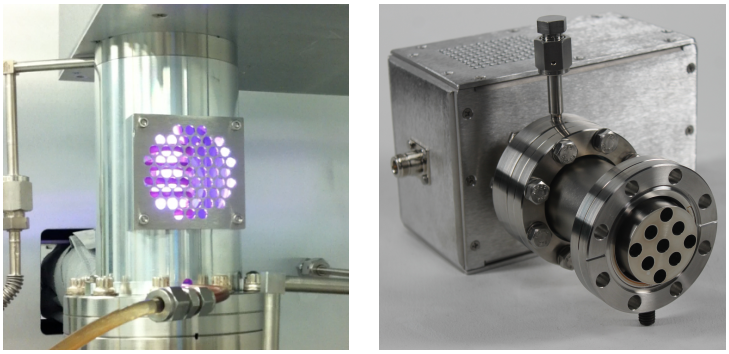

(a) (b)

Figure 3.2: Representative photographs of (a) quartz-based ICP, and (b) stainless steel HCP sources.

3.2.3 Synthesis of AlN Hollow Nanofibers

AlN depositions were carried out at 200 °C with a base pressure of 200-250 mTorr. Four hundred and 800 cycles of AlN were deposited on electrospun Nylon 6,6 nanofibers via PA-ALD using $AlMe_3$ and NH_3. One PA-ALD cycle consisted of 0.1 s $AlMe_3$/10 s Ar purge/40 s, 50 sccm, 300 W NH_3 plasma/10 s Ar purge. Ar was used as the carrier and purge gas. Precursor and plasma carrier gas flow rates were 60 and 200 sccm, respectively. *In situ* calcination of the AlN-coated nanofibers was carried out at 500 °C for 2 h under 260 sccm Ar flow. Samples were taken out from the reactor through a load lock and exposed to air as soon as the ALD reactor cooled down to 200 °C. AlN hollow nanofibers were also prepared by *ex situ* calcination at air ambient (500 °C, 2 h).

3.3 Characterization Methods

3.3.1 Characterization of Thin Films

3.3.1.1 X-Ray Photoelectron Spectroscopy

Chemical compositions and bonding states were determined by X-ray photoelectron spectroscopy (XPS) using Thermo Scientific K-Alpha spectrometer with a monochromatized Al K_α X-ray source. Pass energy, step size and spot size were 30 eV, 0.1 eV and 400 μm, respectively. Etching of the samples was carried out *in situ* with a beam of Ar ions having an acceleration voltage of 1 kV. Unless stated otherwise, high-resolution XPS data were corrected for charging by shifting peaks with respect to the adventitious C peak located at 284.8 eV. Peak deconvolution was performed using the Avantage Software, without applying any restrictions to spectral location and full width at half maximum (FWHM) values.

3.3.1.2 Secondary Ion Mass Spectroscopy

Secondary ion mass spectroscopy (SIMS) measurements were realized by the Evans Analytical Group (EAG) using a Physical Electronics Quadrupole SIMS instrument. Analyses were carried out using EAGs proprietary analytical protocols. Calibrations were based on relevant AlN, GaN and AlGaN internal standards for concentration and depth. Atomic mixing or depth resolution of the primary ion beam setup was <9 nm/decade. Therefore, any decay length ≥9 nm/decade in the acquired profiles should be free of SIMS broadening artifacts and represent true slope of concentration distribution. However, heterogeneous sample structure may cause further broadening where element penetration may appear deeper than it actually is.

3.3.1.3 Grazing-Incidence X-ray Diffraction and Line Profile Analysis

Grazing-incidence X-ray diffraction (GIXRD) measurements were carried out by PANalytical X'Pert PRO materials research diffractometer (MRD) using Cu K_α radiation. Angle of incidence (ω), which was optimized for each individual sample, was <0.4°. GIXRD patterns were obtained by performing ten repeated scans within the 2Theta range of 20-80° with a step size of 0.1° and counting time of 10 s. These scans were then added together in order to obtain a single GIXRD pattern. Peak positions and the corresponding interplanar spacing values were obtained by fitting the GIXRD data using PANalytical X'Pert HighScore Plus Software. Using the same software, line profile analysis (LPA) was applied to each GIXRD pattern. Instrumental broadening was corrected using a polycrystalline silicon monitor sample, whose GIXRD data was obtained by performing three repeated scans within the 2Theta range of 10-145° with a step size and counting time of 0.06° and 10 s, respectively.

3.3.1.4 X-Ray Diffraction

X-ray diffraction (XRD) measurements were carried out in a PANalytical X'Pert PRO multi-purpose X-ray diffractometer with Bragg-Brentano Theta-Theta configuration using Cu K_α radiation.

3.3.1.5 Transmission Electron Microscopy and Selected Area Electron Diffraction

FEI Tecnai G2 F30 transmission electron microscope (TEM) operating at a voltage of 300 kV was used for the imaging of samples prepared by FEI Nova 600i Nanolab focused ion beam (FIB) system. Samples were prepared at an acceleration voltage of 30 kV, using various beam currents ranging from 50 pA to 21 nA. Damage layers formed at the film/substrate interfaces were removed by FIB milling at beam voltages of 5 and/or 2 kV. An aperture size of 40 μm was used for obtaining the selected area electron diffraction (SAED) patterns.

3.3.1.6 Atomic Force Microscopy

Asylum Research MFP-3D and Park Systems XE-100 atomic force microscopes operating in the contact mode were used to reveal surface morphologies of III-nitride thin film samples presented in Chapters 4 and 6, respectively.

3.3.1.7 X-Ray Reflectivity

X-ray reflectivity (XRR) measurements were performed by PANalytical X'Pert PRO MRD using Cu K_α radiation. XRR data were fitted by the PANalytical X'Pert Reflectivity Software using a four-layer model; i.e., Al_2O_3 (or Ga_2O_3)/AlN (or GaN)/SiO_2/Si.

3.3.1.8 Spectroscopic Ellipsometry

Ellipsometric spectra were recorded in the wavelength range of 300-1000 nm for AlN, and 400-1200 nm for GaN and $Al_xGa_{1-x}N$ thin films at three angles of incidence (65°, 70° and 75°) using a variable angle spectroscopic ellipsometer (V-VASE, J. A. Woollam) with a rotating analyzer. Optical constants and film thicknesses were extracted using the Cauchy dispersion function using a two-layer model; i.e., Cauchy/Si (0.5 mm). Growth per cycle (GPC) values were determined by dividing film thickness by the number of (PA-)ALD cycles applied.

3.3.1.9 Ultraviolet-Visible Spectrophotometry

Room temperature transmission and absorption measurements presented in Chapter 4 were performed with a Varian Cary 100 ultraviolet-visible (UV-VIS) spectrophotometer. Normal incidence transmission measurements presented in Chapter 6 were performed relative to air within the range of 220-900 nm using an Ocean Optics UV-VIS-near infrared (NIR) single beam spectrophotometer (HR4000CG-UV-NIR).

3.3.1.10 Electrical Characterization

3.3.1.10.1 Fabrication of Metal-Insulator-Semiconductor Capacitor Structures

Metal-insulator-semiconductor (MIS) capacitor structures with AlN as the insulating layer were fabricated on 25 mm × 40 mm p-type Si (100) substrates (resistivity, ρ = 20-40 ohm.cm) using class 100 and 1000 cleanroom facilities (UNAM Cleanroom Facility-UCF). Schematic representation of the fabrication procedure is shown in Figure 3.3. Steps followed for this fabrication process are listed below.

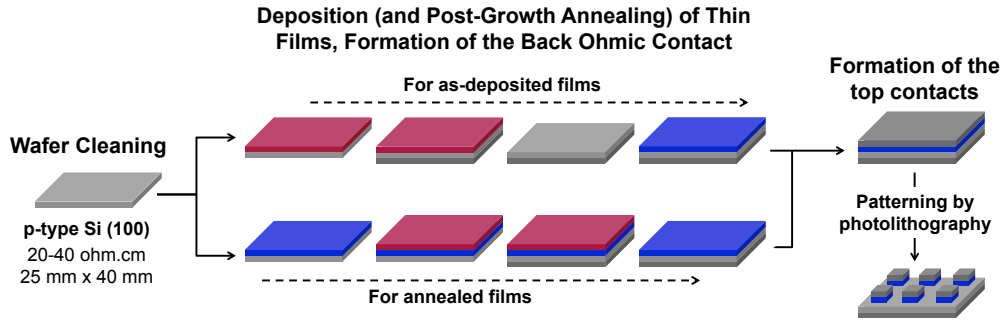

Figure 3.3: Schematic representation of the fabrication procedure for MIS capacitor structures.

1. Wafer cleaning
   (a) solvent cleaning
   (b) piranha etch: 4 volumes sulfuric acid (H_2SO_4) and 1 volume hydrogen peroxide (H_2O_2), 5-10 min
   (c) native oxide removal: 2% HF solution, 2-3 min
2. Formation of the back ohmic contact, then deposition of the insulating AlN layer (for as-deposited AlN films)[1]

[1]For annealed AlN thin films, first the insulating Al layer should be deposited and subjected to post-deposition annealing. Following this, back ohmic contact can be formed by following the steps described below.

(a) protecting the top side with a layer of photoresist: (i) spin-coating[2]AZ 5214 E photoresist: 4000 rpm, 50 s (~1.4 μm photoresist thickness), (ii) dehydration bake: 110 °C, 50-55 s

(b) thermal evaporation[3] of ~80 nm Al

(c) photoresist stripping: washing the samples with acetone, methanol, isopropanol, DI-water, drying with N_2

(d) rapid thermal annealing[4] at 450 °C under N_2 ambient (100 sccm): ramping with 15 °C/s, 2 min at 450 °C

(e) native oxide removal: 2% HF solution, 2-3 min

(f) PA-ALD of AlN at 200 °C: 80, 175, 525 cycles

3. Formation of the top contacts

(a) thermal evaporation of ~80 nm Al

(b) patterning of the Al and AlN layers by photolithography: (i) spin-coating hexamethyldisilazane (HMDS): 5000 rpm, 40 s, (ii) spin-coating AZ 5214 E photoresist: 4000 rpm, 50 s (~1.4 μm photoresist thickness), (iii) dehydration bake: 110 °C, 50-55 s, (iv) exposure[5]: constant dose, 45 mJ, (v) development: 1 volume AZ 400K[6] developer and 4 volumes DI-water, 55 s, (vi) rinsing with DI-water, drying with N_2

Cross-sectional schematic representation of the resulting MIS capacitor structure is given in Figure 3.4.

[2]Spin-coating was carried out using Laurell spinner system.

[3]VAKSIS thermal evaporation system (PVD Vapor 3S Thermal) was used for the back contact metallization.

[4]Samples were annealed using ATV-Unitherm (RTA SRO-704) rapid thermal annealing system.

[5]Photoresist was exposed to UV radiation using EVG620 mask aligner.

[6]Besides being used for photoresist development, AZ 400K also etches the AlN layer [183].

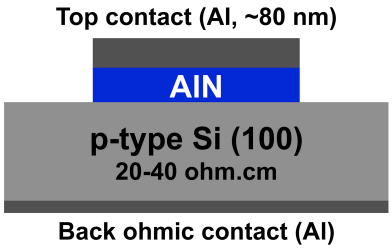

Figure 3.4: Cross-sectional schematic representation of the resulting MIS capacitor structure.

3.3.1.10.2 Capacitance-Voltage and Current-Voltage Measurements

Capacitance-voltage (C-V) and current-voltage (I-V) characteristics of the fabricated MIS capacitor structures were measured under dark using a semiconductor parameter analyzer (Keithley 4200-SCS), which is connected to a probe station (Cascade Microtech PM-5). C-V curves were obtained at a frequency of 1 MHz.

3.3.2 Characterization of AlN Hollow Nanofibers

SEM and energy dispersive X-ray analysis (EDX) studies were carried out using Quanta 200 FEG SEM (FEI) equipped with Ametek Apollo X silicon drift detector (EDAX). Samples used for EDX were uncoated, whereas those used for SEM imaging were coated with ~5 nm Au/Pd alloy. TEM and SAED analyses were performed using a Tecnai G2 F30 transmission electron microscope (FEI). TEM samples were prepared using two different approaches. In the first approach, polymer nanofibers were electrospun directly on copper grids, which were then coated with AlN and calcined *in situ*. Second approach consisted of putting a small piece of AlN hollow nanofiber network into a solvent (i.e., ethanol), followed by sonification to obtain individual hollow nanofibers dispersed through the solvent. AlN hollow nanofiber-containing solvent was then drop casted onto a copper grid and allowed to dry. Chemical composition and bonding states of the AlN nanostructures were investigated by XPS using K-Alpha spectrometer (Thermo Fisher Scientific) with a monochromatized Al K_α X-ray source.

Chapter 4

Plasma-Assisted Atomic Layer Deposition of Aluminum Nitride Thin Films

The work described in this chapter was published in part as:

(1) C. Ozgit, I. Donmez, M. Alevli, and N. Biyikli, "Self-limiting low-temperature growth of crystalline AlN thin films by plasma-enhanced atomic layer deposition," *Thin Solid Films*, vol. 520, no. 7, pp. 2750 - 2755, 2012. DOI: 10.1016/j.tsf.2011.11.081

(2) M. Alevli, C. Ozgit, I. Donmez, and N. Biyikli, "Structural properties of AlN films deposited by plasma-enhanced atomic layer deposition at different growth temperatures," *Physica Status Solidi (A)*, vol. 209, no. 2, pp. 266 - 271, 2012. DOI: 10.1002/pssa.201127430

(3) M. Alevli, C. Ozgit, and I. Donmez, "The influence of growth temperature on the properties of AlN films grown by atomic layer deposition," *Acta Physica Polonica A*, vol. 120, no. 6A, pp. A58 - 60, 2011.

(4) C. Ozgit-Akgun, F. Kayaci, I. Donmez, T. Uyar, and N. Biyikli, "Template-based synthesis of aluminum nitride hollow nanofibers via plasma-enhanced atomic layer deposition," *Journal of the American Ceramic Society*, vol. 96, no. 3, pp. 916 - 922, 2013. DOI: 10.1111/jace.12030

(5) M. Alevli, C. Ozgit, I. Donmez, and N. Biyikli, "The influence of N_2/H_2 and ammonia N source materials on optical and structural properties of AlN films grown by plasma enhanced atomic layer deposition," *Journal of Crystal Growth*, vol. 335, no. 1, pp. 51 - 57, 2011. DOI: 10.1016/j.jcrysgro.2011.09.003

Atomic layer deposition (ALD) of aluminum nitride (AlN) thin films was studied using trimethylaluminum ($AlMe_3$) and ammonia (NH_3) as the Al and N precursors, respectively. Following the thermal ALD, plasma-assisted ALD (PA-ALD) of AlN was investigated at low temperatures using $AlMe_3$ with NH_3 or N_2/H_2 plasma. Process parameters including $AlMe_3$ pulse length, NH_3 (or N_2/H_2) flow rate and duration, purge time, deposition temperature, and plasma power were optimized. AlN thin films were characterized in detail through elemental, structural, surface, optical, and electrical analyses. Conformality of the $AlMe_3$-NH_3 plasma PA-ALD process was also demonstrated by the template-based synthesis of high surface area AlN hollow nanofibers using Nylon 6,6 electrospun nanofibers as sacrificial templates.

4.1 Thermal ALD Using $AlMe_3$ and NH_3

Thermal ALD experiments were carried out within the temperature range of 300-500 °C, where one cycle consisted of 0.5 s $AlMe_3$/10 s Ar purge/7.5 s, 200 sccm NH_3/10 s Ar purge. Figure 4.1(a) shows the growth per cycle (GPC) of AlN at different growth temperatures. Although GPC of 0.07 and 0.14 Å were estimated for 300 and 350 °C, respectively, XPS studies revealed that there is no AlN deposition at 300 °C. For 350 °C, on the other hand, only trace amount of AlN was detected. These results indicate that deposition of AlN with practical rates starts at 400 °C with 0.8 Å/cycle. For higher temperatures, GPC increased with temperature and reached a value of ~2 Å at 500 °C. GPC as a function of precursor doses is also given in Figure 4.1(a). $AlMe_3$ pulse length and NH_3 flow duration (flow rate = 150 sccm) were increased simultaneously from (0.1 s, 1 s) to (2 s, 20 s) at 450 °C. GPC increased with the increasing amount of precursors. Saturation was not observed neither as a function of the temperature nor the precursor doses. Figure 4.1(b) shows the effect of purge time on GPC at 450 °C. GPC decreased from 0.95 to 0.79 Å as the purge time increased from 2 to 10 s, and remained constant at this value for purge times up to 40 s. Purge time of 10 s used in thermal ALD experiments therefore avoids overlapping of the precursor pulses and does not have any effect on the saturation behavior. These

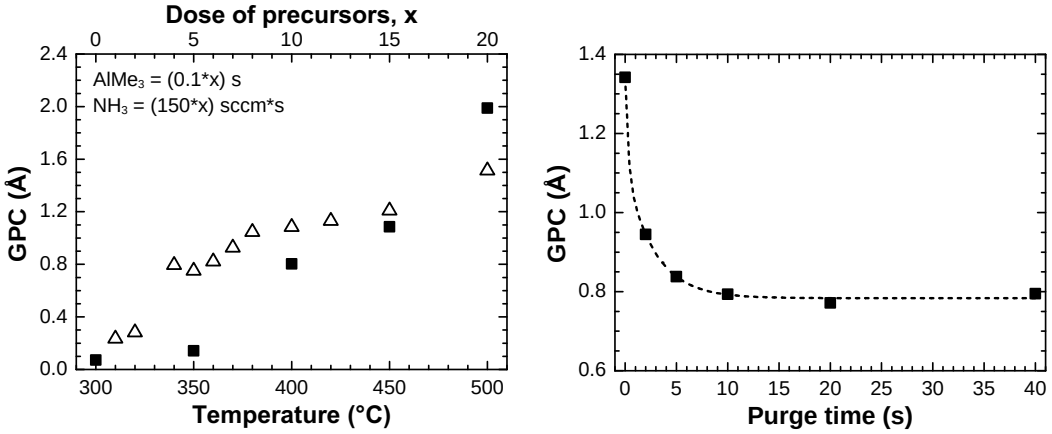

(a) (b)

Figure 4.1: Thermal ALD experiments, where no self-limiting growth behavior was observed. (a) GPC of AlN at different deposition temperatures (■). GPC as a function of $AlMe_3$ and NH_3 doses at 450 °C (△). (b) GPC as a function of purge time at 450 °C. $AlMe_3$ pulse length, NH_3 flow rate and duration were 0.1 s, 150 sccm and 20 s, respectively. Dashed line is for visual aid.

results are in agreement with those reported in the literature [76, 83], where no self-limiting growth behavior was observed due to the fact that surface reactions between $AlMe_3$ and NH_3 occur at temperatures where $AlMe_3$ self-decomposition takes place. Self-limiting growth of AlN is therefore not possible with thermal ALD using $AlMe_3$ and NH_3 precursors. In order to achieve self-limiting surface reactions, $AlMe_3$ (i.e., $Al(CH_3)_3$) self-decomposition must be avoided by the use of lower deposition temperatures. In this respect, high temperatures needed for the NH_3 reaction can be lowered using a plasma-assisted process.

4.2 PA-ALD Using $AlMe_3$ and NH_3 Plasma

4.2.1 Optimization of PA-ALD Parameters

Saturation curves of Al and N precursors obtained by PA-ALD at 185 °C are given in Figure 4.2(a). For the $AlMe_3$ saturation curve, NH_3 flow rate, duration

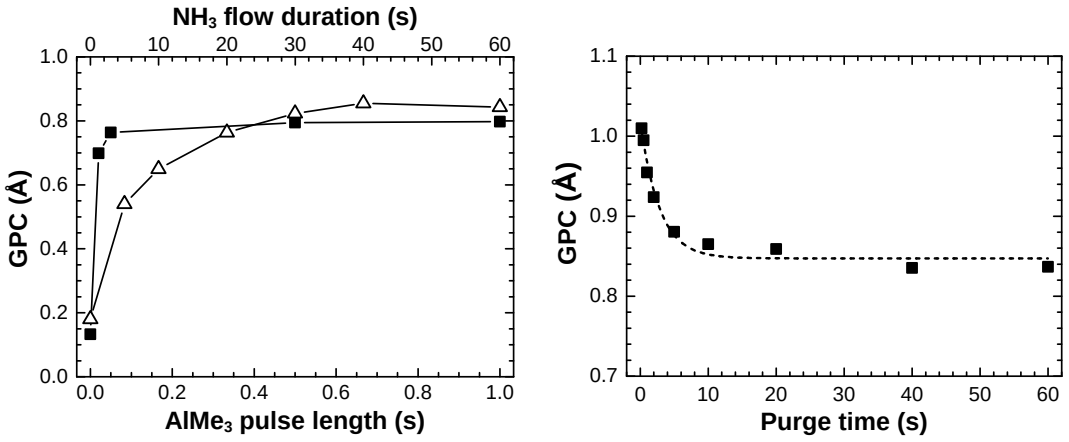

(a) (b)

Figure 4.2: (a) Precursor saturation curves at 185 °C: NH_3 flow duration was kept constant at 20 s for the $AlMe_3$ saturation curve (■), and $AlMe_3$ pulse length was kept constant at 0.05 s for the NH_3 saturation curve (△). (b) GPC as a function of purge time: $AlMe_3$ pulse length and NH_3 flow duration were constant at 0.1 and 40 s, respectively. Dashed line is for visual aid.

and plasma power were kept constant at 50 sccm, 20 s and 300 W, respectively. GPC increased with increasing $AlMe_3$ pulse length until 0.05 s, where GPC saturated at ~0.76 Å. For the NH_3 saturation curve, $AlMe_3$ dose was constant at 0.05 s and NH_3 flow duration was varied with constant flow rate and plasma power (50 sccm, 300 W). GPC increased with increasing NH_3 flow duration until maximum rate of ~0.86 Å was obtained at 40 s. Increasing NH_3 dose to 60 s did not increase GPC. The effect of purge time on GPC was also studied at 185 °C (Figure 4.2(b)). GPC decreased from 1.01 to 0.86 Å as the purge time increased from 0.2 to 10 s. For longer purge times, deposition rate remained almost constant. Increased deposition rates at short purge times are due to insufficient purging, where one precursor is introduced into the reactor before the other one is completely removed. These results show that 10 s purge time is already a good estimation for 185 °C and does not require any further optimization.

GPC of AlN as a function of deposition temperature is shown in Figure 4.3(a). For these experiments, 100 cycle depositions were carried out with cycles consisting of 0.1 s $AlMe_3$/10 s Ar purge/40 s, 50 sccm, 300 W NH_3 plasma/10 s Ar

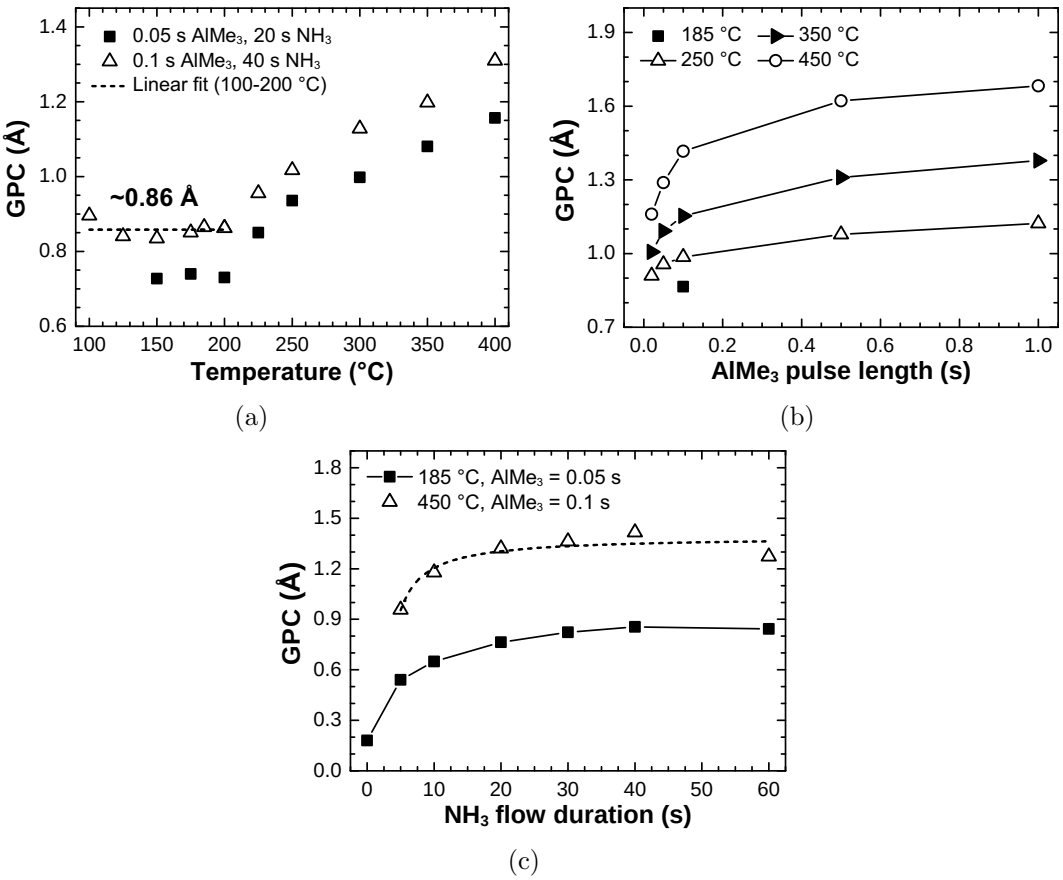

Figure 4.3: (a) Deposition rates of AlN thin films at different temperatures. (b) $AlMe_3$ saturation curves at 185, 250, 350, and 450 °C, where NH_3 flow duration was kept constant at 40 s. (c) NH_3 saturation curves at 185 and 450 °C. Dashed line is for visual aid.

purge. GPC remained constant at ~0.86 Å for temperatures up to 200 °C, and then increased with temperature. Temperature dependency of GPC, observed within the range of 200-400 °C, may be due to the effect of temperature on the number and type of reactive sites present on the surface before and after the chemisorption, or the effect of temperature on the preferred reaction mechanisms [12]. Self-decomposition of $AlMe_3$ molecules may also be responsible from the increasing growth rate with temperature, however this is unlikely since the lowest temperature reported for the decomposition of $AlMe_3$ is ~300 °C [80]. In order to investigate this further, $AlMe_3$ and NH_3 saturation characteristics were studied at higher deposition temperatures. Figure 4.3(b) shows $AlMe_3$ saturation

curves at 185, 250, 350, and 450 °C. As the temperature increased, curves gradually deviated from the self-limiting behavior. NH_3 saturation curves at 185 and 450 °C are given in Figure 4.3(c). As the temperature increased from 185 to 450 °C, GPC increased without any deviation from the self-limiting behavior. Assuming that the decomposition of $AlMe_3$ does not occur until 300 °C, the deviation observed in $AlMe_3$ saturation curve at 250 °C might be due to the increase in saturation $AlMe_3$ dose. $AlMe_3$ dose needed for the saturation of NH_3-terminated surface may increase with temperature if the number of reactive sites or sticking coefficient has temperature dependency [184].

Film thickness vs. number of deposition cycles is presented in Figure 4.4(a). Film thickness increased linearly with increasing number of cycles, confirming that the deposition rate is constant at 185 °C. Slope of the linear fit revealed the GPC at this temperature as 0.85 Å, which is in good agreement with the GPC observed within the ALD temperature window. Results also suggest that deposition starts immediately with the first cycle, without any incubation period. Figure 4.4(b) shows the deposition rate as a function of plasma power at 185 °C. As the plasma power increased from 50 to 100 W, GPC increased from 0.66 to 0.79 Å. As the power further increased to 300 W, GPC increased to 0.86 Å. These results indicate that dissociation efficiency of NH_3 and consequently deposition rate of AlN can be further increased by the use of higher plasma powers; i.e., >300 W.

4.2.2 Characterization of AlN Thin Films

4.2.2.1 Films Deposited Within the ALD Temperature Window

Compositional characterization of ~100 nm thick AlN film deposited on Si (100) at 185 °C was carried out using X-ray photoelectron spectroscopy (XPS). Survey scans detected peaks of Al, N, O, and C at the film surface. In order to reveal atomic concentrations of these elements in the bulk film, same analysis was repeated after the film was etched with a beam of Ar ions for 600 s. Elemental composition of the AlN film was therefore found as 53.93 at.% Al, 41.97 at.% N,

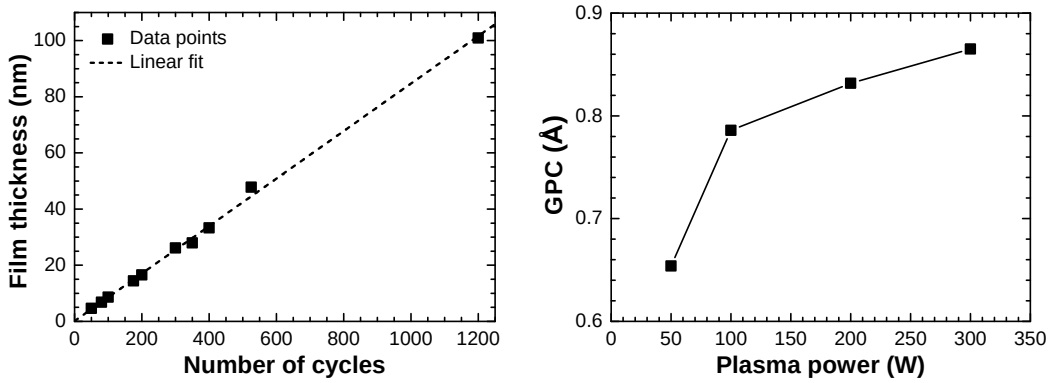

(a) (b)

Figure 4.4: (a) Film thickness vs. number of deposition cycles. (b) GPC of AlN as a function of plasma power. AlN thin films were deposited at 185 °C.

2.28 at.% O, and 1.82 at.% Ar. Ar incorporation is known to occur during ion etching. C was detected only at the film surface and there were no C impurities in the bulk film, indicating that efficient removal of methyl groups from $AlMe_3$ was achieved by the use of NH_3 plasma. Figure 4.5(a) is the compositional depth profile, which indicated constant atomic concentrations for Al and N in the bulk film. Although O concentration was high (~35 at.%) at the film surface, it decayed rapidly within the first 120 s. At 600 s, concentrations of Al, N and O were 59.8, 37.6 and 2.6 at.%, respectively.

O 1s high-resolution XPS (HR-XPS) scan given in Figure 4.5(b) represents the film surface, whereas Al 2p and N 1s scans given in Figures 4.5(c) and 4.5(d) refer to bulk film (t_{etch} = 150 s). O 1s scan was fitted by two peaks located at 529.96 and 531.46 eV, corresponding to Al-O-N [185] and O-Al [186] bonds, respectively. Results, which indicate oxidation at the film surface, are similar to those reported in the literature for air-exposed AlN thin films deposited by plasma source molecular beam epitaxy [186]. Al 2p data was fitted with a single peak at 73.02 eV (Figure 4.5(c)), which is assigned to the Al-N bond [186, 187]. Additional information about the chemical bonding states in the films was provided by the N 1s spectrum that was fitted by two peaks as shown in Figure 4.5(d). N 1s peak at 396.07 eV, which is assigned to the N-Al bond [188], confirms the presence of

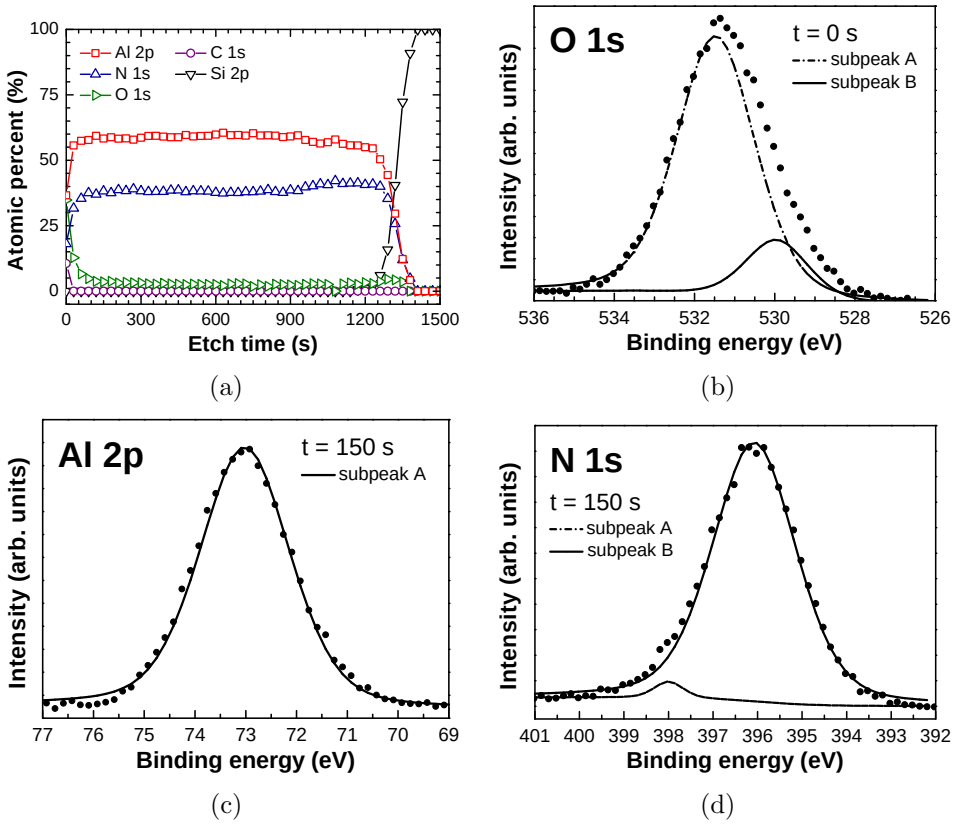

Figure 4.5: (a) Compositional depth profile of ~100 nm thick AlN thin film. (b) O 1s, (c) Al 2p, and (d) N 1s HR-XPS scans.

AlN. Peak at 398.0 eV (N-Al-O bond [186]), on the other hand, corresponds to the <5 at.% O present in the bulk film.

AlN thin films deposited at 185 °C were polycrystalline as determined by grazing-incidence X-ray diffraction (GIXRD). Figure 4.6 shows the GIXRD patterns of ~33 nm thick AlN films (i.e., 400 PA-ALD cycles) simultaneously deposited on Si (100), Si (111), *c*-plane sapphire, metalorganic chemical vapor deposition (MOCVD)-grown GaN on *c*-plane sapphire, and glass (Pyrex) substrates, where (100), (002), (101), (102), (110), (103), and (112) reflections of the hexagonal wurtzite phase were observed (ICDD reference code: 00-025-1133). It should be noted that the reflection labeled as (112) also includes (200) and (201) reflections. 2Theta positions of (200), (112) and (201) reflections are 69.73°, 71.44°

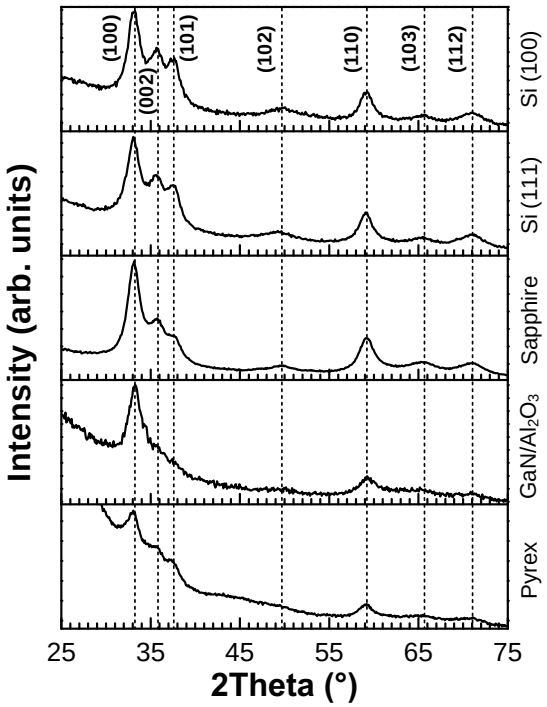

Figure 4.6: GIXRD patterns of ~33 nm thick AlN thin films deposited on Si (100), Si (111), *c*-plane sapphire, MOCVD-grown GaN on *c*-plane sapphire, and glass substrates. GIXRD patterns indicate a hexagonal wurtzite crystal structure.

and 72.63°, respectively. The only difference between the GIXRD patterns given in Figure 4.6 was the relatively more pronounced intensity of (100) reflection for the films deposited on sapphire and GaN/sapphire substrates. Crystallite sizes were determined from these patterns by the line profile analysis (LPA). Crystallite size information was obtained for each individual reflection. An average data was also obtained for each sample from the classical linear Williamson-Hall plot, using the (100), (002), (101), and (110) reflections. (102), (103) and (112) reflections were excluded from the Williamson-Hall plot since their broad profiles and low intensities may lead to errors in the analysis. Moreover, as mentioned earlier, the peak at ~71° consists of multiple reflections, and therefore it is not applicable to LPA. For the sample deposited on glass substrate, (101) reflection was also excluded since the LPA analysis resulted with a negative crystallite size value. From the Williamson-Hall plots, average crystallite sizes were found as

3.5, 3.1, 3.7, 4.3, and 4.7 for AlN thin films deposited on Si (100), Si (111), *c*-plane sapphire, MOCVD-grown GaN on *c*-plane sapphire, and glass substrates, respectively. For a ~100 nm thick AlN thin film deposited on Si (100), crystallite size was measured as 3.8, 3.4, 4.0, and 4.7 from the (100), (002), (101), and (110) reflections, respectively. The average crystallite size value obtained from Williamson-Hall plot was 2.8 nm.

Figure 4.7 is the XRD pattern of ~500 nm thick AlN thin film deposited at 200 °C on Si (111) substrate. In this pattern (100), (002), (101), (102), (110), as well as the (200), (112) and (201) reflections of the *h*-AlN phase were observed, indicating that the deposited AlN layer is randomly oriented.

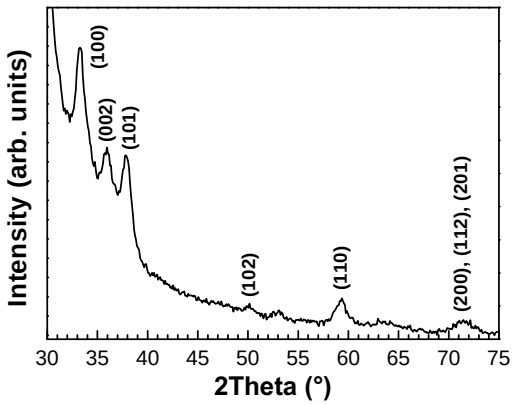

Figure 4.7: XRD pattern of ~500 nm thick AlN thin film deposited at 200 °C on Si (111) substrate.

Figure 4.8(a) is the cross-sectional TEM image of the AlN film deposited on Si (100) at 185 °C. Film thickness was measured as 95.9 nm from this image, which is in good agreement with the results obtained by spectroscopic ellipsometry (SE). Figures 4.8(b) and 4.8(c) are the high-resolution TEM (HR-TEM) images of the same sample, showing a film microstructure consisting of nanometer sized crystallites. Selected area electron diffraction (SAED) pattern of this film is also given in the inset of Figure 4.8(b). In this pattern, reciprocal lattice points correspond to the diamond lattice of Si substrate. Diffraction rings, on the other hand, refer to AlN thin film and indicate a polycrystalline nature. HR-TEM image of the polycrystalline AlN thin film deposited on amorphous glass

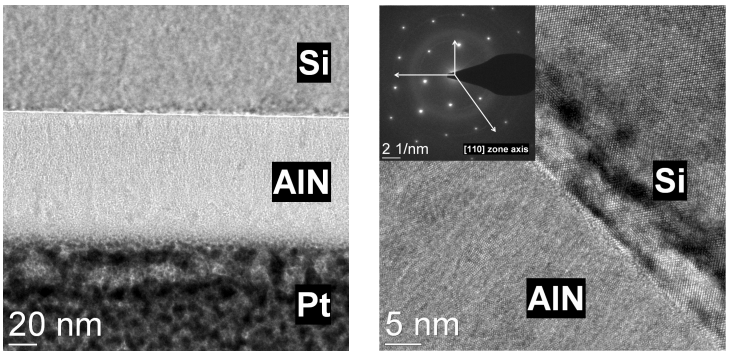

(a) (b)

(c) (d)

Figure 4.8: (a) Cross-sectional TEM image of ~100 nm thick AlN thin film deposited at 185 °C on Si (100). (b), (c) Cross-sectional HR-TEM images, and (inset) SAED pattern of the same sample. (d) Cross-sectional HR-TEM image of AlN thin film deposited on glass substrate.

substrate is given in Figure 4.8(d). SAED pattern of this sample consists of two polycrystalline diffraction rings.

Figures 4.9(a) and 4.9(b) show the surface morphology of ~33 nm thick AlN film deposited on Si (100) substrate. Root-mean-square (rms) roughness of the film was measured as 0.32 nm from a 2 μm × 2 μm scan area. Rms roughness values of the AlN films deposited on GaN/sapphire and sapphire substrates were 0.42 and 0.51 nm, respectively. 2D and 3D AFM images revealing the surface morphology of ~100 nm thick AlN film deposited on Si (100) substrate are given in Figures 4.9(c) and 4.9(d), respectively. As the film thickness increased from ~33 to ~100 nm, rms roughness increased from 0.32 to 1.25 nm.

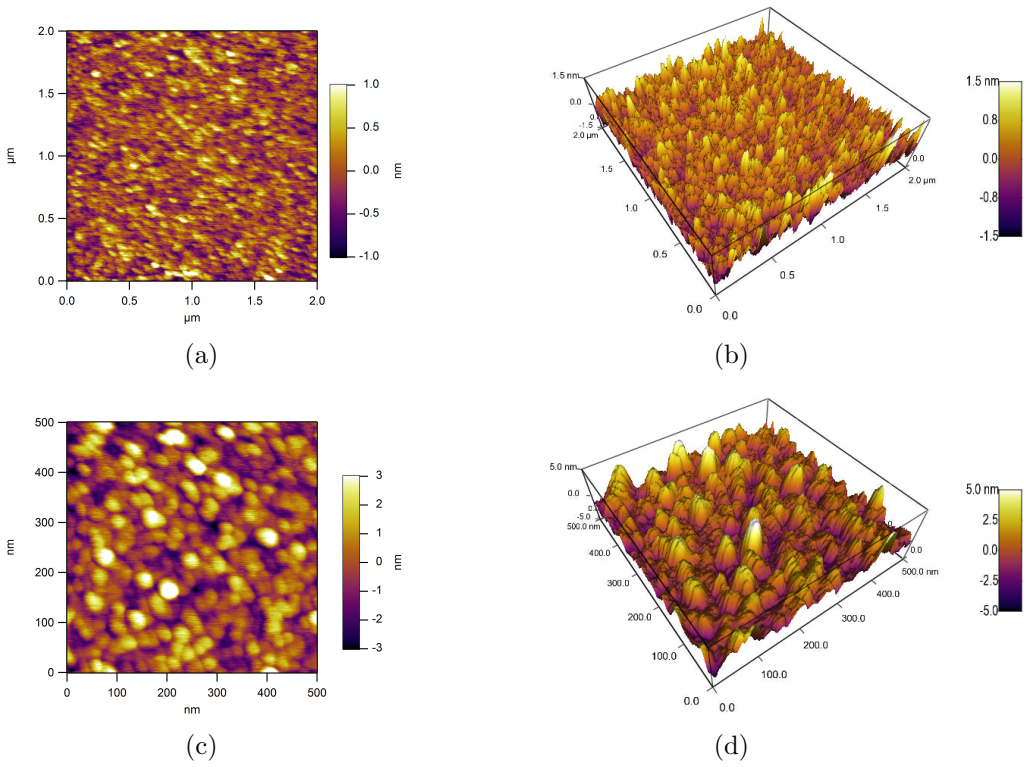

Figure 4.9: (a) 2D and (b) 3D AFM images of ~33 nm thick AlN thin film deposited at 185 °C on Si (100). (c) 2D and (d) 3D AFM images of ~100 nm thick AlN thin film deposited at 185 °C on Si (100).

X-ray reflectivity (XRR) measurements revealed a higher surface roughness value (i.e., 1.90) for the ~100 nm thick AlN film deposited on Si (100) substrate. Thickness (sum of the AlN and Al_2O_3 layer thicknesses in the 4-layer model) and mass density values determined using XRR were 94.6 nm and 2.71 g/cm^3, respectively. This thickness value is slightly lower than that directly measured from the cross-sectional TEM image. The mass density of 2.71 g/cm^3 estimated by XRR is in good agreement with the values recently reported by Bosund et al. for AlN thin films deposited via PA-ALD [112].

Refractive index and extinction coefficient of the AlN film deposited at 185 °C are shown in Figure 4.10(a) as a function of wavelength. Refractive index, which was determined as 2.15 at 270 nm, decreased to 1.88 at 1000 nm. Refractive index of AlN at 632 nm was 1.92. These values are in good agreement with

those reported in literature for polycrystalline AlN thin films [189]. Extinction coefficient (k), which was measured as ~0.03 at 270 nm, decreased rapidly within the wavelength range of 270-335 nm. For higher wavelengths k was almost zero, indicating that the film is transparent in this spectral region. Room temperature transmission spectrum, which was corrected for the substrate and spectrometer response characteristics, is given in Figure 4.10(b) for ~100 nm thick AlN film deposited at 185 °C on double side polished sapphire. Transmission increases with wavelength within the range of 185-350 nm, reaches to 95% at 350 nm and remains >95% until 3 μm. A pronounced reduction of the transmission signal within 235-300 nm is also noteworthy. This absorption band, centered at ~255.5 nm (4.86 eV), was attributed to the oxygen- or vacancy-related defects [190]. Since wurtzite AlN is a direct band gap material and its absorption coefficient is directly proportional to the wavevector value, the square of the product of absorption vs. incident photon wavelength was plotted (inset of Figure 4.10(b)) in order to determine the optical band edge (i.e., absorption edge) [191]. Experimental absorption spectrum of the sample showed that absorption decreases rapidly in the UV spectral range and becomes insignificant in the visible region. A straight-line fitted through the measured data (dashed line shown in the inset

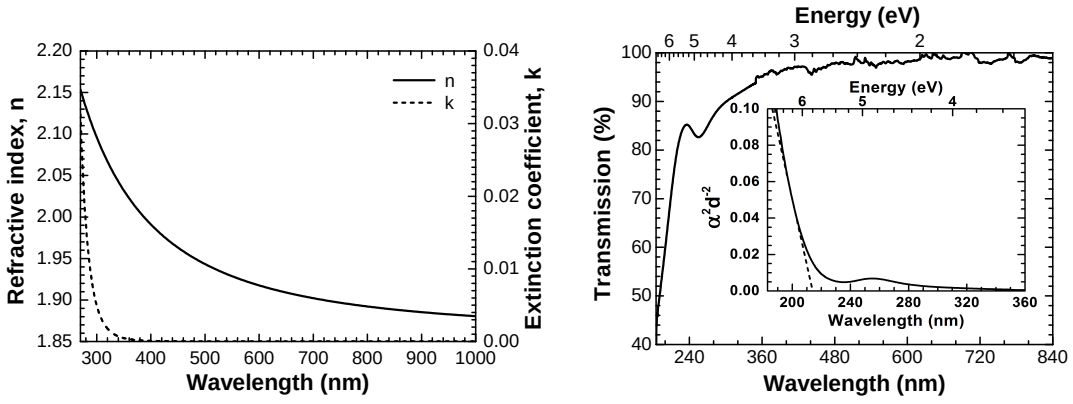

(a) (b)

Figure 4.10: (a) Optical constants (refractive index and extinction coefficient) of ~100 nm thick AlN film deposited on Si (100). (b) Optical transmission spectrum of the film deposited on double side polished sapphire. (Inset) Absorption spectrum of the same sample.

of Figure 4.10(b)) intersects the abscissa at ~5.8 eV, and reveals the optical band edge of AlN thin film deposited by PA-ALD.

Capacitance-voltage (C-V) and current-voltage (I-V) characteristics of the metal-insulator-semiconductor (MIS) capacitor structures with AlN insulating layers deposited by PA-ALD at 200 °C are presented in Figure 4.11. C-V curves given in Figures 4.11(a)-4.11(c) indicated decent interfaces between the Si (100) substrates and AlN dielectric thin films. Although being quite thin, ~7 nm thick AlN thin film exhibited a good dielectric behavior with well-defined accumulation, depletion and inversion regions in its C-V curve (Figure 4.11(a)). Dielectric constants (ε) of AlN films were calculated using the parallel-capacitor model, which is given as

$$C_{acc} \simeq C_{AlN} = \frac{\varepsilon_{AlN}\ \varepsilon_0\ A}{t_{AlN}} \tag{4.1}$$

where C_{acc} is the capacitance at the accumulation region, C_{AlN} is the capacitance of the AlN thin film, ε_{AlN} is the relative permittivity (or dielectric constant) of AlN, ε_0 is the permittivity of free space ($\simeq 8.8542\times10^{-12}$ F/m), A is the area of the capacitor, and t_{AlN} is the thickness of the insulating AlN layer [192]. Figure 4.12 shows the optical microscope images of MIS capacitor structures with ~7 nm thick AlN as the insulating layer. Using Figure 4.12(b), the capacitor area was measured as 5.93×10^{-2} mm^2. Capacitor areas of MIS structures fabricated with ~14 and ~47 nm thick AlN were also calculated from their optical microscope images. By substituting numerical values of C_{acc}, ε_0, A, and t_{AlN} in Eq. 4.1, dielectric constants of ~7, ~14 and ~47 nm thick AlN thin films were calculated as 1.6, 3.2 and 6.8, respectively. These results are in good agreement with literature, where dielectric constants of 6.1-7.0 (t_{AlN} = 75-210 nm), 6.9 (t_{AlN} = 300 nm), 6.9-7.1 (t_{AlN} = 250-340 nm), 7.9 (t_{AlN} = 92 nm), and 4-11.2 (t_{AlN} = 200-1000 nm) were reported for AlN films deposited using atomic layer growth (ALG) [193], RF sputtering [194], reactive dc magnetron sputtering [195], KrF excimer laser sputtering [196], and plasma-enhanced chemical vapor deposition [197], respectively.

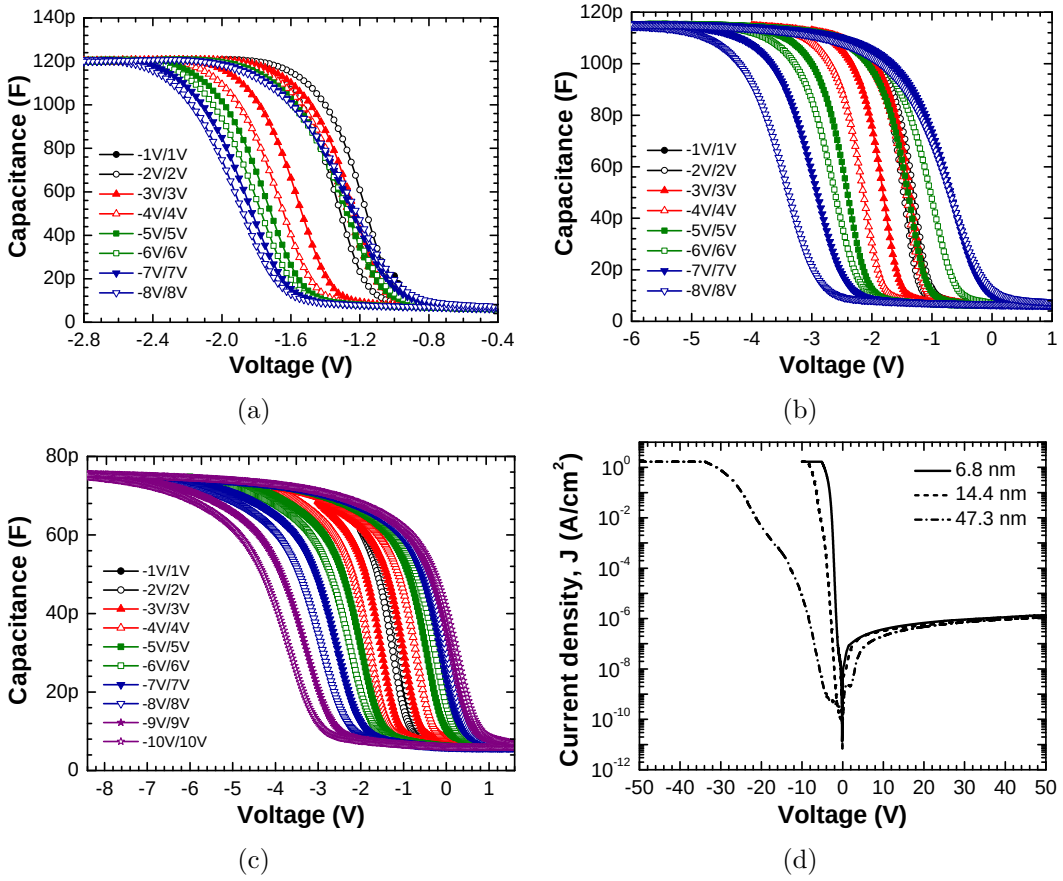

Figure 4.11: (a), (b), (c) C-V characteristics of the MIS capacitor structures with ~7, ~14 and ~47 nm thick AlN insulating layers, respectively. (d) I-V characteristics of the MIS capacitor structures.

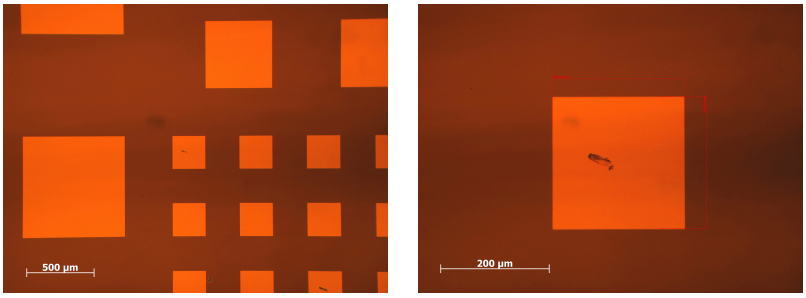

Figure 4.12: Optical microscope images of the MIS capacitor structures with ~7 nm thick AlN as the insulating layer.

I-V characteristics of the fabricated 250 μm × 250 μm MIS structures are given in Figure 4.11(d). Leakage currents were found to be <1 nA for voltages up to 50 V. Moreover, no breakdown was observed within this voltage range.

4.2.2.2 Effect of Deposition Temperature

In order to investigate the effect of deposition temperature on the properties of AlN films, ~100 nm thick films were deposited at 100, 400 and 500 °C using the optimized PA-ALD recipe; i.e., 0.1 s $AlMe_3$/10 s Ar purge/40 s, 50 sccm, 300 W NH_3 plasma/10 s Ar purge. Table 4.1 summarizes the number of cycles applied, resulting film thicknesses measured by SE, corresponding GPC values, and the refractive index (n) values for these samples.

As discussed in Section 4.2.1, ALD window, in which self-limiting growth occurs, covers the deposition temperatures in the range of 100-200 °C. Accordingly, for films deposited at 100 and 185 °C, same number of PA-ALD cycles resulted with similar film thicknesses. GPC values of 1.35 and 1.52 Å were determined for films deposited at 400 and 500 °C, respectively. $AlMe_3$ self-decomposition occurs at deposition temperatures >300 °C [80], therefore for these films chemical vapor deposition (CVD)-type growth is inevitable. Increasing deposition rate with increasing temperature is a well-known characteristic of CVD. As presented in Table 4.1, n increased with deposition temperature, which is probably due to the enhanced crystalline quality and/or density of the AlN films deposited at higher

Table 4.1: SE results of AlN thin films deposited at different temperatures.

Deposition temperature (°C)	Number of cycles applied	Film thickness (nm)	GPC (Å)	n^a
100	1200	97.1	0.81	1.86
185	1200	98.8	0.82	1.91
400	800	107.9	1.35	2.02
500	700	106.1	1.52	2.05

[a] n is the refractive index at 632 nm.

temperatures.

Elemental compositions of AlN thin films deposited at different temperatures are given in Table 4.2. Data were obtained after 600 s of Ar ion etching, and therefore represent the bulk films. There were no C impurities in the deposited AlN films as determined by XPS. The Al/N ratio for films deposited at 100 and 185 °C were 1.27 and 1.28, respectively, which indicate that Al-rich films were deposited within the ALD temperature window. The Al/N ratio increased, and film became more Al-rich as the deposition temperature increased to 400 °C. AlN ratio was 1.36 for films deposited at 400 and 500 °C. It is also worth mentioning that the films deposited at high temperatures had lower O concentrations.

Table 4.2: Elemental compositions of AlN thin films deposited at different temperatures.

Deposition temperature (°C)	Elemental composition (at.%)[a]			
	Al	N	O	Ar[b]
100	53.34	42.13	2.55	1.98
185	53.93	41.97	2.28	1.82
300	55.99	41.02	1.18	1.81
400	55.89	41.10	1.43	1.58

[a] XPS survey scan results, t_{etch} = 600 s.
[b] Ar incorporates into films during Ar ion etching.

Chemical bonding states at the film surface (t_{etch} = 0 s) and in the bulk film (t_{etch} = 300 s) were determined for AlN thin films deposited at 100, 200, 400, and 500 °C by the evaluation of Al 2p HR-XPS scans (Figure 4.13). For all four films, Al 2p HR-XPS scans obtained from the film surface (Figure 4.13(a)) appeared at similar binding energy values and were fitted with two subpeaks. Subpeaks located at higher binding energies (74.2 eV±0.1 eV) correspond to the Al-O bonding state [187], whereas the ones located at lower energies (73.25±0.1 eV) correspond to the Al-N bonding state [186, 187]. Upon Ar ion etching, subpeaks located at higher binding energies (i.e., Al-O bond) disappeared, and therefore Al 2p HR-XPS scans were fitted with a single peak corresponding to the Al-N bonding state. Previously, in addition to the Al-N bonding state, we

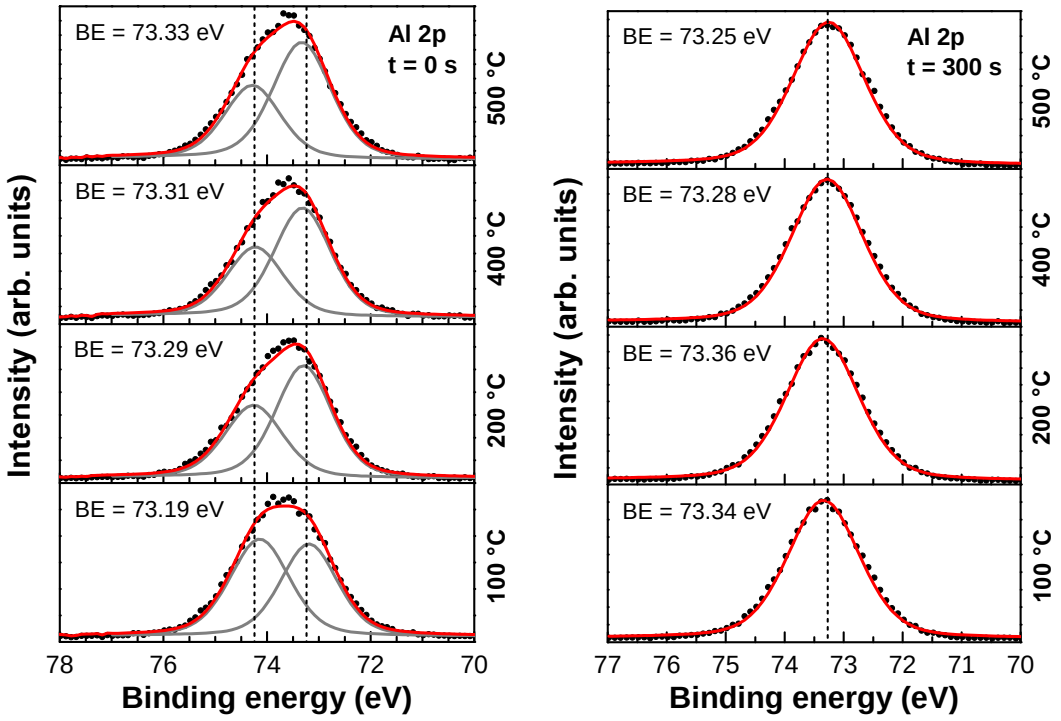

Figure 4.13: Al 2p HR-XPS scans of AlN thin films deposited at different temperatures; (a) t_{etch} = 0 s (i.e., film surface) (b) t_{etch} = 300 s. Binding energy values denoted on each figure correspond to the Al-N bonding state. Dashed lines are for visual aid.

also reported Al-Al bonding for samples deposited at 185 and 400 °C, and Al-O bonding for samples deposited at 100 and 500 °C [198, 199]. However, it should be noted the data presented in those studies were not corrected for charging. When charging effects were corrected by shifting the Al 2p HR-XPS spectra with respect to the adventitious C peak, it has been clearly seen that the deposition temperature does not have any effect on the chemical bonding states of AlN thin films deposited by PA-ALD.

GIXRD patterns of ~100 nm thick AlN films deposited at 100, 185, 400, and 500 °C are given in Figure 4.14. For the films deposited at 400 and 500 °C, higher intensities were observed with smaller full width at half maximum (FWHM) values, which is an indication of enhanced crystallinity and increased

crystallite sizes. The average crystallite sizes of AlN thin films as a function of deposition temperature, as determined from the Williamson-Hall plots, are presented in Figure 4.15. Crystallite size was found to be 2.7 and 2.8 nm for films deposited at 100 and 185 °C, respectively. For higher temperatures crystallite size increased with deposition temperature. As the temperature increased to 400 and 500 °C, average crystallite size values increased to 6.2 and 7.9 nm, respectively.

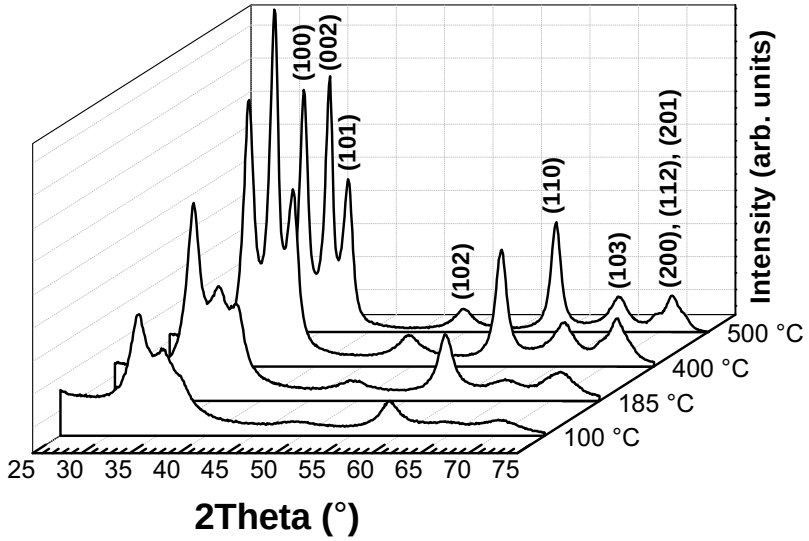

Figure 4.14: GIXRD patterns of ~100 nm thick AlN films deposited on Si (100) substrates at different temperatures.

Thickness, mass density and roughness values for AlN thin film samples deposited at 100, 185, 400, and 500 °C are also presented in Figure 4.15. Film thicknesses measured with SE and XRR were in good agreement for the films deposited at 100 and 500 °C. For the AlN films deposited at 185 and 400 °C, on the other hand, films thickness values estimated by the fitting of XRR data were lower than those measured using SE. Mass density increased from 2.41 to 3.01 g/cm^3 as the deposition temperature increased from 100 to 500 °C. Surface roughness values estimated by XRR were compared to those directly measured by AFM from 500 nm × 500 nm (for sample deposited at 185 °C) and 1 μm ×

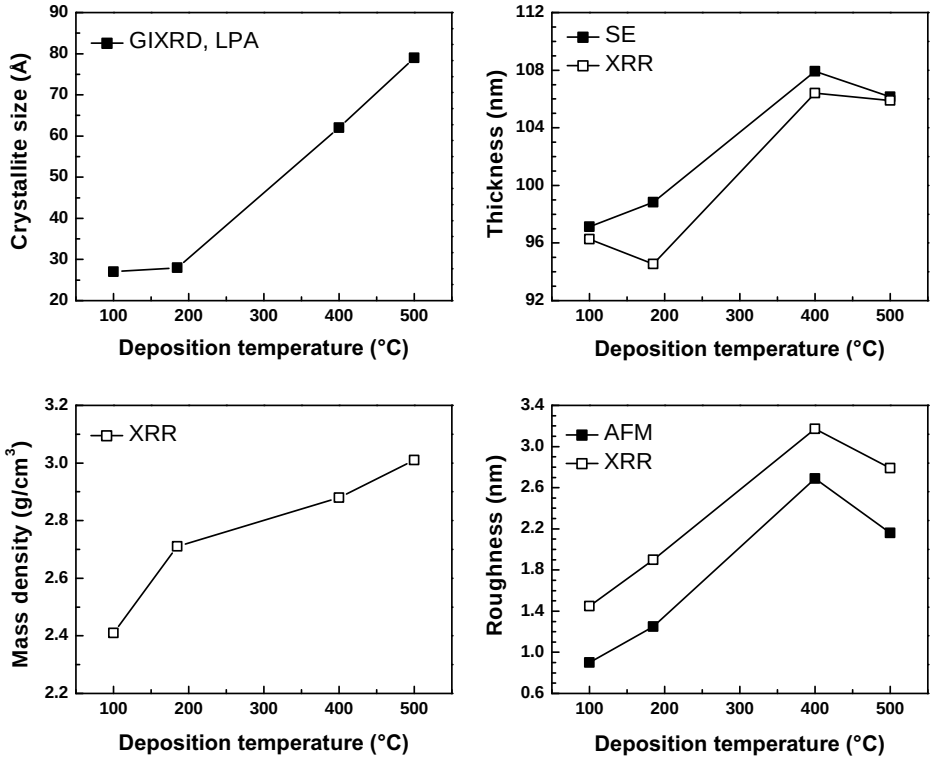

Figure 4.15: Crystallite sizes, thicknesses, mass densities, and roughnesses of AlN thin films as a function of deposition temperature.

1 μm (for AlN films deposited at 100, 400 and 500 °C) scan areas. Although both data sets followed the same trend, roughness values were overestimated by XRR. Roughness decreased from 2.69 to 2.16 nm (as measured by AFM) as the deposition temperature increased from 400 to 500 °C. This was attributed to the increased adatom mobility at higher temperatures, which enables surface diffusion and increases coalescence probability of the nucleation centers (i.e., more CVD-like growth) [198].

Optical properties of AlN thin films deposited at 100, 185, 400, and 500 °C were studied in detail by Alevli et al. using SE, Fourier transform infrared spectroscopy, optical absorption, and photoluminescence. Results of this study can be found in Ref. [200].

4.2.3 Template-Based Synthesis of AlN Hollow Nanofibers

In this section, we report on the template-based synthesis and characterization of AlN hollow nanofibers. The process has three steps (Figure 4.16): (i) preparation of the Nylon 6,6 nanofiber template by electrospinning, (ii) conformal deposition of AlN on the electrospun polymer template via PA-ALD, and (iii) removal of the organic template by calcination.

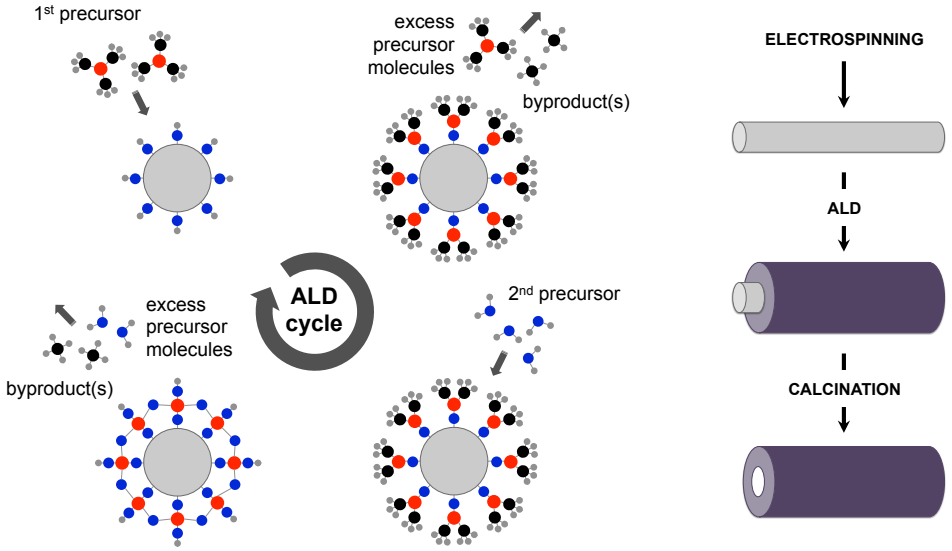

Figure 4.16: (Left) Schematic representation of an ALD cycle. (Right) Template-based synthesis of inorganic hollow nanofibers; preparation of the nanofiber template by electrospinning, conformal deposition on electrospun nanofibers via PA-ALD, and removal of the organic template by calcination.

Nylon 6,6 nanofiber templates having different average fiber diameters were obtained via electrospinning technique. Characteristics (composition and viscosity) of the Nylon 6,6 solutions, together with the morphologies and average fiber diameters of the electrospun Nylon 6,6 nanofibers are summarized in Table 4.3. Type of the solvent used and concentration of polymer solution affected the polymer solution viscosity that is quite important for fiber diameters. Therefore, the viscosity of each Nylon 6,6 solution was different; accordingly, electrospinning

Table 4.3: Properties of Nylon 6,6 solutions and the resulting electrospun nanofibers.

Solvent system	% Nylon 6,6[a] (w/v)	Viscosity (Pa s)	Fiber diameter (nm)	Fiber morphology
Formic acid	8	0.0228	67±35	Bead-free nanofibers
HFIP	5	0.115	330±83	Bead-free nanofibers
HFIP	8	0.24	737±266	Bead-free nanofibers

[a]With respect to the solvent.

of these solutions yielded Nylon 6,6 nanofibers with different fiber diameters. Less stretching of the electrified jet was occurred for more viscous polymer solutions and larger fiber diameters were obtained from these solutions, as it is anticipated [201, 202]. The representative scanning electron microscopy (SEM) images of uniform and bead-free electrospun Nylon 6,6 nanofiber templates having smooth surfaces obtained from 8% (w/v) formic acid, and 5% and 8% (w/v) HFIP solutions are given in Figure 4.17. Average fiber diameters of these Nylon 6,6 nanofibers were measured as 70, 330 and 740 nm, respectively. These randomly oriented Nylon 6,6 nanofibers having different average fiber diameters were used as templates for the fabrication of AlN hollow nanofibers.

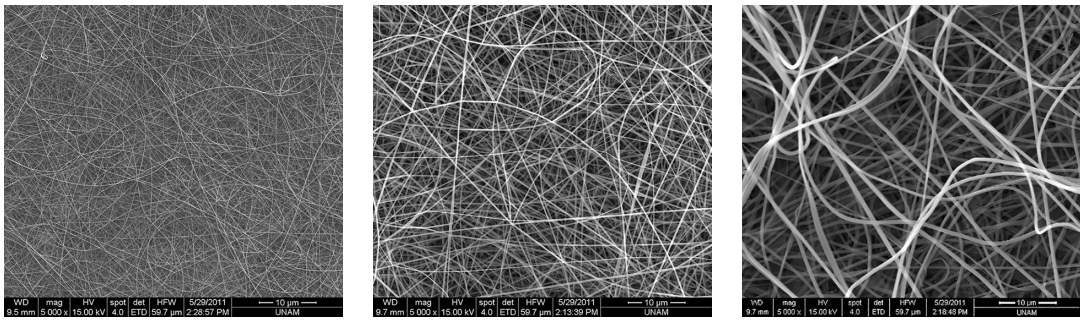

(a) (b) (c)

Figure 4.17: SEM images of electrospun Nylon 6,6 nanofiber templates having (a) 70 nm, (b) 330 nm, and (c) 740 nm average fiber diameters.

Four hundred cycles AlN were deposited on an electrospun template (average fiber diameter 740 nm) at 200 °C by PA-ALD. In Section 4.2.1, we have reported the deposition rate of AlN at this temperature as 0.86 Å/cycle for planar substrates, which corresponds to a ~34 nm thick film for 400 cycle deposition. As expected, the characteristic self-limiting growth mechanism resulted in highly uniform and conformal AlN layers on electrospun Nylon 6,6 nanofibers (Figure 4.18(a)). However, integrity of these conformal layers could not be retained after *ex situ* calcination at air ambient (Figures 4.18(b) and 4.18(c)). Although wall thickness of the resulting inorganic hollow nanofibers could easily be controlled by the number of ALD cycles, there seems to be a critical wall-thickness-to-inner-diameter ratio for ALD-grown layers to preserve their shapes after the sacrificial templates have been removed by calcination.

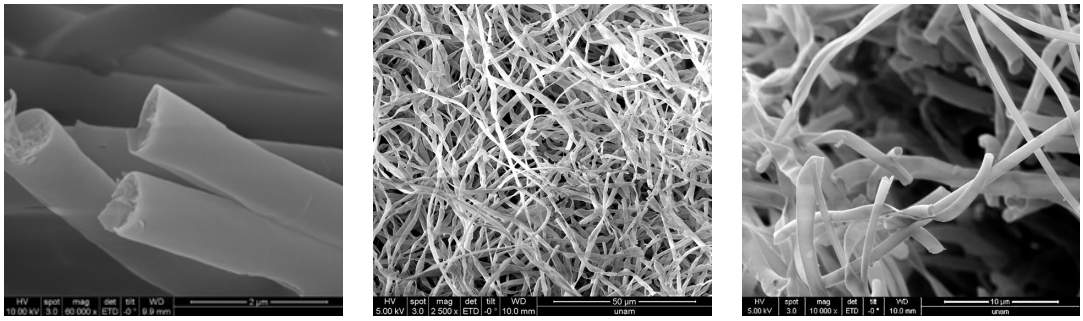

(a) (b) (c)

Figure 4.18: SEM images of (a) Nylon 6,6 nanofibers (average fiber diameter 740 nm) coated with 400 cycles AlN, and (b), (c) inorganic hollow nanofibers synthesized by the *ex situ* calcination of coated nanofibers.

Figure 4.19(a) shows the SEM image of nanostructures synthesized by 800-cycle PA-ALD growth of AlN (corresponding to ~69 nm AlN wall thickness) on ~740 nm diameter fiber templates followed by an *in situ* heat treatment under continuous Ar flow. Resulting structures were hollow, although they have been calcined at an oxygen-free ambient. The critical wall-thickness-to-inner-diameter ratio could not be reached despite the doubled number of ALD cycles. Conformal AlN layer was unable to preserve the cylindrical geometry of the electrospun fiber template, which resulted in a hollow ribbon-like morphology. Figure 4.19(b) is the SEM image of hollow nanofibers synthesized by depositing 800 cycles AlN on a

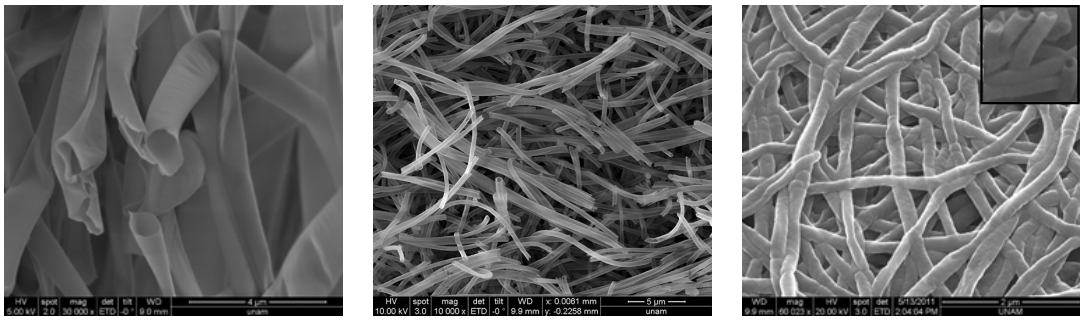

(a) (b) (c)

Figure 4.19: SEM images of hollow nanofibers synthesized by depositing 800 cycles AlN on Nylon 6,6 templates having (a) 740 nm, (b) 330 nm, and (c) 70 nm average fiber diameters. AlN-coated fibers were calcined *in situ*.

template having 330 nm average fiber diameter. For this combination, the resulting structure was an ideal replicate of the electrospun nanofiber template. EDX indicated the presence of Al, N, O, and C in this sample. SEM image of hollow nanofibers synthesized by depositing 800 cycles AlN on a template having 70 nm average fiber diameter is given in Figure 4.19(c). It is seen that individuality of the fibers has been lost due to the coalescence of AlN layers deposited on different fibers. The cross-sectional SEM image of this sample revealed that AlN fibers were hollow (inset of Figure 4.19(c)), yet, the wall-thickness-to-inner-diameter ratio for this combination was too high.

Figure 4.20 belongs to AlN hollow nanofibers synthesized by the deposition of 800 cycles on a template having 330 nm average fiber diameter, followed by *ex situ* calcination. Each fiber was coated with a uniform and conformal layer of AlN. These layers preserved their shapes even after calcination at air ambient and resulted in a structure that is composed of continuous hollow nanofibers.

Bright field scanning TEM image of sample prepared by the deposition of 800 cycles on a template having 70 nm average fiber diameter, followed by *in situ* calcination is given in Figure 4.21(a). It is seen that the wall thicknesses of hollow nanofibers are highly uniform along the fiber axes. Figures 4.21(b)-4.21(d) are the TEM images of samples prepared using templates having average

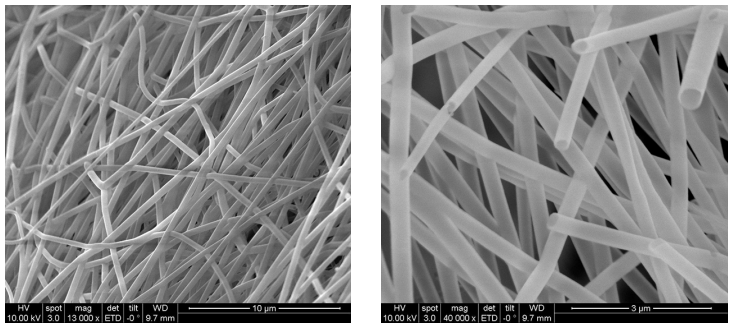

(a) (b)

Figure 4.20: SEM images of AlN hollow nanofibers taken at different magnifications. Hollow nanofibers were synthesized by the deposition of 800 cycles AlN on a Nylon 6,6 template having 330 nm average fiber diameter, followed by *ex situ* calcination at air ambient.

fiber diameters of 70, 330 and 740 nm, respectively. Wall thicknesses of the AlN hollow nanofibers shown in Figures 4.21(b) and 4.21(c) were measured as ~65 nm, which is quite consistent with the deposition rate of AlN PA-ALD process at 200 °C. For the sample shown in Figure 4.21(d), wall thickness was ~32 nm. This value is lower than the expected coating thickness, and might be related to the TEM sample preparation approach that was followed. For the samples shown in Figures 4.21(a)-4.21(c), few nanofibers were electrospun on copper grids, which were then coated and calcined *in situ*. These fibers were at the very top during the PA-ALD of AlN. For the sample shown in Figure 4.21(d), on the other hand, TEM sample was prepared by sonification and drop casting. This individual nanofiber might therefore belong to any position along the out of plane direction. As AlN recipe has been optimized for planar substrates, the precursor doses used in this experiment may not be enough for coating such a high surface area sample. Even if the $AlMe_3$ and NH_3 doses are sufficient for self-terminating reactions to take place at the fiber surface, there may have not been enough time for them to diffuse into the nanofiber matrix.

Crystal structure of the AlN film deposited on Nylon 6,6 nanofiber templates was studied by HR-TEM and SAED. HR-TEM image of the AlN hollow nanofiber synthesized using ~330 nm diameter Nylon 6,6 nanofibers is given

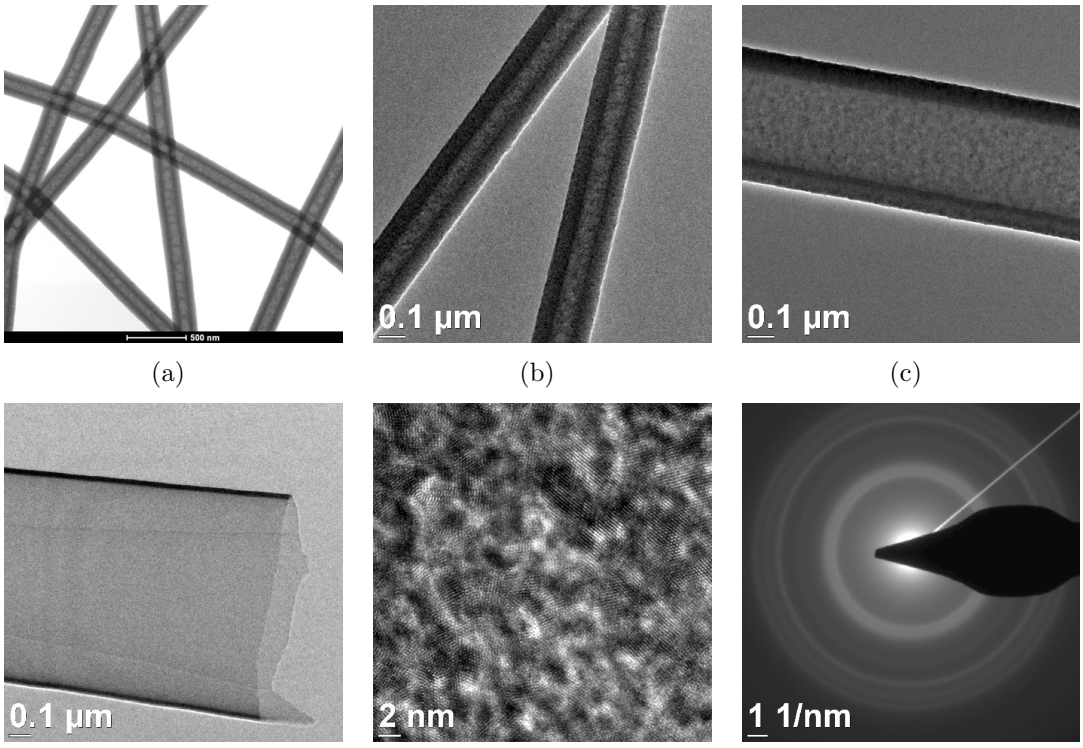

Figure 4.21: AlN hollow nanofibers synthesized by the deposition of 800 cycles AlN, followed by *in situ* calcination. (a) Bright field TEM image of hollow nanofibers synthesized using Nylon 6,6 template having an average fiber diameter of 70 nm. (b)-(d) TEM images of hollow nanofibers synthesized using templates with average fiber diameters of 70, 330 and 740 nm, respectively. (e) HR-TEM image, and (f) SAED pattern of AlN hollow nanofibers synthesized using a template having 330 nm average fiber diameter.

in Figure 4.21(e). AlN was found to be polycrystalline with nanometer-sized grains, which was further confirmed by SAED. SAED pattern of the same sample (Figure 4.21(f)) revealed seven polycrystalline diffraction rings, representing the *h*-AlN phase. Table 4.4 summarizes the SAED results, theoretical values for *h*-AlN and corresponding planes. When same recipe was deposited on planar substrates, the same seven reflections of the *h*-AlN phase appeared in the GIXRD pattern (Section 4.2.2.1, Figure 4.6).

Table 4.4: SAED results, theoretical values and corresponding crystallographic planes.

Diameter (1/nm)	Interplanar spacing, d (Å)		Corresponding plane, hkl
	Calculated	Theoretical[a]	
7.434	2.690	2.6950	100
8.057	2.482	2.4900	002
8.451	2.367	2.3710	101
11.036	1.8123	1.8290	102
12.952	1.5442	1.5559	110
14.199	1.4085	1.4133	103
15.261	1.3105	1.3194	112

[a]Hexagonal AlN, ICDD reference code: 00-025-1133.

Chemical compositions of bare and coated Nylon 6,6 nanofibers, as well as synthesized AlN hollow nanofibers were investigated by XPS, which is a surface analysis technique that collects data from the top ~5-10 nm of the sample. In this study, the relatively large spot size (~400 μm) of the X-ray beam interacted with a large number of coated or calcined nanofibers, which might have discontinuities or cracks on the AlN shell due to the sample preparation procedure applied. Therefore, the collected data probably represent the organic content and Nylon 6,6-AlN interface in addition to the PA-ALD-grown AlN surface. Survey scans detected peaks of Al, N, O, and C for coated and calcined samples prepared by depositing 800 cycles AlN on a template having 330 nm average fiber diameter (Table 4.5). *Ex situ* calcination at 500 °C for 2 h must have resulted in complete removal of the organic component. Accordingly, Al content increased and N content decreased when coated sample was calcined. An increased amount of O is believed to be due to the oxidation of AlN films upon annealing at air ambient. The 19.18 at.% C present in the calcined sample, on the other hand, corresponds either to the surface contamination or calcination residues. XPS survey scan results of *in situ* calcined sample were quite similar to those of coated sample. There was no significant decrease in C concentration upon calcination. In other words, calcination at an oxygen-free ambient was not as effective as that performed at air ambient, although SEM images showed hollow structures for

Table 4.5: XPS survey scan results. Eight hundred cycles AlN were deposited on a template having 330 nm average fiber diameter.

	Elemental composition (at.%)			
Sample	Al	N	O	C
Bare template	-	9.79	11.71	78.50
Coated template	20.69	8.33	33.74	37.24
After *ex situ* calcination	33.02	5.78	42.02	19.18
After *in situ* calcination	21.87	7.51	37.14	33.49

both cases. Results therefore indicate oxidation of AlN layer in the case of *ex situ* calcination and ineffectiveness of *in situ* calcination in terms of removing the organic component.

HR-XPS scans were also obtained to reveal bonding states of AlN hollow nanofibers synthesized at different conditions. Charging effects were corrected for coated and calcined samples using the adventitious C peak located at ~285 eV. C 1s peak of the bare template having 70 nm average fiber diameter was fitted by multiple subpeaks, one of which (corresponding to the surface C contamination) was found to be located at ~285 eV. No correction was therefore made for the bare template. Al 2p HR-XPS scans of hollow nanofibers synthesized by the *in situ* calcination of templates coated with 800 cycles AlN are shown in Figure 4.22(a). As expected, Al 2p peaks were found to locate at the same position for samples synthesized using templates having different average fiber diameters (i.e., 70 and 740 nm). The data obtained from the sample prepared using 740 nm average fiber diameter template was fitted by two subpeaks located at 73.33 and 74.32 eV, corresponding to Al-N [186] and Al-O [187] bonds, respectively. The Al-O bond indicates surface oxidation, which might be expected as the samples were taken out from the ALD reactor and exposed to air at 200 °C. N 1s HR-XPS scans of the samples, as well as that of the bare template having an average fiber diameter of 70 nm are given in Figure 4.22(b). N 1s data obtained from the sample prepared using 740 nm average fiber diameter template were fitted by two subpeaks. The peak located at 396.57 eV was attributed to the N-Al bond [186]; whereas the one located at 399.06 eV was assigned as the N-O bond [188]. The presence of the

N-O bond, which was also observed for the bare Nylon 6,6 template, is a direct proof of the existence of organic component in the sample prepared by *in situ* calcination. The peak representing the N-O bond was also observed for the sample coated with 800 AlN cycles; however, it disappeared after *ex situ* calcination at air ambient. The temperatures required for the removal of sacrificial Nylon 6,6 nanofiber templates are not high and the whole process can be carried out inside the ALD reactor. As Nylon 6,6 nanofibers could not be completely removed through heat treatment at an oxygen-free ambient, the gas composition and gas flow rates must be adjusted accordingly during calcination.

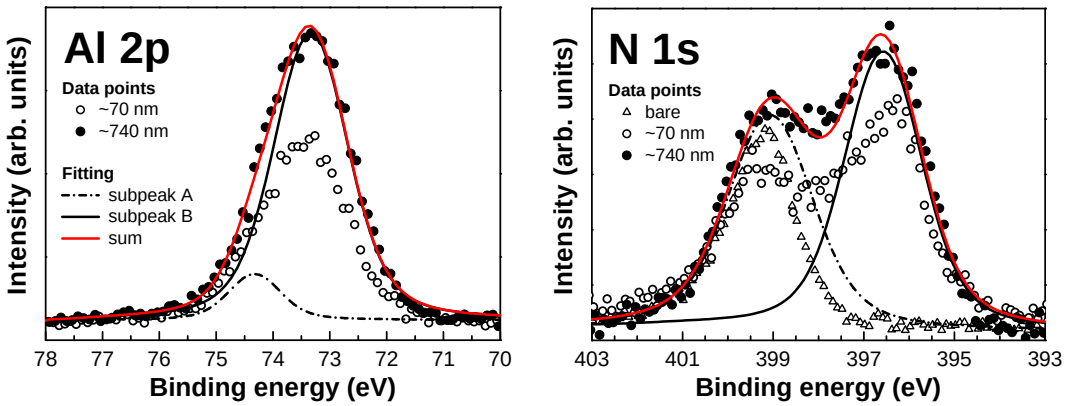

(a) (b)

Figure 4.22: (a) Al 2p and (b) N 1s HR-XPS scans of AlN hollow nanofibers synthesized by depositing 800 cycles AlN on Nylon 6,6 templates having 70 and 740 nm average fiber diameters, which was followed by *in situ* calcination. N 1s HR-XPS scan of bare Nylon 6,6 nanofiber template having an average fiber diameter of 70 nm is also included.

Al 2p HR-XPS scans of coated and calcined (both *in situ* and *ex situ*) samples prepared using polymeric templates having 70 nm average fiber diameter were all fitted by two subpeaks located at 73.5±0.2 (Al-N bond) and 74.5±0.3 eV (Al-O bond). Figure 4.23 shows the Al 2p HR-XPS scans of calcined samples. When compared with that prepared by *ex situ* calcination, the sample prepared by *in situ* calcination exhibited a lower Al-O/Al-N subpeak area ratio (0.18 vs. 0.86) as expected.

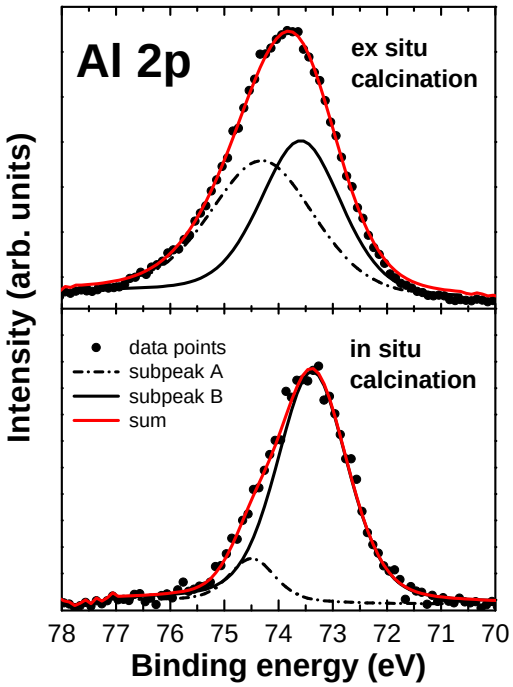

Figure 4.23: Al 2p HR-XPS scans of AlN hollow nanofibers synthesized by the deposition of 800 cycles AlN on Nylon 6,6 nanofiber templates (average fiber diameter 70 nm), followed by *in situ* and *ex situ* calcinations.

4.3 PA-ALD Using $AlMe_3$ and N_2/H_2 Plasma

4.3.1 Optimization of PA-ALD Parameters

A series of depositions were carried out in order to determine the most appropriate N_2/H_2 flow rate ratio. Results are presented in Figure 4.24(a). First, H_2 flow rate was varied while keeping all the other variables constant. 100 cycles were deposited at 185 °C on Si (100) substrates, using 0.1 s $AlMe_3$/10 s Ar purge/40 s, 50 sccm N_2 + x (x = 0, 25, 50, or 100) sccm H_2, 300 W N_2/H_2 plasma/10 s Ar purge. GPC, which was found to be 1.24 Å for x = 0, decreased to 0.59, 0.58 and 0.51 Å as the H_2 flow rate increased to 25, 50 and 100 sccm, respectively. Similar experiments have also been done for optimizing the N_2 flow ratio. 100 cycles were deposited at 185 °C using 0.1 s $AlMe_3$/10 s Ar purge/40 s, y (y =

0, 25, 50, or 100) sccm N_2 + 50 sccm H_2, 300 W N_2/H_2 plasma/10 s Ar purge. GPC, which was 0.31 Å for y = 0, increased to 0.65 Å when 25 sccm N_2 was introduced together with 50 sccm H_2 during the second half-cycle. GPC for y = 50 and 100 sccm were 0.60 and 0.53 Å, respectively. As seen from Figure 4.24(a), similar GPC values were obtained for all combinations, where x, y ≠ 0. Therefore, subsequent depositions were carried out using a flow rate ratio of 1; i.e., flow rates of N_2 and H_2 were both set to 50 sccm.

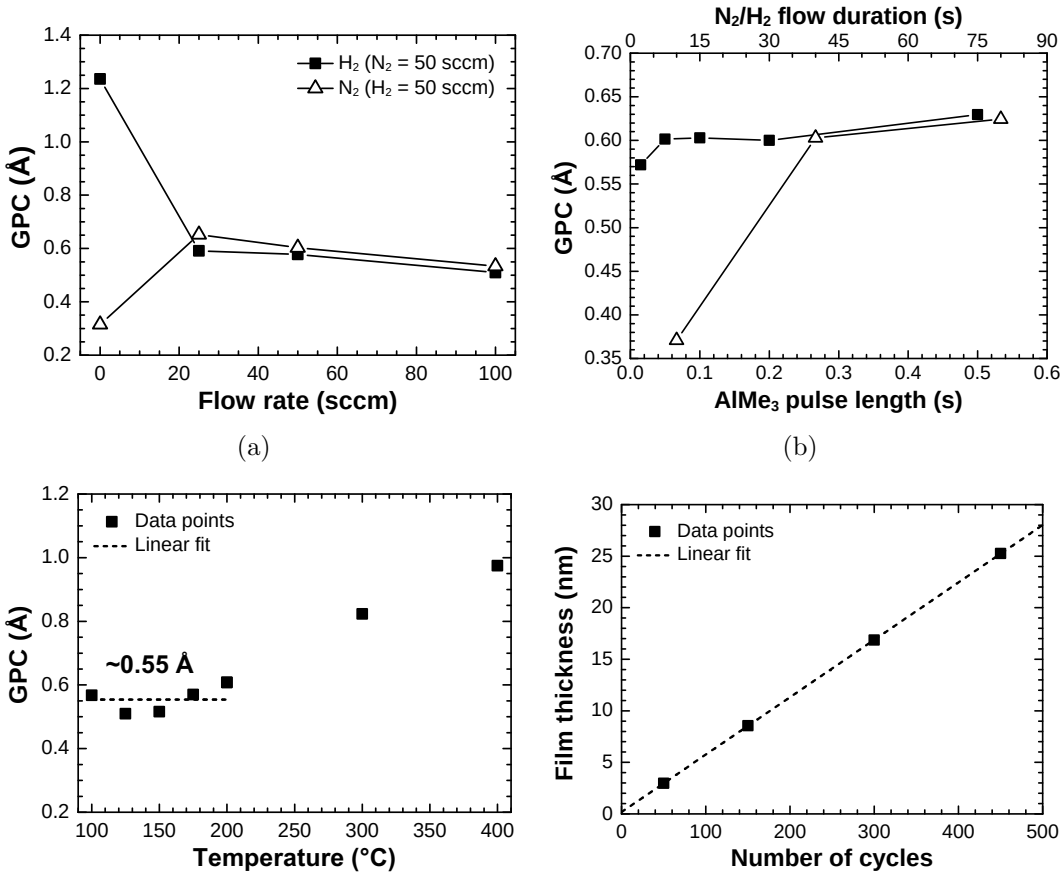

Figure 4.24: Optimization of PA-ALD process parameters for AlN using $AlMe_3$ and N_2/H_2 plasma as the group-III and -V sources, respectively. (a) GPC as a function of N_2 or H_2 flow rate. (b) $AlMe_3$ (■) and N_2/H_2 (△) saturation curves at 185 °C. (c) GPC values for AlN thin films deposited at different temperatures. (d) Film thickness vs. number of deposition cycles at 175 °C.

$AlMe_3$ saturation curve was obtained at 185 °C using the same recipe (Figure 4.24(b)). GPC increased from 0.57 to 0.60 Å as the $AlMe_3$ pulse length increased from 0.015 to 0.05 s, and remained constant at this value when $AlMe_3$ pulse length was further increased to 0.2 s. N_2/H_2 saturation curve is also given in Figure 4.24(b)), where flow duration was varied with constant flow rate and plasma power (50 + 50 sccm, 300 W). $AlMe_3$ pulse length and purge time were 0.1 and 10 s, respectively. Saturation was observed at 40 s, with a GPC of 0.60 Å. Increasing the N_2/H_2 duration to 80 s resulted in a very slight increase (i.e., ~0.02 Å) in GPC.

The effect of growth temperature on GPC was investigated by depositing 150 cycles AlN at various temperatures using the following recipe: 0.05 s $AlMe_3$/10 s Ar purge/40 s, 50 + 50 sccm, 300 W N_2/H_2 plasma/10 s Ar purge. Results, which are plotted in Figure 4.24(c), were similar to those obtained for the NH_3 plasma process (Section 4.2.1), with only difference being the decreased GPC. GPC remained constant at ~0.55 Å for temperatures up to 200 °C, and then increased with temperature. Therefore, the ALD temperature window for the $AlMe_3$-N_2/H_2 plasma process was determined as 100-200 °C.

Film thickness vs. number of deposition cycles plot is given in Figure 4.24(d). At 175 °C, film thickness increased linearly with increasing number of cycles, confirming that the GPC is constant at this given temperature. Slope of the linear fit revealed the GPC at this temperature as 0.56 Å, which is in good agreement with the value observed within the ALD temperature window. Results also showed that deposition starts immediately with the first cycle, without any incubation period.

4.3.2 Characterization of AlN Thin Films

AlN thin films were prepared by the deposition of 1400 PA-ALD cycles at 185 °C using 0.05 s $AlMe_3$/10 s Ar purge/40 s, 50 + 50 sccm, 300 W N_2/H_2 plasma/10 s Ar purge. Although in the previous section it has been stated that 0.05 s $AlMe_3$

is enough for having saturated surface reactions, the process resulted in non-uniform films. For 4 in. Si (100) substrate, which has been placed at the center of substrate holder, AlN thickness decreased from center to edges, as determined visually from the color variations. SE results confirmed this observation, and the film thickness at the center was measured as 83.8 nm. Unless stated otherwise, characterization studies were performed using the central region of this sample.

Chemical composition and bonding states were determined by XPS. Survey scan detected peaks of Al, N, O, and C at the film surface. There were no C impurities in the bulk film. Atomic concentrations of Al and N were constant in the film as determined by the compositional depth profile. Elemental composition of the AlN film (t_{etch} = 600 s) was found from the survey scan as 55.16 at.% Al, 41.15 at.% N, 1.77 at.% O, and 1.93 at.% Ar. Atomic concentration of Al increased, and that of N decreased slightly when N_2/H_2 plasma was used as the N precursor instead of NH_3 plasma. Al/N ratio, which was 1.28 for AlN films deposited using NH_3 plasma process, increased to 1.34 for the samples deposited with N_2/H_2 plasma. Al 2p and N 1s HR-XPS spectra indicated the exactly same bonding states reported in Section 4.2.2 for AlN films deposited using NH_3 plasma. Al 2p HR-XPS scan obtained from the bulk film (t_{etch} = 300 s) was fitted with a single peak, which is located at 73.2 eV. This peak was attributed to the Al-N bonding state [186, 187]. N 1s spectrum, on the other hand, was fitted by two peaks. Peaks located at 397.6 and 396.17 eV were assigned as the N-Al-O [186] and N-Al [188] bonds, respectively.

GIXRD pattern of the AlN thin film deposited using N_2/H_2 plasma at 185 °C is given in Figure 4.25 together with that obtained from a ~100 nm thick AlN film deposited using NH_3 plasma at the same temperature. Both patterns exhibited (100), (002), (101), (102), (110), (103), and (112)[1] reflections of the hexagonal wurtzite phase. Crystallite size data were determined for the AlN thin film deposited by N_2/H_2 PA-ALD process from its GIXRD pattern using LPA. For a ~84 nm thick AlN thin film deposited on Si (100), crystallite size was measured as 4.8, 3.1, 3.7, and 4.2 nm from the (100), (002), (101), and (110) reflections,

[1]The reflection labeled as (112) also includes (200) and (201) reflections. 2Theta positions of (200), (112) and (201) reflections are 69.73°, 71.44° and 72.63°, respectively.

respectively. The average crystallite size value obtained from the Williamson-Hall plot was 3.2 nm. Polycrystalline nature of the AlN film was also confirmed by cross-sectional HR-TEM imaging (Figures 4.26(a) and 4.26(b)). SAED pattern of the sample revealed polycrystalline diffraction rings.

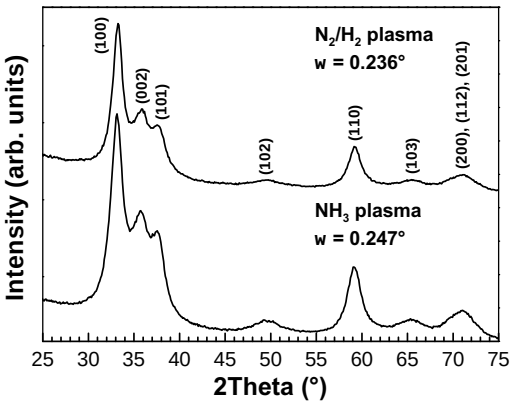

Figure 4.25: GIXRD patterns of AlN thin films deposited at 185 °C on Si (100) substrates using $AlMe_3$-NH_3 and $AlMe_3$-N_2/H_2 PA-ALD processes.

2D and 3D surface morphologies of ~84 nm thick AlN film deposited on Si (100) substrate are presented in Figures 4.27(a) and 4.27(b), respectively. Rms roughness of the film was measured as 1.03 nm from a 500 nm × 500 nm scan area. Roughness determined by XRR was 1.97 nm. XRR also revealed the mass density of the film as 2.61 g/cm^3, which is slightly lower than the value estimated for the film deposited using NH_3 plasma (i.e., 2.71 g/cm^3).

Refractive index of the AlN thin film deposited using N_2/H_2 plasma at 185 °C was measured as 1.92 at 632 nm. Refractive index of the film deposited with NH_3 plasma was also 1.92 nm at the same wavelength (Section 4.2.2). From the transmission spectra, the transmission onset was determined as 188 nm. Optical band edge was determined from the absorption spectra as 5.92 eV, which is slightly higher than the value estimated for AlN film deposited using NH_3 plasma.

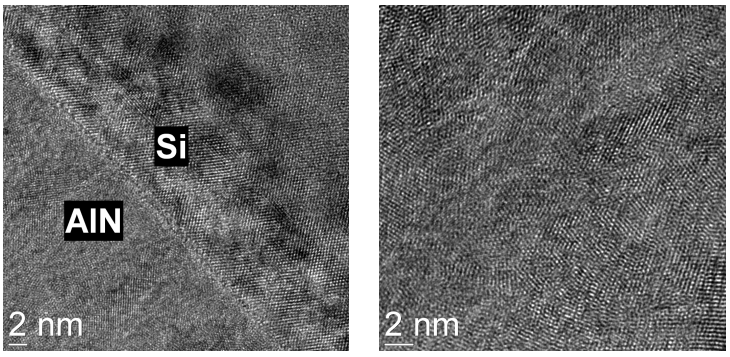

(a) (b)

Figure 4.26: Cross-sectional HR-TEM images of ~84 nm thick AlN thin film deposited at 185 °C on Si (100) substrate using $AlMe_3$-N_2/H_2 PA-ALD process.

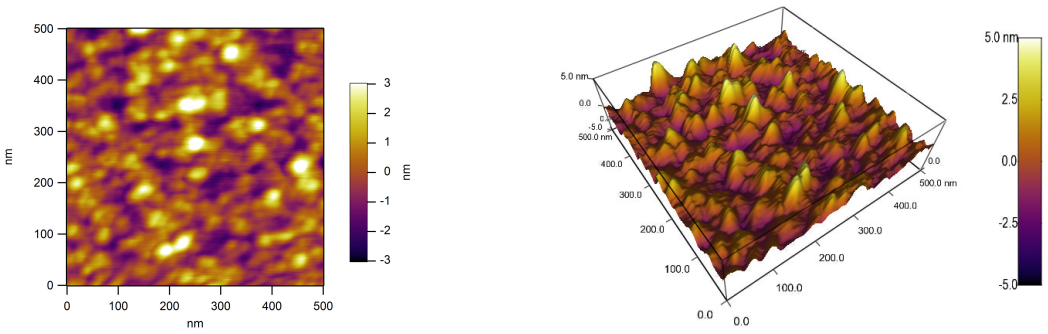

(a) (b)

Figure 4.27: (a) 2D and (b) 3D AFM images of ~84 nm thick AlN thin film deposited at 185 °C on Si (100) using $AlMe_3$-N_2/H_2 PA-ALD process.

Chapter 5

The Indication of Plasma-Related Oxygen Contamination in III-Nitride Thin Films

The work described in this chapter was published in part as:

(1) C. Ozgit, I. Donmez, M. Alevli, and N. Biyikli, "Atomic layer deposition of GaN at low temperatures," *Journal of Vacuum Science and Technology A*, vol. 30, no. 1, pp. 01A124 (4pp), 2012. DOI: 10.1116/1.3664102

(2) C. Ozgit, I. Donmez, and N. Biyikli, "Self-limiting growth of GaN at low temperatures," *Acta Physica Polonica A*, vol. 120, no. 6A, pp. A55 - A57, 2011.

(3) C. Ozgit-Akgun, I. Donmez, and N. Biyikli, "Plasma-enhanced atomic layer deposition of III-nitride thin films," *ECS Transactions*, vol. 58, no. 10, pp. 289 - 297, 2013. DOI: 10.1149/05810.0289ecst

Plasma-assisted atomic layer deposition (PA-ALD) of gallium nitride (GaN) and indium nitride (InN) thin films were studied using trimethylgallium ($GaMe_3$), triethylgallium ($GaEt_3$), trimethylindium ($InMe_3$), and cyclopentadienyl indium (CpIn) precursors with ammonia (NH_3) plasma. $GaMe_3$-NH_3 and $GaEt_3$-NH_3 plasma processes were optimized for true ALD conditions. As the deposited films were characterized in detail through elemental and structural analyses, it has been realized that the films contain high concentrations of O. Although - at first - the most probable source of this contamination was presumed as the O-containing impurities in the 5N-grade NH_3 gas, subsequent experiments revealed the true source as the quartz tube of inductively coupled RF-plasma (ICP) source itself. Accordingly, different plasma gas compositions were studied with lower plasma durations as an attempt to minimize the plasma-related oxygen contamination in III-nitride thin films.

5.1 PA-ALD of GaN Thin Films

5.1.1 PA-ALD Using $GaMe_3$ and NH_3 Plasma

5.1.1.1 Optimization of PA-ALD Parameters

GaN thin films were deposited on Si (100) substrates by PA-ALD using $GaMe_3$ and NH_3. Effect of $GaMe_3$ pulse length on GPC was investigated at 185 °C with a constant NH_3 flow duration of 40 s (Figure 5.1(a)). $GaMe_3$ pulse lengths of 0.015 and 0.03 s resulted with the same growth per cycle (GPC), i.e., 0.46 Å; indicating that 0.015 s is high enough for saturative surface reactions to take place. Figure 5.1(b) shows GPC as a function of NH_3 flow duration. $GaMe_3$ pulse length and NH_3 flow rate were constant at 0.015 s and 50 sccm, respectively. GPC increased with NH_3 flow duration until 90 s and reached saturation at ~0.56 Å. Using the saturation value of NH_3 exposure step (50 sccm, 90 s), saturation behavior of $GaMe_3$ was restudied. Since $GaMe_3$ has a very high vapor pressure at room temperature (~228 Torr at 25 °C), even the minimum pulse

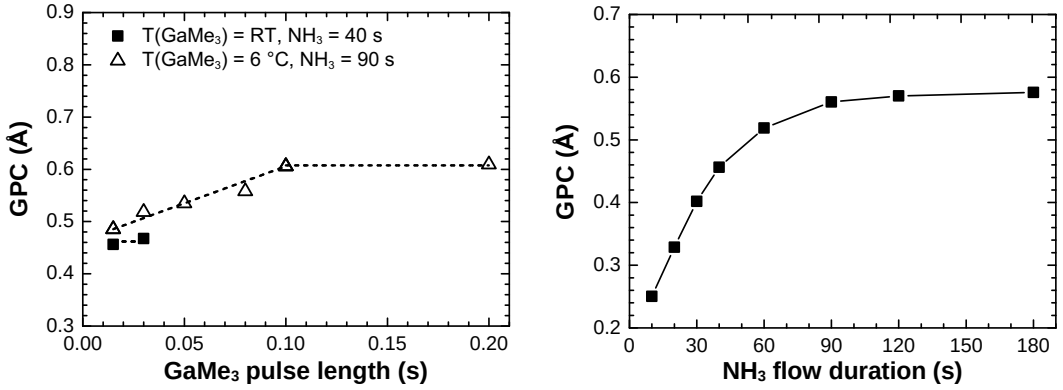

(a) (b)

Figure 5.1: (a) $GaMe_3$ saturation curves at 185 °C for different $GaMe_3$ temperatures. NH_3 flow rate was constant at 50 sccm. Dashed lines are for visual aid. (b) NH_3 saturation curve at 185 °C. $GaMe_3$ pulse length was 0.015 s.

length (i.e., 0.015 s) might be resulting in doses much higher than the saturation dose. The excessive usage of $GaMe_3$ can be avoided by lowering the temperature of $GaMe_3$ until a decrease in deposition rate is observed. Therefore, we cooled down the $GaMe_3$ precursor using a home-made Peltier cooling system, stabilized its temperature at 6 °C, and restudied its saturation behavior. The results are given in Figure 5.1(a). GPC increased with $GaMe_3$ pulse length within the range of 0.015-0.1 s. For 0.1 s and higher $GaMe_3$ pulse lengths, saturation was observed at ~0.61 Å.

In order to determine the temperature range at which the GPC is constant (i.e., the ALD window), 100 cycles with 0.015 s $GaMe_3$ (T_{GaMe_3} = 25 °C) and 90 s NH_3 plasma were deposited at different temperatures. GPC vs. temperature graph consisted of four distinct regions (Figure 5.2(a)). GPC was constant at ~0.51 Å in region III (250-350 °C), implying that the growth of GaN at these temperatures is self-limiting. For temperatures in the range of 185-250 °C (region II), deposition rate increased with decreasing temperature. GPC was ~0.56 Å at 185 °C. Since this behavior might be related to the purging efficiency, which decreases with decreasing temperature, the effect of purging duration on deposition rate was investigated at 185 °C. An experiment has been carried out by

doubling the purge time. Deposition rate obtained using 20 s purge time was found to be same as that obtained using 10 s, which indicates that the observed behavior is not due to the overlapping of precursor molecules and plasma radicals as a result of inefficient purging. Figure 5.2(b) shows GPC as a function of purge time at 185 °C. Being different than the above-mentioned purge time experiment, $GaMe_3$ was cooled down to 6 °C and stabilized at this temperature prior to depositions. GPC decreased from 0.63 to 0.53 Å as the purge time increased from 2 to 10 s. For longer purge times, GPC remained almost constant; it was ~0.52 Å for depositions carried out using 20 and 40 s purge times. Although GPC has an obvious temperature dependency in region II, both $GaMe_3$ and NH_3 precursors showed saturation behaviors at 185 °C. Since growth was proven to be self-limiting at 185 °C, region II has been also included to the ALD window. Region I (100-185 °C) corresponds to the activation energy limited zone, where deposition rate decreases at low temperatures due to the decrease in thermal energy. For ~385 °C and higher temperatures (region IV) growth rate increased with temperature, which is probably due to the decomposition of $GaMe_3$. Depending on these observations, upper and lower limits of the ALD window, in which surface reactions take place in a self-limiting fashion, were estimated as ~385 and 185 °C, respectively.

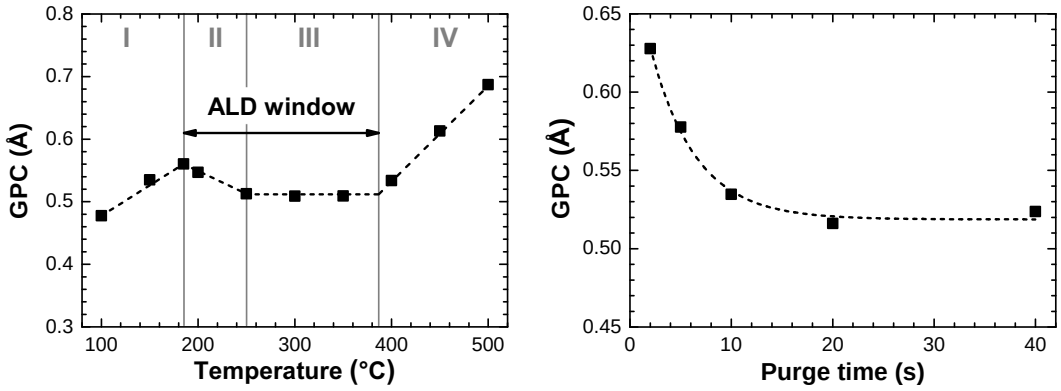

(a) (b)

Figure 5.2: (a) GPC values for GaN thin films deposited at different temperatures. (b) GPC as a function of purge time at 185 °C. Dashed lines are for visual aid.

Film thickness vs. number of deposition cycles at 250 °C is given in Figure 5.3. As seen from this figure, film thickness increases linearly with the number of cycles, confirming that the GPC is constant at this temperature due to the self-limiting nature of the ALD process. Slope of the linear fit revealed the GPC at this temperature as 0.39 Å, which is lower than the GPC observed within the ALD temperature window.

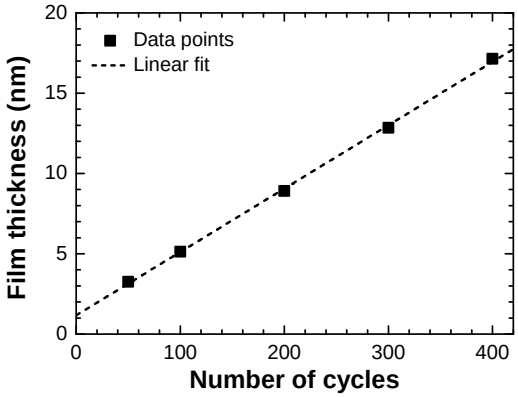

Figure 5.3: Film thickness vs. number of deposition cycles plot for GaN thin films deposited at 250 °C using $GaMe_3$ and NH_3 plasma.

5.1.1.2 Characterization of GaN Thin Films

Compositional characterization of ~17 nm thick GaN film was carried out by X-ray photoelectron spectroscopy (XPS). Survey scan detected peaks of Ga, N, O, and C at the film surface. Figure 5.4 represents the compositional depth profile of the film deposited at 250 °C. In the bulk film (t_{etch} = 60 s), concentrations of Ga, N and O were 36.6, 43.9 and 19.5 at.%, respectively. Compositional characterization of ~42 nm thick film deposited at 185 °C revealed similar results, where concentrations of Ga, N and O in the bulk film were determined as 31.3, 46.9 and 21.8 at.%, respectively. Although these results suggest that the films are N-rich, in practice it is not possible to determine the real Ga/N ratio using wide-scan survey spectra since Auger peaks of Ga overlap with the N 1s peak and contribute to its intensity. There is also a slight N 2s contribution in the Ga 3d peak. When the background of N 1s peak was determined manually, which in

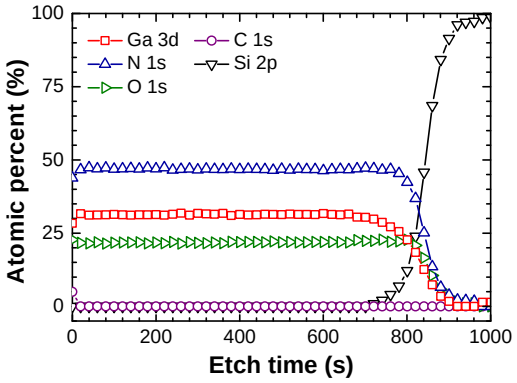

Figure 5.4: Compositional depth profile of ~17 nm thick GaN thin film deposited at 250 °C.

part eliminated the Ga contribution, the elemental composition of ~42 nm thick GaN film (t_{etch} = 100 s) was found as 41.84 at.% Ga, 29.81 at.% N, 26.41 at.% O, and 1.94 at.% Ar (Ar incorporation occurs as a result of ion etching process). However, it should be noted that this data still does not represent the actual atomic concentrations of Ga and N. In order to determine the actual values, the high-resolution XPS (HR-XPS) data should be analyzed. Atomic concentrations of Ga and N, and therefore the stoichiometry can be determined if Ga 3d and N 1s peaks are distinguished by the deconvolution of HR-XPS data and correlated with the correct Scofield factors. As the deposition temperature decreased from 250 to 185 °C, O content in the film increased from 19.5 to 21.8 at.%. This behavior is similar to that seen in the case of GPC, and may explain the higher deposition rates observed in region II (Figure 5.2(a)). For both of these films, C was detected only at the surfaces and no C impurities were found in the bulk films, indicating that the methyl groups (CH_3) were completely removed from $GaMe_3$ molecules by the use of NH_3 plasma.

Constant O concentrations throughout the film thicknesses reveal that the oxidation occurs during film deposition. In order to determine the source of O present in the films, trimethylaluminum ($AlMe_3$) precursor (carried by Ar) was pulsed into the reactor for 500 times at 250 °C. There was 10 s of purging time between the pulses. If there were any unwanted O contents in the reactor or in

the Ar gas, then Al_2O_3 would be expected to grow. However, no film growth was observed. Although we carried out a similar experiment at 185 °C using the $GaMe_3$ precursor, we later realized that $GaMe_3$ does not react with H_2O at this temperature; in order to deposit Ga_2O_3 thin films we used O_2 plasma as the reactant [203]. These results indicated that the source of O was neither a leak in the reactor nor the Ar gas. The most probable source of high O levels was therefore presumed as the O-containing impurities in 5N-grade NH_3 gas. This argument strengthened by the fact that there were no filters/gas purifiers installed on the gas delivery lines. However, as it will be shown in Section 5.3.1, similar O concentrations were detected in GaN films deposited with purified process gases. The true source of oxygen contamination was then found to be the quartz tube of ICP source itself, which was later confirmed by the case where we detected a leak in the system due to the etching of the quartz tube (see Figure 5.5). Such plasma-related oxygen contamination was also reported for GaN thin films grown by remote plasma enhanced chemical vapor deposition [204].

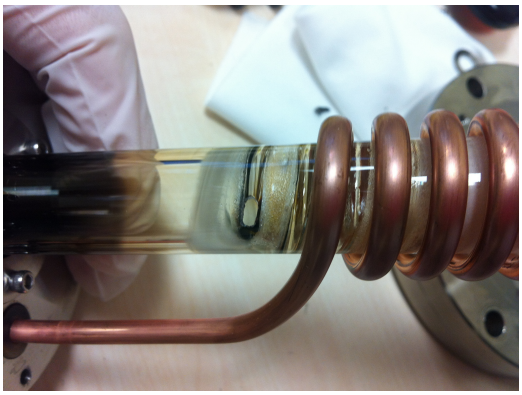

Figure 5.5: Photograph of the quartz tube of ICP source, which was etched all the way through its wall thickness.

High-resolution transmission electron microscopy (HR-TEM) images of ~42 nm thick GaN thin film deposited at 185 °C are given in Figures 5.6(a) and 5.6(b). Film thickness was measured as 40.8 nm from Figure 5.6(a), which is in good agreement with the results obtained by spectroscopic ellipsometry (SE). Film was found to be composed of small crystallites dispersed in an amorphous matrix (Figure 5.6(b)). A similar microstructure was also observed for the ~17 nm thick

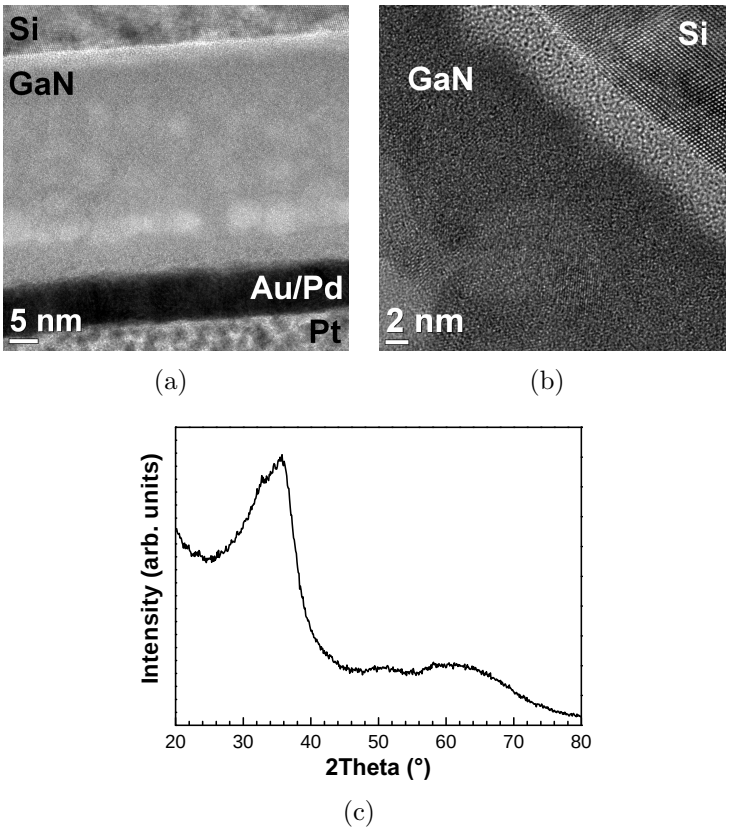

Figure 5.6: (a), (b) Cross-sectional HR-TEM images of ~42 nm thick GaN thin film deposited at 185 °C on Si (111) substrate. (c) GIXRD pattern of ~17 nm thick GaN thin film deposited at 250 °C on Si (100) substrate.

GaN thin film deposited at 250 °C. GIXRD pattern of this sample (Figure 5.6(c)) indicated an amorphous structure, with some implications of long-range order corresponding to the small crystallites that exist in the amorphous Ga-O-N matrix.

Surface morphology of the film was studied by atomic force microscopy (AFM). Root-mean-square (rms) roughness of the ~17 nm thick film deposited at 250 °C was measured as 0.58 nm from a 1 μm × 1 μm scan area. X-ray reflectivity (XRR) data of the ~42 nm thick film deposited at 185 °C was fitted using a 3-layer model (i.e., $Ga_xO_yN_z/SiO_2/Si$), from which the thickness, mass density and roughness values were estimated as 39.37 nm, 5.25 g/cm^3 and 1.26 nm, respectively. The thickness and refractive index of the film were determined using SE as 42.01 nm and 1.89 (λ = 632 nm), respectively.

5.1.2 PA-ALD Using $GaEt_3$ and NH_3 Plasma

5.1.2.1 Optimization of PA-ALD Parameters

GaN thin films were deposited on Si (111) substrates by PA-ALD using $GaEt_3$ and NH_3 as the Ga and N precursors, respectively. Figure 5.7(a) shows the $GaEt_3$ saturation curves obtained at 150 and 250 °C. The data obtained at 250 °C did not show a clear saturation behavior. Therefore, same depositions were repeated after the temperature was decreased to 150 °C. As seen in Figure 5.7(a), GPC increased with $GaEt_3$ pulse length until 1 s. A further increase in $GaEt_3$ pulse length did not affect GPC, implying that the chemisorption of $GaEt_3$ is self-limiting at this temperature. The effect of purge time on GPC at 150 °C is given in Figure 5.7(b). Data given in this plot were collected from thin film samples, which were deposited by repeating the following PA-ALD cycle for 200 times: 0.5 s $GaEt_3$/Ar purge/90 s, 50 sccm, 300 W NH_3 plasma/Ar purge. As shown in the figure, GPC decreased from 0.60 to 0.49 Å as the purge time increased from 0 to 5 s, and remained constant at this value for longer purge times. Ten seconds of purge time, which has already been used for the saturation curve depositions, was therefore shown to be sufficient for the separation of reactants. Figure 5.8(a) is the NH_3 saturation curve obtained at 250 °C. GPC increased with NH_3 flow duration until 120 s and reached saturation at ~0.47 Å.

GPC values for GaN thin films deposited at different temperatures are given in Figure 5.8(b). For these experiments, 200 cycles were deposited with 0.5 s $GaEt_3$/10 s Ar purge/90 s, 50 sccm, 300 W NH_3 plasma/10 s Ar purge. A constant GPC (i.e., ~0.48 Å) was observed within the temperature range of 150-350 °C. For higher temperatures, GPC increased with temperature. Film thickness vs. number of deposition cycles graph for GaN films deposited at 150 °C using 1 s $GaEt_3$ with 120 s NH_3 plasma is given in Figure 5.9. A linear growth behavior was observed at 150 °C, where slope of the linear fit revealed the GPC as 0.43 Å.

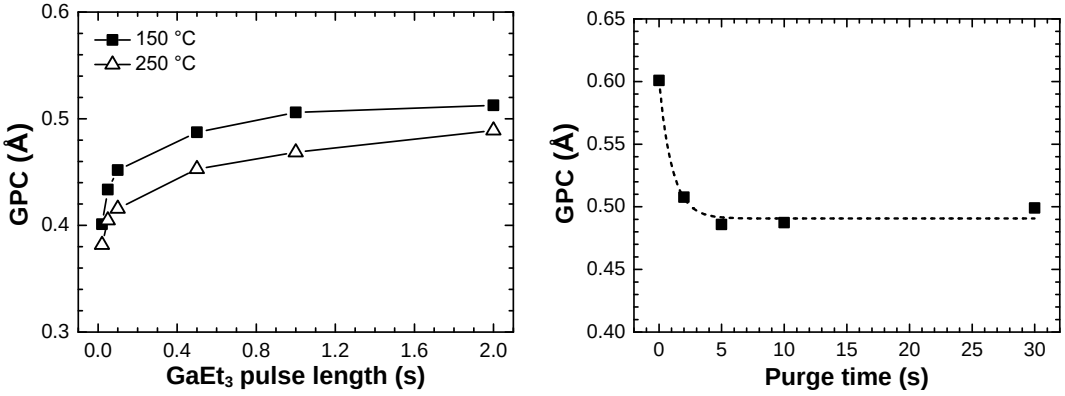

(a) (b)

Figure 5.7: (a) $GaEt_3$ saturation curves at 150 and 250 °C. NH_3 flow rate and duration were constant at 50 sccm and 90 s, respectively. Purge time between the exposures was 10 s. (b) Deposition rate as a function of purge time. Dashed line is for visual aid.

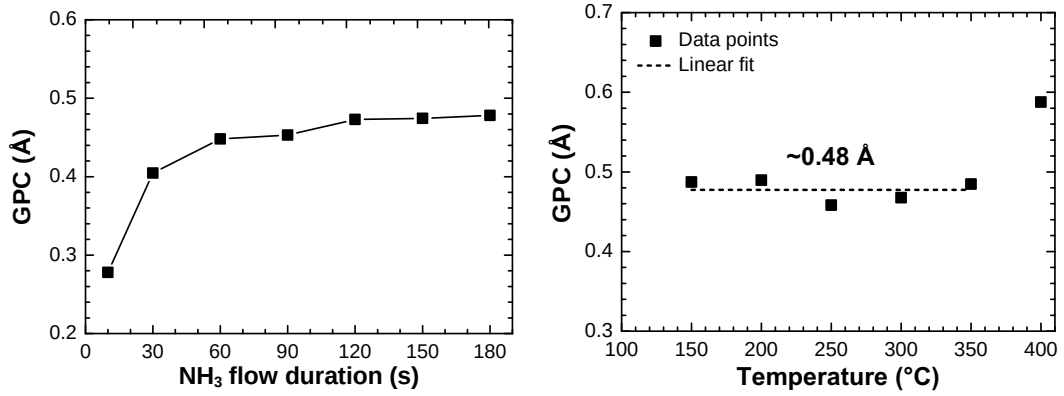

(a) (b)

Figure 5.8: (a) NH_3 saturation curve at 250 °C. $GaEt_3$ pulse length was constant at 0.5 s, purge time between the exposures was 10 s. (b) GPC values for GaN thin films deposited at different temperatures.

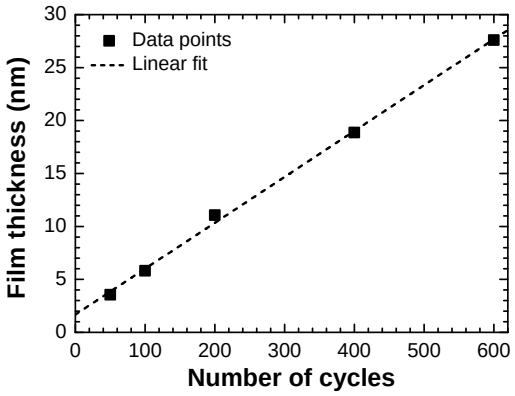

Figure 5.9: Film thickness vs. number of deposition cycles plot for GaN thin films deposited at 150 °C using $GaEt_3$ and NH_3 plasma.

5.1.2.2 Characterization of GaN Thin Films

Compositional characterization of ~28 nm thick GaN film deposited at 150 °C was carried out using XPS. Survey scans detected peaks of Ga, N, O, and C. C was detected only at the film surface and no C impurities were found in the bulk film. O content of the film was high; i.e., 22.5 at.%, as determined from compositional depth profile. XPS survey scan revealed the elemental composition of bulk film (t_{etch} = 100 s) as 38.49 at.% Ga, 35.91 at.% N, 23.83 at.% O, and 1.77 at.% Ar, where the background of N 1s peak was determined manually. GIXRD pattern of the sample, which indicated an amorphous structure, was identical to that of ~17 nm thick GaN thin film deposited at 250 °C using $GaMe_3$ and NH_3 plasma (see Figure 5.6(c)). XRR data of the film was fitted using a 3-layer model (i.e., $Ga_xO_yN_z/SiO_2/Si$), from which the thickness, mass density and roughness values were estimated as 26.66 nm, 4.76 g/cm^3 and 1.11 nm, respectively. The thickness and refractive index of the film were determined using SE as 27.67 nm and 1.90 (λ = 632 nm), respectively.

5.2 PA-ALD of InN Thin Films

5.2.1 PA-ALD Using $InMe_3$ and NH_3 Plasma

Four sequential depositions were carried out at 250 °C using $InMe_3$ and NH_3 plasma as the In and N precursors, respectively. Details of these depositions are summarized in Table 5.1. After each deposition, ellipsometric spectrum of the sample was recorded (Figure 5.10), and then the sample was loaded back into the reactor for the following deposition. Although the ellipsometric angle, Psi (Ψ) shifted slightly to higher values with each deposition, there was no significant film growth after 1000 PA-ALD cycles as determined by both SE and XRR. XPS survey scan indicated the presence of 1.47 at.% In, 21.44 at.% N, 46.88 at.% O, 24.71 at.% C at the film surface. The remaining 5.5 at.% was the contribution from Si (111) substrate.

Table 5.1: Details of the sequential $InMe_3$-NH_3 plasma depositions.

Deposition sequence	Number of cycles	$InMe_3$ pulse length (s)	NH_3[a] flow duration (s)	Purge time (s)
D1	250	0.015	180	5
D2	250	0.03	180	5
D3	250	0.015	60	5
D4	250	0.015	300	5

[a]Flow rate and plasma power were 50 sccm and 300 W, respectively.

5.2.2 PA-ALD Using CpIn and NH_3 Plasma

Two sequential depositions were carried out at 250 °C using CpIn and NH_3 plasma as the In and N precursors, respectively. 250 PA-ALD cycles were deposited in each case, where one PA-ALD cycle was consisted of 1 s CpIn/10 s Ar purge/40 s, 50 sccm, 300 W NH_3 plasma/10 s Ar purge. Therefore, a total of 500 cycles were deposited on a Si (111) substrate. XPS survey scan detected 9.99 at.% In,

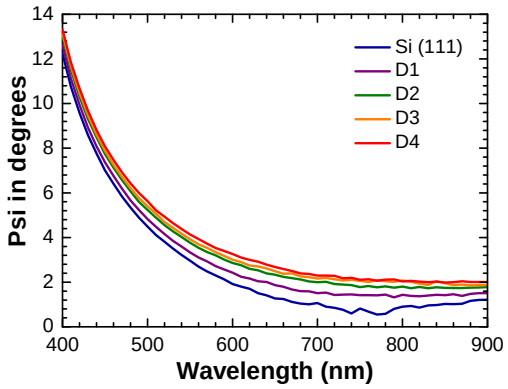

Figure 5.10: Ellipsometric spectra of the Si (111) substrate before and after the sequential $InMe_3$-NH_3 plasma depositions. The angle of incidence was 75°.

5.12 at.% N, 34.45 at.% O, 32.08 at.% C, and 18.35 at.% Si at the sample surface. GIXRD pattern of the sample indicated a polycrystalline structure consisting of cubic In_2O_3 (*c*-In_2O_3) and tetragonal In (*t*-In) phases. Upon annealing at 900 °C for 30 min under N_2 ambient, peaks corresponding to the *t*-In phase disappeared. The thickness of the annealed sample, which was polycrystalline single-phase *c*-In_2O_3, was determined using SE as 7.2 nm. When O_2 plasma was used as the reactant, 250 PA-ALD cycles (1 s CpIn/5 s Ar purge/20 s, 25 sccm, 300 W O_2 plasma/5 s Ar purge) were resulted in a ~36.2 nm thick *c*-In_2O_3 thin film [205].

5.3 GaN and AlN Thin Films Deposited Using Purified NH_3, N_2/H_2 and N_2 Plasma Gases

In Section 5.1, GaN thin films deposited using metalorganic precursors and NH_3 plasma were shown to have high O incorporation, which was attributed to oxygen contamination related to the plasma system. In this section, it will be shown that the choice of nitrogen containing plasma gas (NH_3, N_2/H_2 or N_2) determines the severity of O incorporation into deposited films. Lowest O concentrations were attained for GaN and AlN thin films using N_2 and NH_3 plasmas, respectively.

5.3.1 GaN Thin Films

Three samples were deposited at 185-215 °C using different N-containing plasma gases, namely NH_3, N_2 and N_2/H_2. Being different than the depositions described in Section 5.1, 5N-grade plasma gases, and the carrier gas, Ar, used in these depositions were further purified using MicroTorr gas purifiers.

For the film deposited with NH_3 plasma, one PA-ALD cycle consisted of 0.015 s $GaMe_3$ (T_{GaMe_3} = 6 °C)/10 s Ar purge/90 s, 50 sccm, 300 W NH_3 plasma/10 s Ar purge. For this sample, 21.5 at.% O was detected in the bulk film using XPS. In other words, the high O concentration in GaN film could not be lowered by the use of purified process gases. It has been then realized that the actual source of this oxygen contamination was the etching of quartz tube in which plasma forms. As an attempt to grow GaN thin films with low O concentrations, we tried thermal ALD of GaN at 450 °C, however $GaMe_3$ and NH_3 did not react at this temperature, and therefore no film growth was observed. For the following PA-ALD experiments, shorter plasma durations were used in order to avoid heating of the quartz tube and a lower base pressure was employed (i.e., ~150 mTorr) for favoring the inductive plasma source operation, both of which would minimize the sputtering of quartz and therefore decrease the extent of plasma-related oxygen contamination [206]. Table 5.2 summarizes the deposition conditions for GaN thin film samples. Elemental compositions of the deposited films are given in Table 5.3.

Table 5.2: Deposition details for GaN thin film samples.

Plasma gas	Flow rate (sccm)	Flow duration (s)	Deposition temperature (°C)	Number of cycles	Film thickness[a] (nm)
NH_3	50	90	185	1000	31.6
N_2	50	20	215	1000	19.1
N_2/H_2	50/20	20/5	200	1000	22.0

[a]Film thicknesses were measured using SE.

Table 5.3: Elemental compositions of GaN thin film samples as determined by XPS survey scans. Data were collected after 60 s Ar ion etching.

Plasma gas	Elemental composition (at.%)				
	Ga	N	O	C	Ar
NH_3	45.02	31.69	21.46	-	1.84
N_2	44.58	41.83	4.48	9.12	-
N_2/H_2	46.46	44.64	4.70	4.20	-

When N_2 plasma was used instead of NH_3 plasma, O concentration of GaN thin film decreased to 4.48 at.%, whereas its C concentration increased to 9.12 at.%. The sample deposited using N_2 plasma was amorphous. We were able to deposit polycrystalline wurtzite GaN thin films with low O and C concentrations (4.70 and 4.20 at.%, respectively) at 200 °C by introducing 20 sccm H_2 in addition to 50 sccm N_2 during the third quarter of the plasma duration. GIXRD pattern of the GaN film deposited using N_2/H_2 plasma is shown in Figure 5.11. These results show that C impurities have a detrimental effect on the crystallinity of GaN and introduction of H_2 during the N_2 plasma is crucial for achieving C-free GaN thin films.

XRR data of the sample with high O concentration (NH_3 plasma, 21.46 at.% O) was fitted using a three-layer model (i.e., $Ga_xO_yN_z/SiO_2/Si$), whereas those of the samples with relatively low O concentrations were fitted using a four-layer model (i.e., $Ga_2O_3/GaN/SiO_2/Si$). Film thickness values obtained by fitting of the measured XRR data were slightly lower than those measured by SE. Film thicknesses ($t_{Ga_xO_yN_z}$ or $t_{GaN} + t_{Ga_2O_3}$) were measured as 30.48, 18.27 and 22.63 nm for the films deposited using NH_3, N_2 and N_2/H_2 plasmas, respectively. Furthermore, density values of 4.64, 4.09 and 4.91 g/cm^3, and roughness values of 0.49, 1.16 and 2.61 nm were estimated for GaN films deposited using NH_3, N_2 and N_2/H_2 plasmas, respectively.

Refractive index of the GaN film at 632 nm was increased from 1.93 to 2.00 as the O concentration decreased from 21.46 to 4.48-4.70 at.%. The increase in C concentration did not affect the refractive index value.

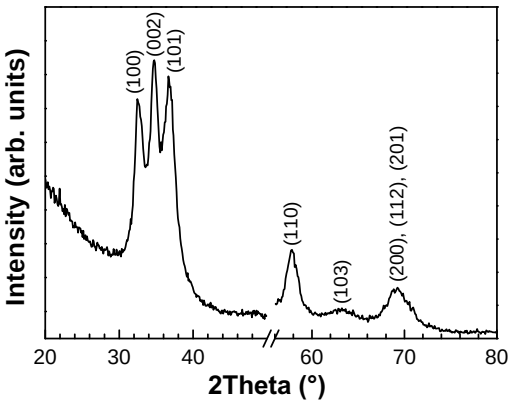

Figure 5.11: GIXRD pattern of a ~22 nm thick GaN thin film deposited at 200 °C by PA-ALD using $GaMe_3$ and N_2/H_2 plasma.

5.3.2 AlN Thin Films

Six samples were deposited at 190 °C using different N-containing plasma gases, namely NH_3, N_2 and N_2/H_2. 5N-grade plasma gases, and the carrier gas, Ar, used in these depositions were further purified using MicroTorr gas purifiers. One PA-ALD cycle was consisted of 0.1 s $AlMe_3$/10 s Ar purge/N-containing plasma (plasma power = 300 W)/10 s Ar purge. An AlN thin film was also deposited at 450 °C using thermal ALD, and used for comparison. Deposition details for AlN thin film samples are summarized in Table 5.4. Elemental compositions of the deposited AlN films are given in Table 5.5.

In the case of GaN thin films (Section 5.3.1), the film deposited using NH_3 plasma had ~20 at.% O in the bulk film. The use of N_2 or N_2/H_2 plasma decreased this value to <5 at.%. When same approach was followed for the deposition of AlN using $AlMe_3$, O concentration of the film increased tremendously (i.e., >45 at.%). AlN samples deposited using N_2/H_2 plasma process, in which N_2 and H_2 were simultaneously introduced into the reactor, had 4-5 at.% O and 5-6 at.% C in the bulk film. For AlN, best results were obtained with the $AlMe_3$-NH_3 plasma process. For this sample, 3.88 at.% C was found in the bulk film. In Section 4.2.2.1, we reported on the deposition of C-free AlN thin films with low O concentrations using the same PA-ALD process. This suggests that NH_3 plasma

Table 5.4: Deposition details for AlN thin film samples.

Plasma gas	Flow rate (sccm)	Flow duration (s)	Number of cycles	Film thickness[a] (nm)
NH_3	50	20	500	33.5
N_2	50	20	500	53.1
N_2/H_2-1	50/20	20/5[b]	500	42.9
N_2/H_2-2	50/20	20/5[c]	500	53.8
N_2/H_2-3	50/20	20	500	20.4
N_2/H_2-4	50/50	20	500	17.1
NH_3-thermal	50	20	500	51.9

[a]Film thicknesses were measured using SE.
[b]H_2 at 3rd quarter.
[c]H_2 at 1st quarter

duration (20 vs. 40 s) has a major effect on the resulting C concentration of AlN thin films. Furthermore, the atomic concentrations of O and C in the AlN thin film deposited using $AlMe_3$-NH_3 plasma process were comparable to those in AlN film deposited using thermal ALD. Since plasma was not activated during the thermal ALD of AlN, O impurity concentration detected in this film is not associated with the plasma-related oxygen contamination; therefore it represents the minimum attainable O concentration at the given deposition conditions. When compared to sample deposited using thermal ALD, a lower O concentration was detected for the film deposited using NH_3 plasma. This difference is considered to be within the limits of measurement error. XPS results therefore suggest that the AlN films deposited using NH_3 plasma are not affected by the plasma-related oxygen contamination. For the film deposited using N_2/H_2 plasma (N_2/H_2-4), 4.04 at.% O was detected after 50 s of Ar ion etching, which is higher than the value reported in Section 4.3.2 for films deposited with 40 s N_2/H_2 plasma (i.e., 1.77 at.% O). However, it should be noted that - as discussed in the previous chapter - AlN films deposited using PA-ALD are prone to atmospheric surface oxidation, effects of which expected to be significant even after Ar ion etching in the case of very thin films.

Table 5.5: Elemental compositions of AlN thin film samples as determined by XPS survey scans.

Plasma gas (-sample number)	t_{etch} (s)	Elemental composition (at.%)				
		Al	N	O	C	Ar
NH_3	150	51.53	41.18	1.51	3.88	1.90
N_2	150	34.78	7.71	48.45	8.00	1.07
N_2/H_2-1	150	38.99	7.03	45.71	6.44	1.83
N_2/H_2-2	150	36.26	7.23	47.42	7.72	1.38
N_2/H_2-3	50	49.13	38.26	4.73	5.94	1.93
N_2/H_2-4	50	49.83	39.17	4.04	4.95	2.02
NH_3-thermal	150	52.88	39.33	1.78	4.08	1.93

Samples with high O concentrations were amorphous as determined by GIXRD. Samples N_2/H_2-3 and N_2/H_2-4 were also amorphous due to the O (~4-5 at.%) and C (~5-6 at.%) impurities. The sample deposited using NH_3 plasma had low concentration of O impurities, however 3.88 at.% C was detected in the sample. Its GIXRD pattern revealed a weak crystallinity with broad peaks corresponding to the hexagonal wurtzite crystal structure.

XRR data were fitted using a three-layer model (i.e., $Al_xO_yN_z/SiO_2/Si$) for the films having >45 at.% O. For the AlN films with low O concentrations, on the other hand, a four-layer model (i.e., $Al_2O_3/AlN/SiO_2/Si$) was applied. XRR results (film thickness, mass density and roughness) are given in Table 5.6 together with the refractive index values, which were determined using SE. Film thicknesses estimated using XRR were in good agreement with the values obtained from SE. Mass density values within the range of 2.35-2.53 g/cm^3 were determined for AlN films deposited using NH_3, N_2 and N_2/H_2 plasmas. These values are lower than 2.71 and 2.61 g/cm^3, which were reported in the previous chapter for films deposited using 40 s NH_3 and N_2/H_2 plasma durations, respectively. Refractive indices of AlN films deposited using PA-ALD increased from 1.55 to 1.84 as the O impurity concentrations decreased from >45 to 1.51 at.%. Yet, the highest refractive index value was still lower than that reported for AlN films deposited using 40 s NH_3 and N_2/H_2 plasma durations ($n = 1.92$ at 632 nm). Mass density and refractive index of the AlN film deposited using thermal ALD ($\rho = 2.72$

g/cm^3, $n = 1.95$ at 632 nm) were slightly higher than those of AlN film deposited using NH_3 plasma with 40 s plasma duration.

Table 5.6: Thickness, mass density and roughness values for AlN thin film samples as estimated by XRR. Refractive index values, which were determined using SE, are also included.

Plasma gas	t_{AlN} or $t_{Al_xO_yN_z}$ (nm)	$t_{Al_2O_3}$ (nm)	ρ (g/cm^3)	r (nm)	n^a
NH_3	31.69	0.35	2.49	1.01	1.84
N_2	50.98	-	2.48	0.28	1.56
N_2/H_2-1	41.52	-	2.53	0.71	1.55
N_2/H_2-2	51.64	-	2.51	0.51	1.56
N_2/H_2-3	17.44	2.05	2.35	0.59	1.82
N_2/H_2-4	15.94	1.36	2.42	0.85	1.83
NH_3-thermal	48.93	0.37	2.72	1.81	1.95

[a] n is the refractive index at 632 nm.

Chapter 6

Hollow Cathode Plasma-Assisted Atomic Layer Deposition of III-Nitride Thin Films

The work described in this chapter was published in part as: C. Ozgit-Akgun, E. Goldenberg, A. K. Okyay, and N. Biyikli, "Hollow cathode plasma-assisted atomic layer deposition of crystalline AlN, GaN and $Al_xGa_{1-x}N$ thin films at low temperatures," *Journal of Materials Chemistry C*, 2014. DOI: 10.1039/c3tc32418d

Hollow cathode plasma-assisted atomic layer deposition (HCPA-ALD) of crystalline aluminum nitride (AlN), gallium nitride (GaN), aluminum gallium nitride ($Al_xGa_{1-x}N$), and indium nitride (InN) thin films was demonstrated at 200 °C using trimethylaluminum ($AlMe_3$), trimethylgallium ($GaMe_3$) and cyclopentadienyl indium (CpIn) as the Al, Ga and In precursors, respectively. Deposition parameters including metalorganic pulse length, N_2/H_2 plasma flow duration and purge time were optimized for $AlMe_3$-N_2/H_2 and $GaMe_3$-N_2/H_2 plasma processes. Films deposited using both non-optimized and optimized parameters were characterized in detail using elemental, structural, surface, and optical analyses.

6.1 AlN and GaN Thin Films Deposited Using Non-Optimized HCPA-ALD Parameters

AlN and GaN thin films were first deposited on 4 in. Si (100) substrates at 200 °C using non-optimized process parameters. Eight hundred cycles were deposited, where one cycle consisted of 0.1 s $AlMe_3$ or 0.015 s $GaMe_3$/10 s Ar purge/40 s, 300 W NH_3 plasma (50 sccm) or N_2/H_2 plasma (50 sccm each)/10 s Ar purge. Table 6.1 summarizes the spectroscopic ellipsometry (SE) results obtained from AlN and GaN thin film samples deposited using NH_3 and N_2/H_2 plasma processes, where average thickness (t_{avg}), average refractive index (n_{avg}) and uniformity data were obtained by the evaluation of spectra taken from five different points on the Si 4 in. wafer (the center and the edges). Growth per cycle (GPC) was calculated by dividing t_{avg} by the number of cycles applied, assuming that a constant amount of material was deposited in each cycle. When compared to N_2/H_2 plasma, the use of NH_3 plasma resulted in slightly higher GPC values for both AlN and GaN thin films. On the other hand, films deposited using N_2/H_2 plasma were better in terms of thickness uniformity. Although these deposition experiments were carried out using HCPA-ALD parameters that are not optimized for true ALD conditions, resulting films were reasonably uniform with wafer-level uniformity of $\leq \pm 1.5\%$ (see Figure 6.1). It is also worth mentioning that we achieved higher GPC

Table 6.1: SE results of AlN and GaN thin films deposited using non-optimized HCPA-ALD parameters.

Sample	t_{avg} (nm)	Uniformity[a] of t (±%)	GPC (Å)	n_{avg}[b]	Uniformity[c] of n (±%)
AlN (NH_3 plasma)	81.5	1.23	1.02	1.98	0.04
AlN (N_2/H_2 plasma)	76.7	1.05	0.96	1.99	0.15
GaN (NH_3 plasma)	21.1	1.51	0.26	2.17	0.50
GaN (N_2/H_2 plasma)	18.4	1.31	0.23	2.14	0.17

[a]Uniformity (±%) is calculated using the formula: $[(t_{max}\text{-}t_{min})/(2\times t_{avg})]\times 100$.
[b]n_{avg} is the average refractive index at 632 nm.
[c]Uniformity (±%) is calculated using the formula: $[(n_{max}\text{-}n_{min})/(2\times n_{avg})]\times 100$.

values for AlN (1.02 and 0.96 Å for NH_3 and N_2/H_2 plasma processes, respectively) using the present configuration; GPC values that we obtained using the previous configuration with quartz-based inductively coupled RF-plasma (ICP) source (see Sections 4.2.1 and 4.3.1) were 0.86 and 0.55 Å for NH_3 and N_2/H_2 plasma processes, respectively. Although this improvement may be related to the higher plasma density of the hollow cathode plasma (HCP) source, this cannot be stated for sure since the base pressure and Ar carrier flow rates were not same for

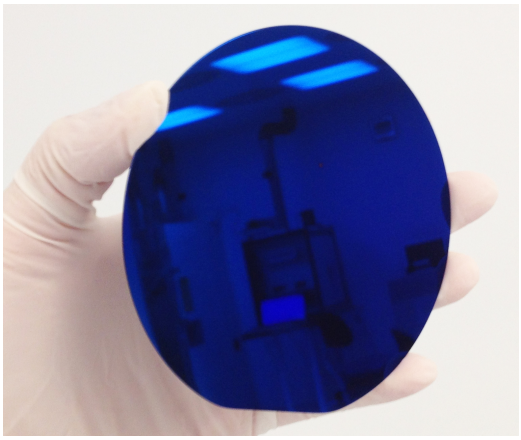

Figure 6.1: Photograph of a 81.5 nm thick AlN thin film deposited on 4 in. Si (100) substrate using $AlMe_3$ and NH_3 plasma. Wafer-level uniformity was measured as ±1.23%.

the current and previous configurations. Refractive indices of the AlN thin films deposited using NH_3 and N_2/H_2 plasmas were 1.98 and 1.99 at 632 nm, respectively, which are higher than the values measured for AlN thin films deposited using quartz-based ICP source and in good agreement with the values given in literature for polycrystalline AlN thin films [189]. We measured the refractive indices of GaN films deposited using NH_3 and N_2/H_2 plasmas as 2.17 and 2.14, respectively, which are comparable to values given in literature [207].

X-ray photoelectron spectroscopy (XPS) survey scans detected 6-11 at.% C and 15-30 at.% O on the AlN and GaN film surfaces. AlN surfaces were more prone to atmospheric oxidation (25-30 at.% O) as compared to GaN surfaces (15-16 at.% O). Additional XPS survey scans were obtained with constant time intervals (e.g., 60 s) as the samples in the ultra high vacuum (UHV) chamber of XPS system were etched with a beam of Ar ions. For all the four samples, C 1s peak disappeared with the first etch; therefore no C was detected in the subsequent scans. O concentrations in the AlN thin films gradually decreased with each etch, and became constant for t_{etch} ≥300 s. XPS survey scan obtained after 600 s of etch revealed the elemental composition of AlN thin film deposited using NH_3 plasma as 50.45 at.% Al, 45.56 at.% N, 2.45 at.% O. The remaining 1.54 at.% corresponds to Ar, which incorporates into samples during ion etching. Elemental composition of the AlN deposited using N_2/H_2 plasma was very similar to that deposited using NH_3 plasma. Survey scan (t_{etch} = 600 s) indicated 50.77 at.% Al, 44.90 at.% N, 2.97 at.% O, and 1.37 at.% Ar for this sample. These results indicate that the AlN films are slightly Al-rich with Al/N ratios of 1.11 and 1.13 for samples deposited using NH_3 and N_2/H_2 plasma processes, respectively. Elemental compositions of the GaN thin films were also determined using XPS (t_{etch} = 60 s), where 42.19 at.% Ga, 55.18 at.% N, 1.51 at.% O, 1.13 at.% Ar, and 42.24 at.% Ga, 54.57 at.% N, 1.65 at.% O, 1.54 at.% Ar were detected for the samples deposited using NH_3 and N_2/H_2 plasmas, respectively. Although these results suggest N-rich GaN films, it should be noted that the atomic concentration of N is overestimated due to the significant contribution of Auger Ga peaks, which overlap with the N 1s peak.

In terms of O impurity concentrations determined by XPS, it seems that the use of HCP source did not result in any improvement as we already reported ~3 at.% O for AlN films deposited using ICP source (see Sections 4.2.2 and 4.3.2). However it should be noted that the determination of impurity concentrations by XPS can be challenging. Butcher et al. [208] reported that using XPS to examine AlN thin films after etching the surface with a 5 kV argon ion beam results in substantial errors in the quantification of O and C impurities present in this material. In another study [209], it was reported that XPS can detect 2-5 at.% O again after Ar ion etching for commercial GaN samples which have approximately 0.02% bulk O as confirmed by secondary ion mass spectroscopy (SIMS). In order to further investigate this, we obtained SIMS depth profiles for AlN and GaN thin films deposited using NH_3 plasma (Figure 6.2). SIMS data showed that H, C and O impurities present in both films. Concentrations of O and C were 6.9×10^{20} and 2.5×10^{20} atoms/cc in the bulk AlN film (depth = 30 nm) (Figure 6.2(a)), both of which correspond to <1 at.%. In literature, similar quantities of O and C impurities were reported for AlN thin films deposited using PA-ALD [116]. SIMS depth profile of GaN film is given in Figure 6.2(b), where lower plateau (7-10 nm) reveals the real concentration of O in the GaN layer. The higher concentration in the 0-5 nm region is an artifact from ion mixing from the surface O. Concentrations of O and C impurities were determined as 1.4×10^{20}

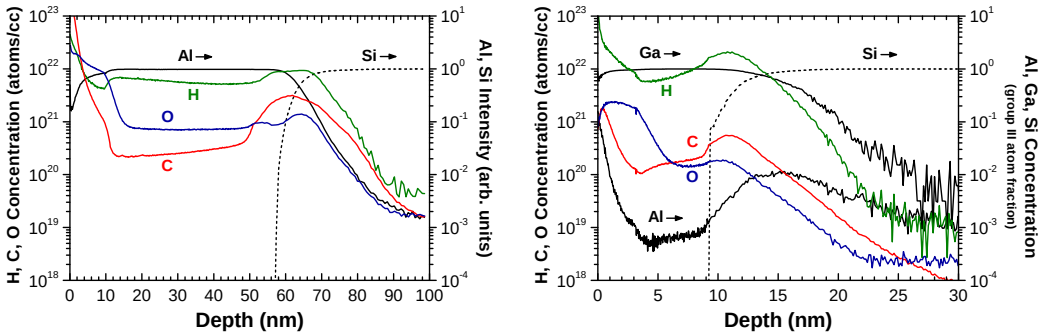

(a) (b)

Figure 6.2: Impurity concentrations determined by SIMS depth profiling for (a) AlN, and (b) GaN thin films deposited using NH_3 plasma. Silicon is not quantified in the layers, only plotted as the substrate layer marker.

and 1.8×10^{20} atoms/cc in the bulk GaN film (depth = 7 nm), both corresponding to <1 at.%. Concentrations of the H impurities were high in both films with values of 5.6×10^{21} and 8.0×10^{21} atoms/cc for AlN and GaN, respectively. This observation is in parallel with the results recently published by Perros et al. [113], which emphasize the presence of high concentrations (~20 at.%) of H impurities in AlN thin films deposited by PA-ALD using NH_3 and N_2/H_2 plasmas. Film thicknesses estimated by SIMS were lower than those measured using SE, which is probably due to the different etch rates of AlN and GaN thin films deposited using HCPA-ALD and the standard samples used to quantify impurity concentrations.

Grazing-incidence X-ray diffraction (GIXRD) patterns of AlN and GaN thin films deposited using NH_3 plasma are given in Figure 6.3. Same GIXRD patterns were obtained for the AlN and GaN thin films deposited using N_2/H_2 plasma; the use of different plasma gases (NH_3 vs. N_2/H_2) affected neither the peak positions nor the relative intensities of peaks. As revealed by their GIXRD patterns, AlN and GaN films were polycrystalline with (hexagonal) wurtzite crystal structure. Crystallite size values were calculated from the (002) reflections using line profile analysis (LPA). Since the size-strain broadening was quite anisotropic, we were not able to determine an average value using the Williamson-Hall plot. Crys-

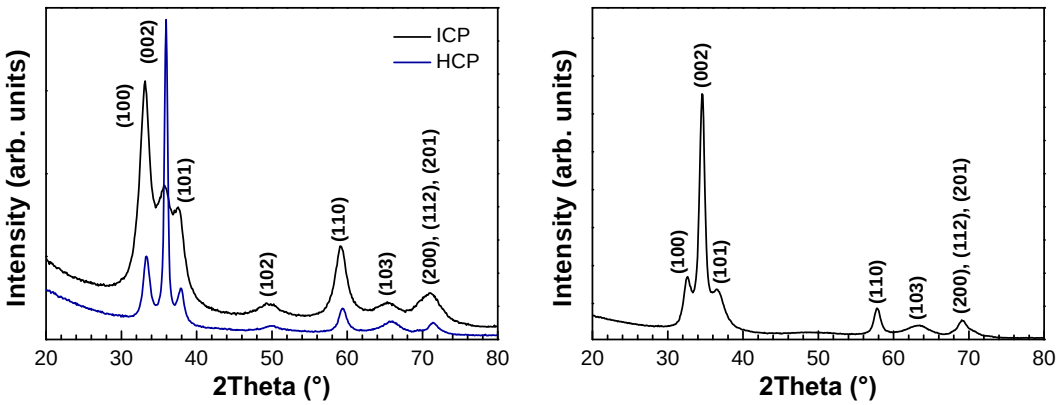

Figure 6.3: GIXRD patterns of (a) AlN, and (b) GaN thin films deposited on Si (100) substrates using NH_3 plasma. GIXRD pattern of the AlN thin film deposited using quartz-based ICP source is also shown in (a) for comparison.

tallite sizes were found to be 19.2 and 24.8 nm for AlN, and 10.2 and 9.3 nm for GaN films deposited using NH_3 and N_2/H_2 plasma processes, respectively. The GIXRD pattern of the AlN thin film deposited using the quartz-based ICP source is also included in Figure 6.3(a) for comparison. The increase in the intensity of (002) reflection and improvement in the full width at half maximum (FWHM) values suggest larger crystallites and therefore an enhancement in the crystalline quality for films deposited using current configuration with the HCP source. LPA analysis results obtained for the (002) reflections showed that the crystallite sizes, which were 3.4 and 3.1 nm for AlN films deposited using NH_3 and N_2/H_2 plasmas, respectively, increased to 20-25 nm with the use of present configuration. Assuming that a significant fraction of O impurities segregate at the grain boundaries, the increase in crystallite size might be indicating a decrease in the O impurity concentration. Figures 6.4(a) and 6.4(b) are the transmission electron microscopy (TEM) and high-resolution TEM (HR-TEM) images of the GaN thin film deposited using NH_3 plasma. The ~3 nm thick amorphous SiO_2 layer at the GaN/Si interface, which is generally named as the damage layer, formed during the TEM sample preparation using FIB [210]. Thickness of the GaN layer was measured from the HR-TEM image (Figure 6.4(b)) as 19.2 nm, which is ~2 nm lower than the value measured using SE (i.e., 21.1 nm). X-ray reflectivity (XRR), on the other hand, yielded a thickness of 18.2 nm for this sample (sum of the GaN and Ga_2O_3 layer thicknesses in the 4-layer XRR model), which is slightly lower than the value directly measured from HR-TEM image. Besides confirming polycrystallinity of the GaN layer, HR-TEM image also evidences the existence of large crystals in the film, which can extend along the film thickness. Diffraction rings seen in the SAED pattern (Figure 6.4(c)) also reveal the polycrystalline nature of GaN thin film, whereas reciprocal lattice points in this pattern correspond to the diamond lattice of the underlying Si (100) substrate.

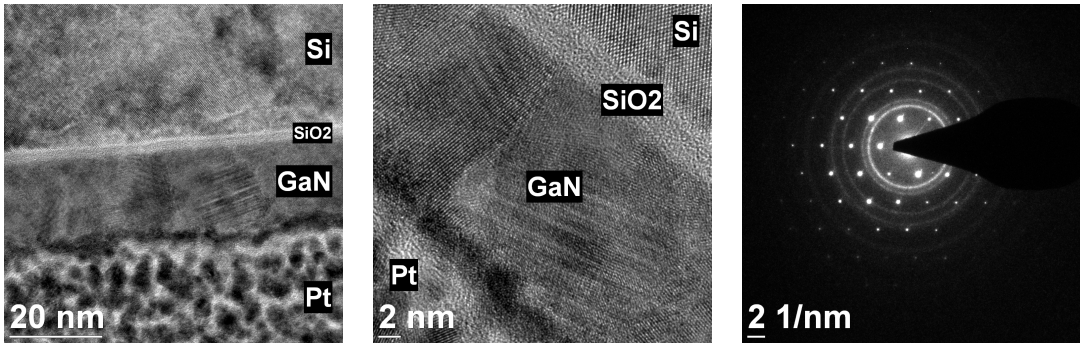

(a) (b) (c)

Figure 6.4: Cross-sectional (a) TEM, and (b) HR-TEM images of 21 nm thick GaN thin film deposited on Si (100) substrate using NH_3 plasma. FIB-induced SiO_2 damage layer formed at the GaN/Si interface during TEM sample preparation. (c) SAED pattern of the same sample.

6.2 Optimization of HCPA-ALD Parameters

6.2.1 AlN Thin Films

HCPA-ALD parameters were optimized at 200 °C for the deposition of AlN thin films using $AlMe_3$ and N_2/H_2 plasma. For the $AlMe_3$ saturation curve (Figure 6.5(a)) 200 cycles AlN were deposited on Si (100) substrates using different $AlMe_3$ pulse lengths, where one HCPA-ALD cycle was 0.03-0.12 s $AlMe_3$/10 s Ar purge/40 s, 50 + 50 sccm, 300 W N_2/H_2 plasma/10 s Ar purge. As seen in Figure 6.5(a), GPC values calculated using SE and XRR data followed the same trend with different values, and GPC slightly decreased with increasing $AlMe_3$ pulse lengths. Physically, such a decrease is not possible since as the pulse length increases the amount (or number) of $AlMe_3$ molecules that are being carried to reactor increases, which in turn increases the number of collisions the reactant has with the surface. Precursors may desorb from the surface when long purge times are used, however this should not be the case here since a constant purge time of 10 s was used for all depositions. Therefore the slight decrease in GPC was considered to be within the limits of measurement error, and ignored, and GPC was accepted as constant at ~0.93 Å (as measured by SE) for the $AlMe_3$

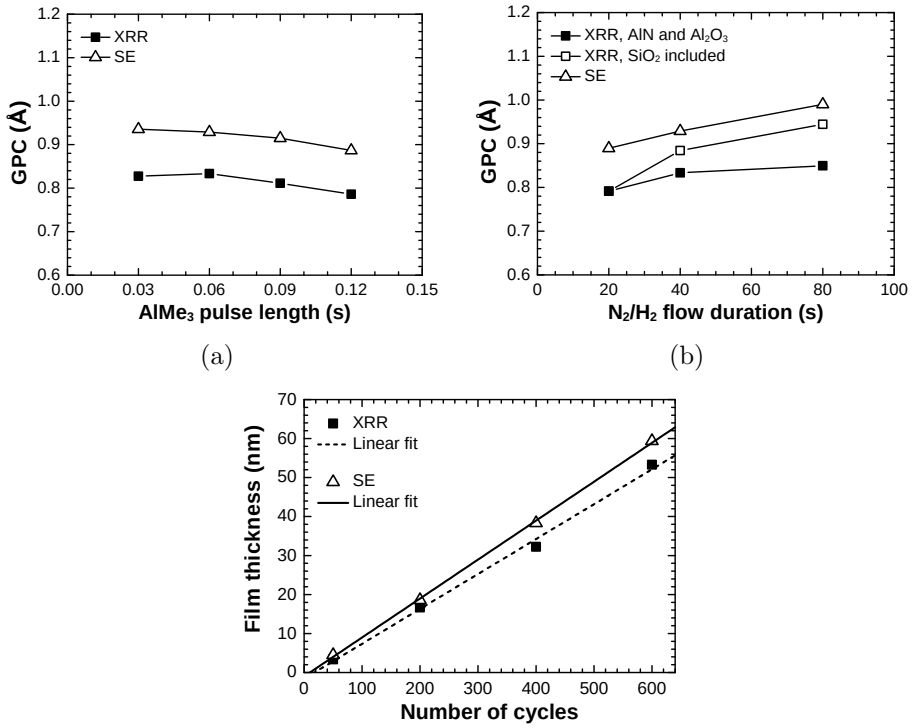

Figure 6.5: (a) $AlMe_3$, and (b) N_2/H_2 saturation curves at 200 °C. For the $AlMe_3$ saturation curve, N_2/H_2 flow rate and flow duration were kept constant at 50 + 50 sccm and 40 s, respectively. $AlMe_3$ pulse length was 0.06 s for the N_2/H_2 saturation curve. (c) AlN film thickness plotted as a function of number of deposition cycles.

pulse length range of 0.03-0.12 s. Although 0.03 s $AlMe_3$ seems to be enough for having self-limiting surface reactions, we selected 0.06 s as the optimized value for the following depositions. As the next step of optimization study, flow duration of N_2/H_2 plasma was varied while keeping the other parameters constant (Figure 6.5(b)). The data obtained using SE and XRR revealed different trends. According to curve plotted using XRR data, GPC first slightly increases and then reaches saturation for flow durations ≥40 s. According to the SE data, it increases from 0.89 to 0.99 Å with longer durations of N_2/H_2 flow within the 20-80 s range. It should be noted that since Si substrates were treated with HF prior to each deposition, the ellipsometric spectra were fitted using a two-layer model (i.e., Cauchy/Si (0.5 mm)) by assuming that the thickness of SiO_2 layer

at the AlN/Si interface was negligible. XRR data, on the other hand, were fitted using a four-layer model (i.e., Al_2O_3/AlN/SiO_2/Si); thicknesses of AlN and surface oxide (Al_2O_3) layers were added together for revealing the film thickness, which was then used for the calculation of GPC value. When the thicknesses of native SiO_2 layers were also included to the film thickness values (shown in Figure 6.5(b)), the results resembled those obtained by SE, where no saturation behavior was observed. Although the applicability of Cauchy dispersion function for the determination of AlN film thickness was verified by TEM (see Section 4.2.2), results suggest that the increase in GPC values obtained by SE for N_2/H_2 flow durations ≥40 s is due to the contribution of native oxide layer. Therefore, it can be presumed that the self-limiting surface reactions are achieved for AlN deposition when 40 s or longer N_2/H_2 plasma is used with predetermined N_2 and H_2 flow rates. Another parameter, which needs to be optimized, is the purge time. If the purge time is not long enough, then the precursor might be introduced into the chamber before the other one is completely purged away. This would result in gas-phase reactions and a significant chemical vapor deposition (CVD) component in the deposited films. In order to optimize this parameter for the deposition of AlN thin films, we did additional depositions using 5 and 20 s purge time, where $AlMe_3$ pulse length was 0.06 s and N_2/H_2 flow duration was 40 s. The GPC values, which were calculated using SE results, were found to be 0.90, 0.93 and 0.92 Å for 5, 10 and 20 s of purging, respectively. This confirms that 10 s purging is long enough to avoid any gas-phase reactions, and even 5 s can be used to have shorter cycles. The optimized recipe was therefore determined for the AlN growth as 0.06 s $AlMe_3$/10 s Ar purge/40 s, 50 + 50 sccm, 300 W N_2/H_2 plasma/10 s Ar purge. In Figure 6.5(c), AlN film thicknesses measured using SE and XRR were plotted as a function of the number of cycles. Results indicated linear growth with a slight nucleation delay. Slope of the linear fit of SE data revealed the GPC at 200 °C as ~1.0 Å.

6.2.2 GaN Thin Films

HCPA-ALD parameters were optimized at 200 °C for the deposition of GaN thin films using $GaMe_3$ and N_2/H_2 plasma, where 300 cycles were deposited using 0.015-0.09 s $GaMe_3$/5-20 s Ar purge/20-80 s, 50 + 50 s, 300 W N_2/H_2 plasma/5-20 s Ar purge. Figure 6.6(a) shows the $GaMe_3$ saturation curve, which was obtained by varying the $GaMe_3$ pulse length between 0.015 and 0.09 s, while keeping the purge time and N_2/H_2 plasma flow duration constant at 10 and 40 s, respectively. SE and XRR data revealed curves with similar shapes but slightly different values. When $GaMe_3$ pulse length was increased from 0.015 to 0.03 s, GPC (determined by SE) negligibly increased from 0.30 to 0.31 Å; for 0.06 and 0.09 s it was 0.32 Å. Therefore, GPC was constant within the range of 0.015-0.09 s, which evidences the self-limiting growth of GaN. In the following step, N_2/H_2 plasma duration was varied between 20 and 80 s (Figure 6.6(b)). $GaMe_3$ pulse length and purge time were 0.03 and 10 s, respectively. According to both SE and XRR data, GPC increased upon increasing the N_2/H_2 flow duration from 20 to 40 s, but then saturated and did not change when flow duration was further increased to 80 s, which again clearly indicates the existence of self-limiting growth mechanism. Therefore, optimized values of $GaMe_3$ pulse length and N_2/H_2 flow duration were determined as 0.03 and 40 s, respectively. The effect of purge time was studied by performing depositions with 5, 10 and 20 s of purge time, all of which resulted with the same GPC. Therefore the optimized recipe for GaN deposition was determined as 0.03 s $GaMe_3$/10 s Ar purge/40 s, 50 + 50 sccm, 300 W N_2/H_2 plasma/10 s Ar purge. Figure 6.6(c) shows GPC values for the optimized recipe, which were plotted as a function of the number of cycles. Both SE and XRR data show a similar trend, where GPC decreases with increasing number of deposition cycles. This suggests substrate-enhanced growth, where GPC of GaN on Si is higher when compared to that of GaN on itself. This kind of a growth behavior can occur if the number of reactive sites on the substrate is higher than on the ALD-grown material [12].

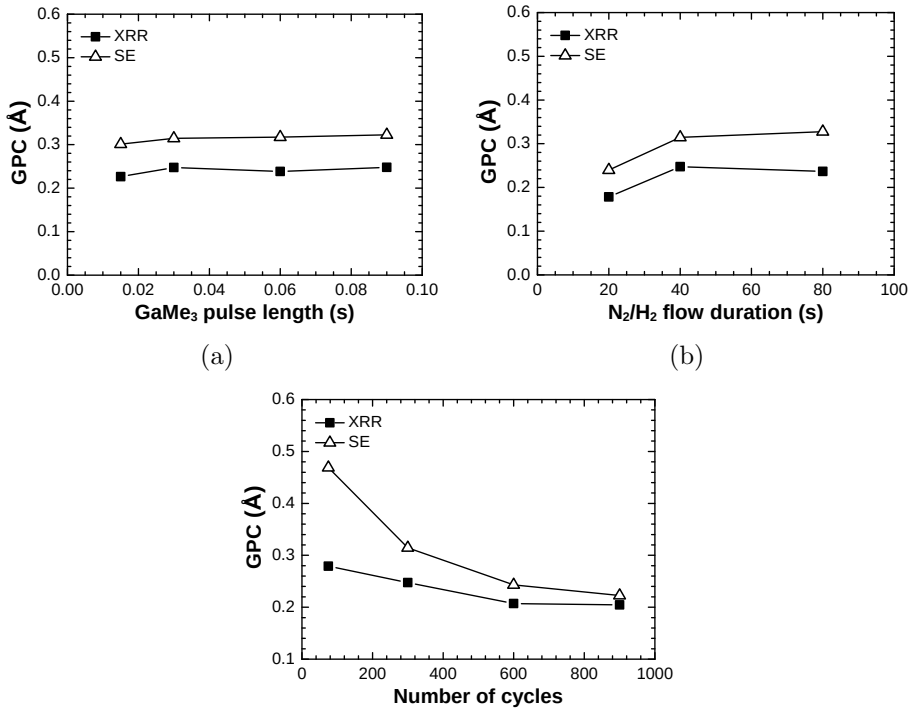

Figure 6.6: (a) $GaMe_3$, and (b) N_2/H_2 saturation curves at 200 °C. For the $GaMe_3$ saturation curve, N_2/H_2 flow rate and flow duration were kept constant at 50 + 50 sccm and 40 s, respectively. $GaMe_3$ pulse length was 0.03 s for the N_2/H_2 saturation curve. (c) GPC plotted as a function of the number of deposition cycles. Data suggests substrate-enhanced growth of GaN thin films.

6.3 AlN and GaN Thin Films Deposited Using Optimized HCPA-ALD Parameters

Six hundred cycles AlN and 900 cycles GaN were deposited at 200 °C using optimized HCPA-ALD parameters. Table 6.2 summarizes the SE results of these thin film samples together with the results of AlN and GaN films deposited using N_2/H_2 plasma with non-optimized parameters. Note that the non-optimized parameters used for the deposition of AlN and GaN thin films using N_2/H_2 plasma were identical to optimized parameters except the pulse lengths of $AlMe_3$ and

Table 6.2: SE results of AlN and GaN thin films deposited using N_2/H_2 plasma.

Sample	t_{avg} (nm)	Uniformity[a] of t (±%)	GPC (Å)	n_{avg}[b]	Uniformity[c] of n (±%)
AlN (0.06 s $AlMe_3$)[d]	59.2	0.57	0.99	1.94	0.28
AlN (0.1 s $AlMe_3$)	76.7	1.05	0.96	1.99	0.15
GaN (0.015 s $GaMe_3$)	18.4	1.31	0.23	2.14	0.17
GaN (0.03 s $GaMe_3$)[e]	20.1	0.77	0.22	2.17	0.32

[a]Uniformity (±%) is calculated using the formula: $[(t_{max}\text{-}t_{min})/(2\times t_{avg})]\times 100$.
[b]n_{avg} is the average refractive index at 632 nm.
[c]Uniformity (±%) is calculated using the formula: $[(n_{max}\text{-}n_{min})/(2\times n_{avg})]\times 100$.
[d]Optimized value for the HCPA-ALD of AlN.
[e]Optimized value for the HCPA-ALD of GaN.

$GaMe_3$. Furthermore, it has been shown in the previous section that the metalorganic pulse lengths used in the non-optimized recipes (0.1 s for $AlMe_3$ and 0.015 s $GaMe_3$) also result in self-limiting growth mechanism (see Figures 6.5(a) and 6.6(a)). For both AlN and GaN thin films, the use of optimized HCPA-ALD parameters resulted in a better thickness uniformity over 4 in. Si substrate. Refractive indices of AlN (0.06 s $AlMe_3$) and GaN (0.015 s $GaMe_3$) thin films were found as 1.94 and 2.14 at 632 nm, respectively. These values increased to 1.99 and 2.17 when higher metalorganic pulse lengths were employed, which might be due the deposition of denser films. Refractive index values of AlN and GaN films determined by the Cauchy dispersion function are both in good agreement with those reported in the literature [189, 207].

The change in metalorganic pulse lengths did not affect the chemical compositions of films. Chemical bonding states at the film surface (t_{etch} = 0 s) and in the bulk film (t_{etch} = 300 and 60 s for AlN and GaN, respectively) were determined for the samples deposited using optimized parameters by the evaluation of their high-resolution XPS (HR-XPS) scans (Figures 6.7 and 6.8). Al 2p HR-XPS scan obtained from the AlN film surface (Figure 6.7(a)), was fitted by two subpeaks (subpeaks A and B) located at 73.78 and 72.92 eV, corresponding to Al-O [187] and Al-N [186, 187] bonds, respectively. Upon Ar ion etching, subpeak A (corresponding to the Al-O bond) disappeared, and therefore Al 2p HR-XPS

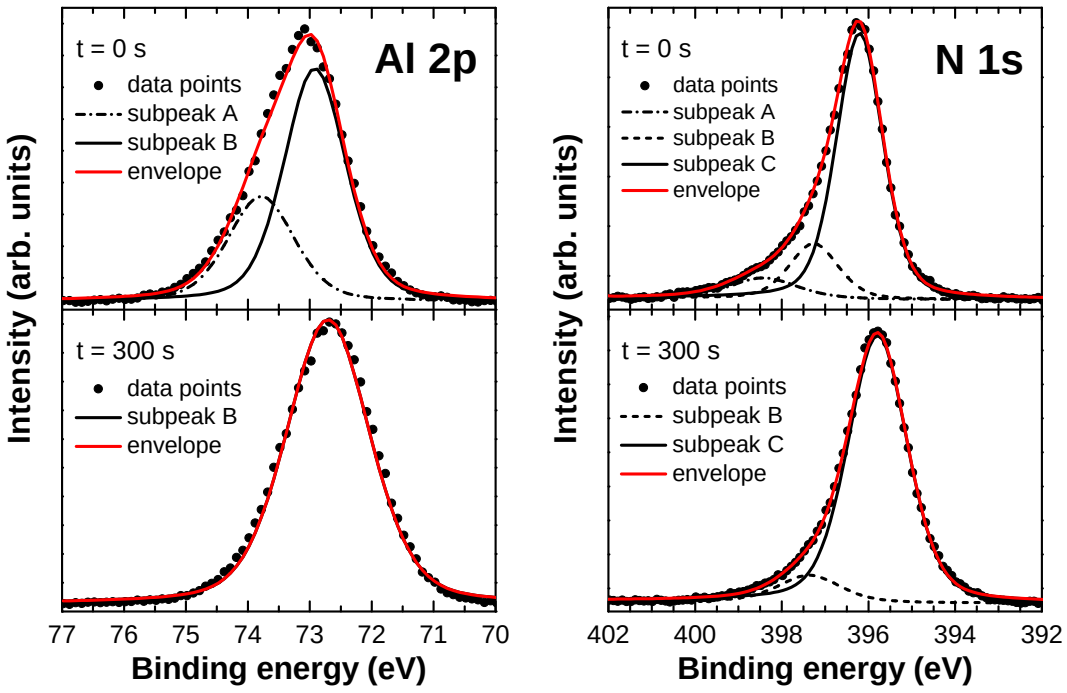

(a) (b)

Figure 6.7: (a) Al 2p, and (b) N 1s HR-XPS scans of 59.2 nm thick AlN thin film deposited on Si (100) substrate using optimized HCPA-ALD parameters.

scan was fitted with a single peak (subpeak B, 72.71 eV), which was attributed to the Al-N bonding state. Additional information about the chemical bonding states in the AlN film was provided by the N 1s spectrum (Figure 6.7(b)). N 1s scan obtained from the AlN film surface, was fitted using three subpeaks located at 398.42 (subpeak A), 397.27 (subpeak B) and 396.20 eV (subpeak C), corresponding to N-Al-O (surface only) [186], N-Al-O [186] and N-Al [186, 188] bonds, respectively. N 1s HR-XPS scan obtained after Ar ion etching revealed the existence of N-Al-O (subpeak B, 397.37 eV) and N-Al (subpeak C, 395.79 eV) bonds in the bulk film. Subpeaks corresponding to Al-N and N-Al bonds in the Al 2p and N 1s spectra, respectively, confirmed the presence of AlN, whereas the oxynitride peak (N-Al-O) was related to the <3 at.% O in bulk film detected by the XPS survey scan.

Ga 3d and N 1s HR-XPS spectra of the GaN thin film sample are given in Figures 6.8(a) and 6.8(b), respectively. Ga 3d and N 1s spectra measured from a commercial metalorganic CVD (MOCVD)-grown GaN sample were also included in these figures for comparison. Ga 3d scan revealed the existence of Ga-O [211, 212] and Ga-N [211–213] bonds at the film surface with subpeaks A (20.27 eV) and B (19.46 eV), respectively. The subpeak D located at 16.98 eV was related to the contribution from N 2s core level [212, 214]. N 1s spectrum obtained from the film surface was fitted using three subpeaks located at 396.87

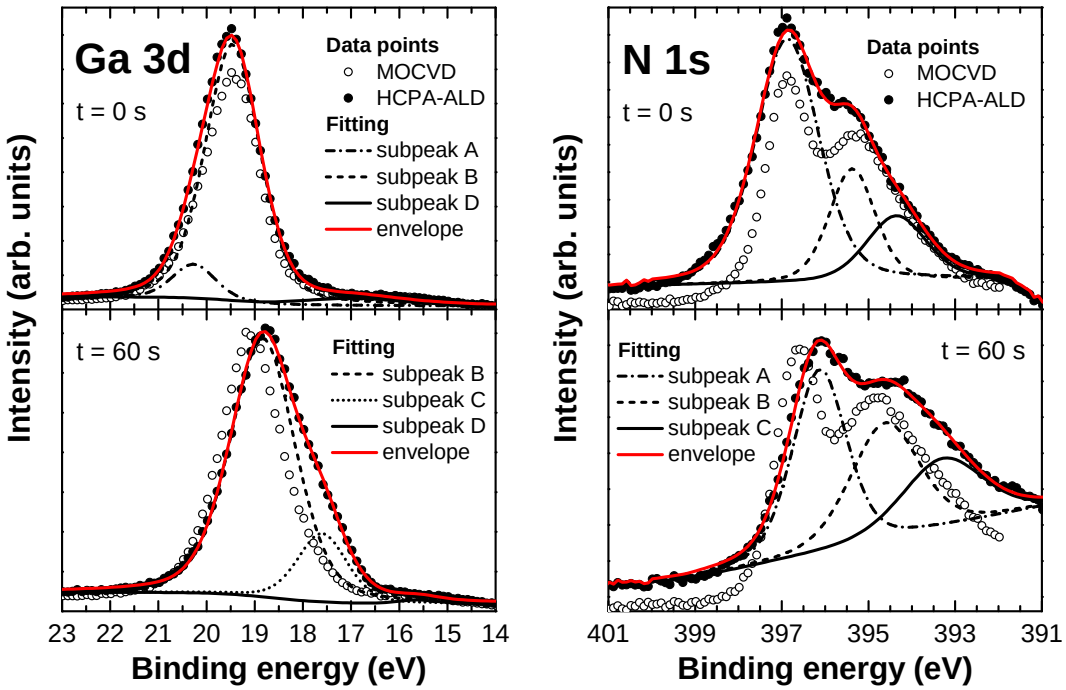

Figure 6.8: (a) Ga 3d, and (b) N 1s HR-XPS scans of 20.1 nm thick GaN thin film deposited on Si (100) substrate using optimized HCPA-ALD parameters.

(subpeak A), 395.37 (subpeak B) and 394.36 eV (subpeak C). Subpeak A was assigned as the N-Ga bond [215], whereas subpeaks B and C were identified as the Auger Ga peaks [216]. Ga 3d and N 1s spectra measured from the surface of GaN thin film deposited by HCPA-ALD were in good agreement with those measured from the surface of commercial MOCVD-grown sample. Ga 3d HR-XPS spectrum of the etched film was fitted with three subpeaks located at 18.83

(subpeak B), 17.60 (subpeak C) and 15.61 eV (subpeak D), corresponding to Ga-N and Ga-Ga [213] bonding states, and contribution from the N 2s core level, respectively. It is believed that the Ga-Ga bond is not associated with the sample, but forms during Ar ion etching due to the accumulation of metallic Ga on the surface of GaN thin film sample [209, 217]. N 1s spectrum obtained from the etched film was fitted using three subpeaks, which were again assigned as the N-Ga bond (subpeak A, 396.23 eV) and Auger Ga peaks (subpeak B, 394.72 eV and subpeak C, 393.39 eV). The spectral locations of the subpeaks corresponding to a particular bonding state, contribution, or Auger peak shifted to lower binding energies for etched GaN samples. The spectral locations of Ga 3d and N 1s peaks (t_{etch} = 60 s) were also found to be slightly different for HCPA-ALD- and MOCVD-grown GaN samples. This might be related to the reference that we used for the correction of charging effects. For etched samples it is generally convenient to use the spectral position of Ar 2p peak for determining the amount of shift needed. However, in our case, Ar 2p peaks were quite weak to be used for correction. Therefore we shifted the HR-XPS spectra of etched samples - as we were shifting the spectra obtained from film surface - by an amount determined by the location of adventitious C peak (C 1s). This approach might not work, as in the present case, if charging of the film surface and etched region are different due to their distinct chemical compositions.

GIXRD patterns of the AlN and GaN thin films deposited on Si (100) and Si (111) substrates using optimized HCPA-ALD parameters (shown in part in Figures 6.11 and 6.12) were identical to those given in Figures 6.3(a) and 6.3(b), respectively, in terms of peak positions and relative intensities of the peaks. As their GIXRD indicated, AlN and GaN thin films deposited at 200 °C were single-phase and polycrystalline with hexagonal wurtzite crystal structure. The GIXRD pattern of the 59.2 nm thick AlN thin film deposited on *c*-plane sapphire substrate was slightly different than those obtained from samples deposited on Si (100) and Si (111) substrates. The same seven reflections of the *h*-AlN phase appeared at the exact same 2Theta positions, however the intensity of (100) reflection was almost as high as that of (002) reflection. Intensity of the (103) reflection was also slightly higher for the sample deposited on *c*-plane sapphire. In the

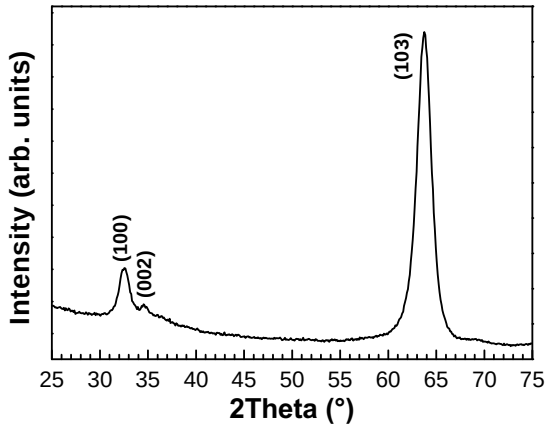

Figure 6.9: GIXRD pattern of 20.1 nm thick GaN thin film deposited on *c*-plane sapphire substrate using optimized HCPA-ALD parameters.

case of GaN, the difference between GIXRD patterns of thin films deposited on Si and *c*-plane sapphire substrates was remarkable. Figure 6.9 is the GIXRD pattern of a 20.1 nm thick GaN thin film deposited on *c*-plane sapphire. (101), (110) reflections and the peak encloses (200), (112), (201) reflections disappeared for this sample. The intensities of (100) and (002) reflections decreased, and the intensity of (103) reflection increased significantly. It should be noted that the GIXRD method, because of its geometry, is insensitive to the planes that are parallel to the substrate, therefore disappearance of the peaks might be an indication of preferred orientation.

XRR results of AlN and GaN thin films deposited on Si (100) substrates using N_2/H_2 plasma with optimized HCPA-ALD parameters are given in Table 6.3. Film thicknesses estimated by XRR were lower than those measured using SE. As shown previously, the actual film thickness lies between the values measured by SE and XRR. The mass densities (ρ) of AlN and GaN thin films were estimated as 2.82 and 5.86 g/cm^3, which are lower than the recognized values of 3.23 and 6.15 g/cm^3, respectively [218]. The estimated mass density of AlN thin film (2.82 g/cm^3) was higher than those reported in literature for AlN films deposited by PA-ALD at 200 °C (ρ = 2.34-2.65 g/cm^3) [112, 113]. XRR also revealed the root-mean-square (rms) roughnesses of these AlN and GaN thin films as 2.16 and 1.54

Table 6.3: XRR results of AlN and GaN thin films deposited using optimized HCPA-ALD parameters.

Sample	$t_{Nit.}$[a] (nm)	$t_{Ox.}$[b] (nm)	ρ (g/cm^3)	r_{rms}
AlN	53.21	0.09	2.82	2.16
GaN	17.00	1.40	5.86	1.54

[a] $t_{Nit.}$ is the thickness of nitride layer; i.e., AlN or GaN.
[b] $t_{Ox.}$ is the thickness of surface oxide layer; i.e., Al_2O_3 or Ga_2O_3.

nm, which are higher than the values directly measured using AFM. Figure 6.10 shows the 2D surface morphologies of AlN and GaN thin films deposited on Si (100) substrates. Rms roughnesses of the AlN and GaN thin films were measured from a 1 μm × 1 μm scan area as 1.97 and 0.64 nm, respectively. Rms surface roughnesses were 1.96 and 0.51 nm for AlN and GaN thin films deposited on Si (111) substrates, and 1.62 and 0.26 nm for AlN and GaN thin films deposited on c-plane sapphire substrates.

6.4 AlN and GaN Thin Films Deposited Using N_2 Plasma

The effect of plasma gas composition on the properties of deposited nitride thin films was studied. For this purpose, AlN and GaN films were deposited on Si (100) substrates using N_2 plasma, as well as N_2/H_2 plasma with decreased H_2 flow (i.e., 25 sccm). SE results of these thin film samples are summarized in Table 6.4, where the thicknesses and refractive indices of the thin films deposited using N_2/H_2 plasma (50 + 25 sccm) were comparable to those of the films deposited using optimized parameters. Thicknesses of the AlN and GaN thin films increased tremendously when N_2 was used as the plasma gas. Furthermore, refractive index values decreased upon the use of N_2 plasma, which indicates deterioration of the film quality. GIXRD patterns of the AlN and GaN thin films deposited with N_2/H_2 and N_2 plasmas are given in Figures 6.11(a) and 6.11(b), respectively,

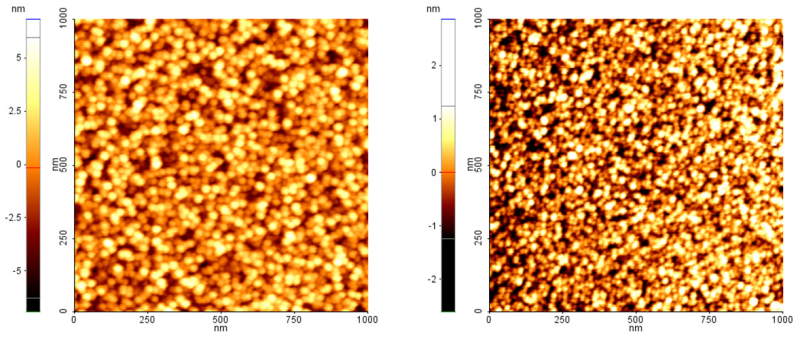

(a) (b)

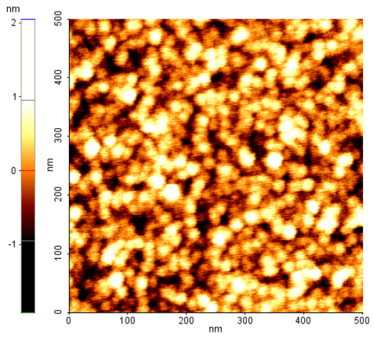

(c)

Figure 6.10: Surface morphologies of (a) 59.2 nm thick AlN, and (b), (c) 20.1 nm thick GaN thin films deposited on Si (100) substrates using optimized HCPA-ALD parameters.

together with the GIXRD patterns of films deposited using optimized HCPA-ALD parameters. As seen from these figures, decreasing H_2 flow rate from 50 to 25 sccm did not affect the crystalline qualities of AlN and GaN thin films, the same GIXRD patterns were obtained in both cases. The use of N_2 plasma without any H_2, on the other hand, resulted in amorphous GaN thin films. In the case of AlN, the crystallinity is almost lost as the reflections of the hexagonal wurtzite phase became barely visible.

We observed similar results for the AlN and GaN films deposited using previous configuration with quartz-based ICP source, where the use of N_2 plasma resulted in high concentrations of C and O impurities in the deposited films and

Table 6.4: SE results of AlN and GaN thin films deposited using N_2/H_2 and N_2 plasmas.

Reactant	t_{AlN} (nm)	n_{AlN}	t_{GaN} (nm)	n_{GaN}
N_2/H_2 plasma[a]	57.2	1.94	20.6	2.18
N_2 plasma	83.6	1.59	111.1	1.88

[a]Flow rates of N_2 and H_2 were 50 and 25 sccm, respectively.

destroyed crystallinity (see Section 5.3). The presence of C impurities (8.0 and 9.1 at.% for AlN and GaN, respectively) suggest that the organic ligands are trapped inside the growing film since N_2 plasma without any H_2 is not efficient in terms of removing the ligands of the chemisorbed trimethylmetal precursors. This might be avoided at higher temperatures, where the methyl ligands of the precursor molecules get free by self-decomposition. Although it has been thought that the high O concentrations in the films (48.5 and 4.5 at.% for AlN and GaN, respectively) are related to plasma-related oxygen contamination, recently Perros et al. [113] showed that the N_2 plasma process results in unstable AlN films, which oxidizes upon exposure to atmosphere.

It is also worth mentioning that there were particles on the surfaces of AlN and GaN films deposited using N_2 plasma. The particles were larger in the case of GaN thin film, which also showed color variations that indicate thickness non-uniformity. The formation of these particles cannot be attributed to gas-phase reactions since we already showed that 10 s purging is sufficient to avoid overlapping of the trimethylmetal precursor and plasma gas (50 sccm N_2 together with 50 sccm H_2). Therefore, the only explanation would be the formation of solid by-products as a result of the reaction between trimethylmetal compounds and N radicals. These results show that the N_2 plasma process is not eligible for the low-temperature deposition of AlN and GaN thin films.

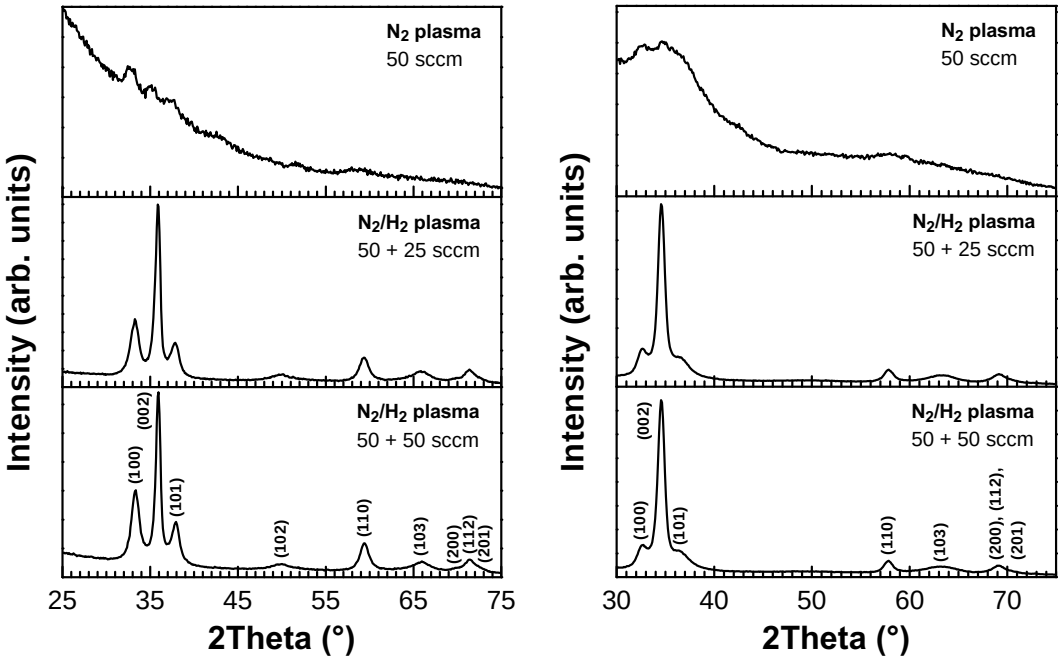

Figure 6.11: GIXRD patterns of (a) AlN, and (b) GaN thin films deposited on Si (100) substrates using N_2/H_2 (50 + 50 sccm), N_2/H_2 (50 + 25 sccm) and N_2 (50 sccm) plasmas.

6.5 Deposition of $Al_xGa_{1-x}N$ Thin Films by Digital Alloying

$Al_xGa_{1-x}N$ thin films with different compositions were deposited at 200 °C on Si (100), Si (111) and *c*-plane sapphire substrates. In order to adjust the alloy composition, different numbers of AlN and GaN subcycles were used in the main cycle; i.e., AlN:GaN = 1:3, 1:1 and 3:1. Eight hundred subcycles were deposited in each case, where AlN subcycles were deposited using the optimized HCPA-ALD parameters, whereas GaN subcycles were deposited using the optimized recipe with 0.015 s $GaMe_3$ pulse length. GIXRD patterns of the $Al_xGa_{1-x}N$ thin films are given in Figure 6.12, together with those of AlN and GaN thin films deposited using optimized process parameters. As seen from these patterns, as the number of AlN subcycles increase, the peaks shift towards higher 2Theta

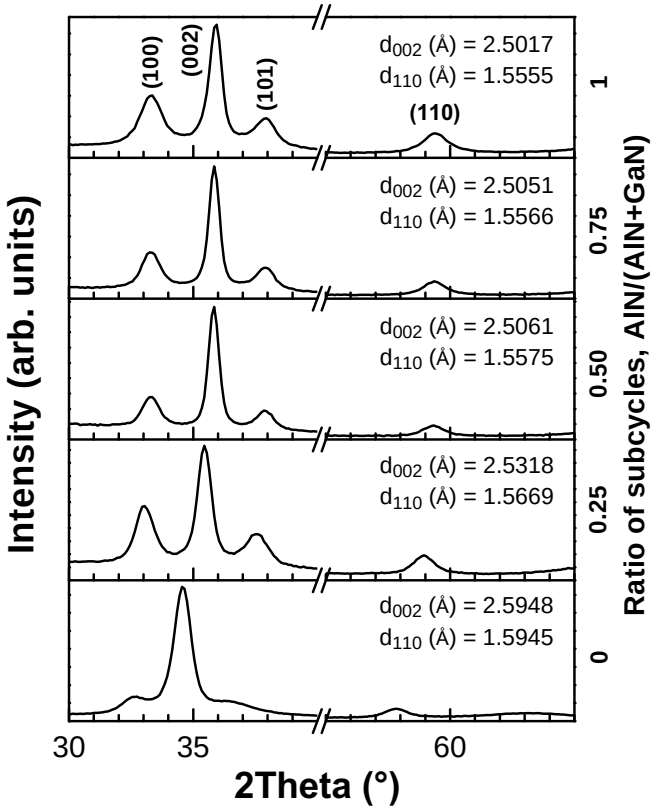

Figure 6.12: GIXRD patterns of AlN, GaN and $Al_xGa_{1-x}N$ thin films deposited on Si (100) substrates.

values due to the incorporation of Al into the wurtzite lattice. Using these data, the alloy composition, x, can be determined for each $Al_xGa_{1-x}N$ thin film using the Vegard's rule, which simply states that the lattice parameters of an alloy will vary linearly between the end members [219]. It should be noted that this rule applies to unstrained materials, where composition is the only factor affecting the lattice parameters. For the c lattice parameter of $Al_xGa_{1-x}N$, Vegard's rule is given as:

$$c_{Al_xGa_{1-x}N} = x\ c_{AlN} + (1-x)\ c_{GaN} \tag{6.1}$$

The interplanar spacing values calculated from peak positions using the well-known Bragg's law are annotated on Figure 6.12 for (002) and (110) planes.

Lattice parameters a and c were roughly calculated by substituting these d_{110} and d_{002} values, respectively, to below formula (Eq. 6.2), which relates the interplanar spacing (d_{hkl}), miller indices (hkl) and lattice parameters (a and c) for hexagonal crystals. Alloy compositions, x, were then calculated from c lattice parameters using the Vegard's rule (Eq. 6.1).

$$\frac{1}{d^2} = \frac{4}{3}\left(\frac{h^2 + hk + k^2}{a^2}\right) + \frac{l^2}{c^2} \tag{6.2}$$

Theoretical values of alloy composition ($x_{Theo.}$) were also determined using the formula,

$$x_{Theo.} = \frac{n_{sub,AlN}\ GPC_{AlN}}{n_{sub,AlN}\ GPC_{AlN} + n_{sub,GaN}\ GPC_{GaN}} \tag{6.3}$$

where $n_{sub,AlN}$ is the number of AlN subcycles, $n_{sub,GaN}$ is the number of GaN subcycles, and GPC_{AlN} and GPC_{GaN} are the deposition rates of AlN and GaN (0.015 s $GaMe_3$) thin films, which were reported as 0.99 and 0.23 Å/cycle, respectively, in the previous sections. The calculated lattice parameters, c/a ratios and alloy compositions are summarized in Table 6.5.

Although the calculated a lattice parameters of AlN and GaN are in good agreement with those reported in literature for their nominally strain-free counterparts, c lattice parameters were found to be higher (0.45% for AlN and 0.06% for GaN with respect to the highest c value reported in literature) than those of strain-free AlN and GaN thin films [219].

These results indicate the presence of strain, which limits the applicability of Vegard's rule to $Al_xGa_{1-x}N$ thin films deposited by HCPA-ALD. In order to minimize errors, alloy compositions were calculated by substituting c lattice parameters of HCPA-ALD-grown AlN and GaN films into Eq. 6.1. Theoretical values calculated using Eq. 6.3 were lower than those found by the Vegard's rule. However, it should be noted that the theoretical calculation of alloy composition is not straightforward in the present case since the deposition rate of AlN on GaN and/or the deposition rate of GaN on AlN might be different than those of

Table 6.5: Lattice parameters, c/a ratios and alloy compositions of AlN, GaN and $Al_xGa_{1-x}N$ thin films.

RS[a]	c[b] (Å)	a[c] (Å)	c/a	$x_{Veg.}$[d]	$x_{Theo.}$[e]
0 (GaN)	5.1896	3.1889	1.627	0	0
0.25	5.0636	3.1338	1.616	0.68	0.59
0.50	5.0122	3.1151	1.609	0.95	0.81
0.75	5.0101	3.1133	1.609	0.96	0.93
1 (AlN)	5.0034	3.1110	1.608	1	1

[a]RS is the ratio of subcycles; i.e., $n_{sub,AlN}/(n_{sub,AlN} + n_{sub,GaN})$.
[b]Calculated using the position of (002) reflection.
[c]Calculated using the position of (110) reflection.
[d]$x_{Veg.}$ is the alloy composition calculated from c values using Vegard's rule (Eq. 6.1).
[e]$x_{Theo.}$ is the alloy composition calculated theoretically using GPC values (Eq. 6.3).

AlN on AlN and GaN on GaN, respectively. Moreover, the HCPA-ALD of AlN exhibits a slight nucleation delay, and the GPC of GaN is higher in the beginning of growth (see Figures 6.5(c) and 6.6(c)).

Thicknesses of the $Al_{0.68}Ga_{0.32}N$, $Al_{0.95}Ga_{0.05}N$ and $Al_{0.96}Ga_{0.04}N$ films were determined as 25.4, 42.4 and 57.9 nm, respectively, using SE. These values were found to be lower than those calculated theoretically due to uncertainties in GPC values as discussed in the above paragraph. Cross-sectional bright-field scanning TEM (STEM) and HR-TEM images of $Al_{0.68}Ga_{0.32}N$ thin film are shown in Figures 6.13(a) and 6.13(b), respectively. From Figure 6.13(a), it is seen that the $Al_{0.68}Ga_{0.32}N$ layer is highly uniform. Thickness of the $Al_{0.68}Ga_{0.32}N$ thin film was measured directly from Figure 6.13(b) as 26.3 nm, which agrees well with the result obtained from SE. HR-TEM image (Figure 6.13(b)) and selected area electron diffraction (SAED) pattern revealed the polycrystalline nature of this sample, which has also been indicated in Figure 6.12 for the film deposited on Si (100) substrate.

In the previous sections, we reported the refractive index values of AlN (0.06 s $AlMe_3$) and GaN (0.015 s $GaMe_3$) as 1.94 and 2.14 at 632 nm, respectively. Refractive index values decreased from 2.03 to 1.96 as the Al content of $Al_xGa_{1-x}N$ increased from 0.68 to 0.96 (Figure 6.14(a)). Refractive indices of the $Al_xGa_{1-x}N$

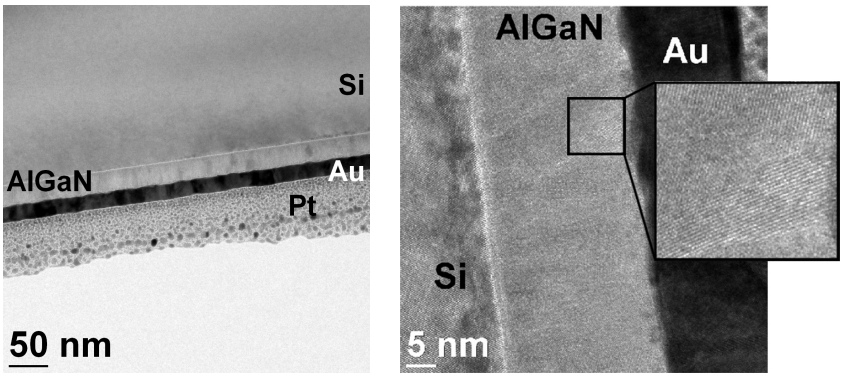

(a) (b)

Figure 6.13: Cross-sectional (a) bright-field STEM, and (b) HR-TEM images of 25.4 nm thick $Al_{0.68}Ga_{0.32}N$ thin film deposited on Si (111) substrate using N_2/H_2 plasma.

thin films were found to be quite close to that of AlN ($n = 1.94$) since the ternary alloys deposited in this study were all Al-rich. Optical transmission spectra of AlN, GaN and $Al_xGa_{1-x}N$ thin films deposited on double side polished sapphire substrates at 200 °C are given in Figure 6.14(b). The optical transmission spectrum of sapphire is also included in the figure. Film transmissions were found to be equal to the substrate transmission (~93%) in the visible spectrum, indicating absorption-free films. A significant decrease in the UV transmission was observed at wavelengths <260 nm, which is caused by the main band gap absorption. In addition, optical band edge values of the films shifted to lower wavelengths with increasing Al content. The transmission data obtained from a 20.1 nm thick GaN film exhibited a weak shoulder at lower wavelength values. The widening of the absorption edge particularly observed for this thin film sample might be attributed to strain-induced defects [220] and/or quantum confinement effect [221] due to the small crystallite size, which was estimated as 9.3 nm by LPA.

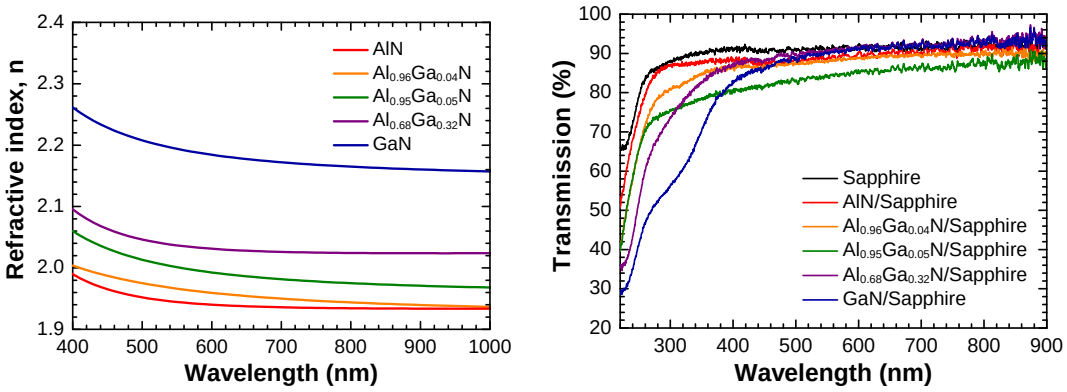

(a) (b)

Figure 6.14: (a) Spectral refractive indices, and (b) optical transmission spectra of AlN, GaN and $Al_xGa_{1-x}N$ thin films deposited Si (100) and double side polished *c*-plane sapphire substrates, respectively.

6.6 HCPA-ALD of InN Thin Films

As the 4th and 6th runs following the integration of HCP source, InN thin films were deposited on Si (100) and HCPA-ALD-AlN/Si (100) substrates at 200 °C using recipes generated with conjecture. Eight hundred cycles were deposited using 1 s CpIn/10 s Ar purge/40 s, 50 + 50 sccm (or 50 sccm), 300 W N_2/H_2 (or NH_3) plasma/10 s Ar purge. Elemental compositions of these thin film samples are summarized in Table 6.6. Samples deposited on Si substrates using N_2/H_2 plasma were uniform in color, whereas the ones deposited using NH_3 plasma exhibited light and dark regions. GPC was quite low for films deposited on Si (100) substrates as understood from XPS measurements, which detected Si at the film surfaces. GPC of the CpIn-N_2/H_2 plasma process on HCPA-ALD-AlN/Si (100) substrate was higher than that of the CpIn-N_2/H_2 plasma process on Si (100); the underlying AlN layer was detected after 80 s of Ar ion etching. O was detected in all samples with high concentrations. There were no C impurities in the films deposited using N_2/H_2 plasma, whereas ~10-13 at.% C was detected in films deposited using NH_3 plasma, after 20 s of Ar ion etching.

Table 6.6: XPS survey scan results of thin film samples deposited using CpIn-N_2/H_2 and CpIn-NH_3 HCPA-ALD processes.

Reactant and substrate	t_{etch} (s)	Elemental composition (at.%) In	N	O	C	Si
N_2/H_2 plasma[a]						
Si (100)	0	2.71	28.79	26.15	6.20	36.14
	20	5.66	16.00	14.34	-	64.00
AlN/Si (100)	0	29.32	22.95	30.86	16.87	
	60	47.35	16.69	35.96	-	-
NH_3 plasma[b]						
Si (100) (dark region)	0	13.98	46.21	18.12	19.21	2.49
	20	22.45	35.85	16.81	10.68	14.20
Si (100) (light region)	0	13.81	44.84	16.83	20.14	4.38
	20	28.67	34.95	15.71	13.34	7.34

[a] 4^{th} run following the integration of HCP source.
[b] 6^{th} run following the integration of HCP source.

GIXRD patterns of thin film samples deposited on Si (100) and AlN/Si (100) substrates using CpIn-NH_3 and CpIn-N_2/H_2 HCPA-ALD processes are given in Figure 6.15. Films deposited on Si (100) substrates using N_2/H_2 and NH_3 plasmas were found to be composed of tetragonal In (*t*-In) and cubic In_2O_3 (*c*-In_2O_3) phases. For the sample deposited on AlN/Si (100) substrate using N_2/H_2 plasma, on the other hand, GIXRD results indicated the existence of hexagonal wurtzite InN (*h*-InN) phase in addition to the *t*-In and *c*-In_2O_3 phases. In this pattern, reflections that belong to the underlying *h*-AlN film are also apparent. These reflections can be avoided by decreasing the angle of incident X-ray beam (i.e., ω).

TEM and HR-TEM images, as well as the SAED pattern of the film deposited on AlN/Si (100) substrate using CpIn-N_2/H_2 HCPA-ALD process are presented in Figure 6.16. Although the deposited material was shown to be composed of polycrystalline *h*-InN, *t*-In and *c*-In_2O_3 phases using GIXRD, it was labeled as "InN" in TEM and HR-TEM images for convenience. The deposit was observed to be in the form of large particles (Figures 6.16(a)-6.16(c)). The height of the

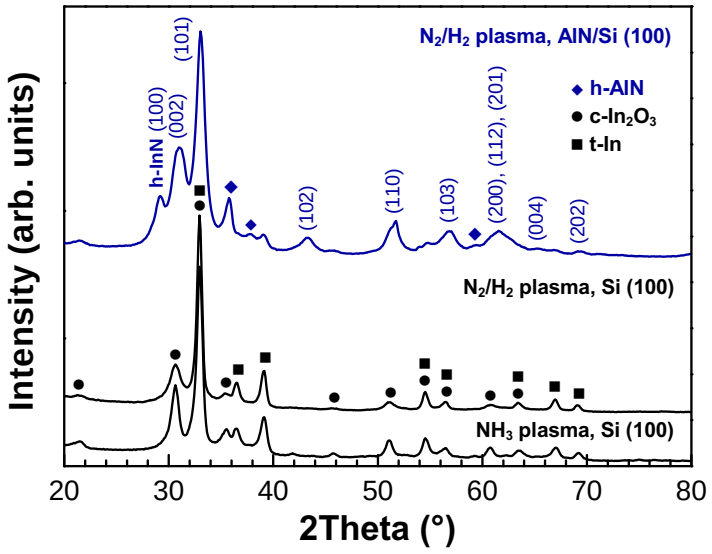

Figure 6.15: GIXRD patterns of the thin films deposited on Si (100) and AlN/Si (100) substrates using CpIn-NH_3 and CpIn-N_2/H_2 plasma processes.

particle shown in the left side of Figure 6.16(c) was measured from this image as ~38 nm. As shown in Figure 6.16(d), there were also regions, where the material was deposited in a continuous manner. The thickness of continuous layer was measured as ~25.5 nm from Figure 6.16(d). HR-TEM images shown in Figures 6.16(d) and 6.16(e), as well as the SAED pattern (Figure 6.16(f)) confirmed the polycrystalline nature of deposited material. The bright spots on the polycrystalline diffraction rings indicated the presence of large crystallites.

The high O concentrations in deposited films may be related to the residual water vapor on the walls of the chamber, which decays with each metalorganic pulse. In order to further investigate this, CpIn-N_2/H_2 HCPA-ALD process was repeated as the 59^{th} run following the integration of HCP source. Si (100), Si (111), as well as a 59.2 nm thick AlN film deposited by HCPA-ALD on Si (100) were used as the substrates. Upon the application of 800 InN cycles, the yellowish color of the AlN/Si (100) substrate became purple (Figure 6.17), which indicates an increase in film thickness. The deposited film was highly uniform over the substrate as seen in Figure 6.17(b).

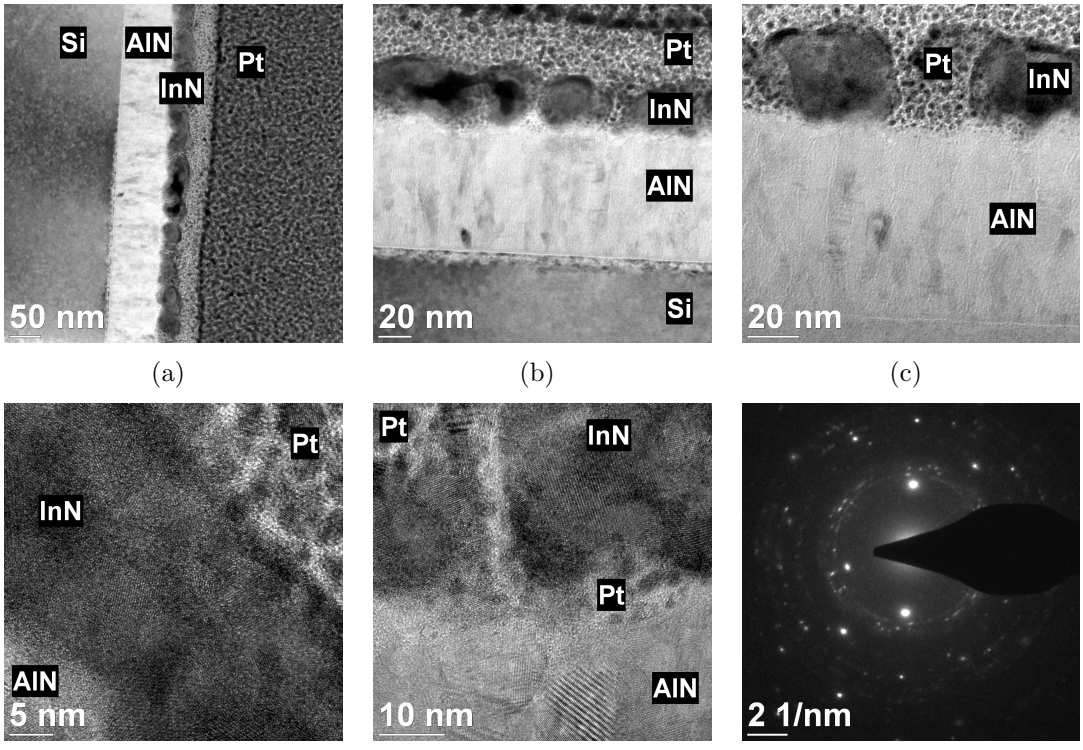

Figure 6.16: (a)-(c) TEM and (d), (e) HR-TEM images, and (f) SAED pattern of the thin film deposited on a AlN/Si (100) substrate using CpIn-N_2/H_2 HCPA-ALD process. Deposited material was labeled as "InN" for convenience.

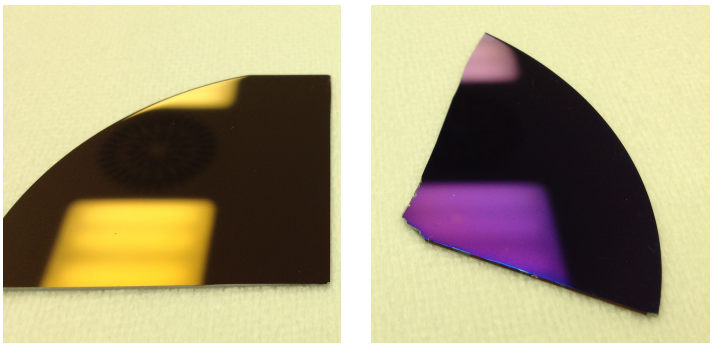

(a) (b)

Figure 6.17: Photographs of the HCPA-ALD-AlN/Si (100) substrate (a) before and (b) after the CpIn-N_2/H_2 HCPA-ALD process.

GIXRD patterns of the samples deposited on Si (100), Si (111) and AlN/Si (100) substrates are given in Figure 6.18. All samples were identified as polycrystalline, single-phase *h*-InN. There were no signs of the *t*-In and *c*-In_2O_3 phases. These results suggest that single-phase *h*-InN thin films can be deposited using HCPA-ALD given that the chamber is free of residual water. Residual water vapor contaminates the chamber upon exposure to atmosphere. In this respect, using a load lock is particularly important in the case of InN deposition. Although residual water can be removed from the chamber walls by performing bake-out and/or pulsing metalorganic precursors, it would not be feasible to perform such procedures before each deposition.

XRR data of the InN thin film deposited on Si (111) substrate was fitted using a 4-layer model (i.e., In_2O_3/InN/SiO_2/Si). The results indicated negligible thickness and a quite low mass density for this film. For the fitting of the XRR data of InN film deposited on AlN/Si (100) substrate, on the other hand, a 6-layer model was used; i.e., In_2O_3/InN/Al_2O_3/AlN/SiO_2/Si. Thicknesses of the InN and In_2O_3 layers were estimated as 34.87 and 0.08 nm, respectively. Mass density was found to be 2.89 g/cm^3, which is very low compared to the recognized value of 6.81 g/cm^3 [218]. XRR fitting also revealed the surface roughness as 3 nm.

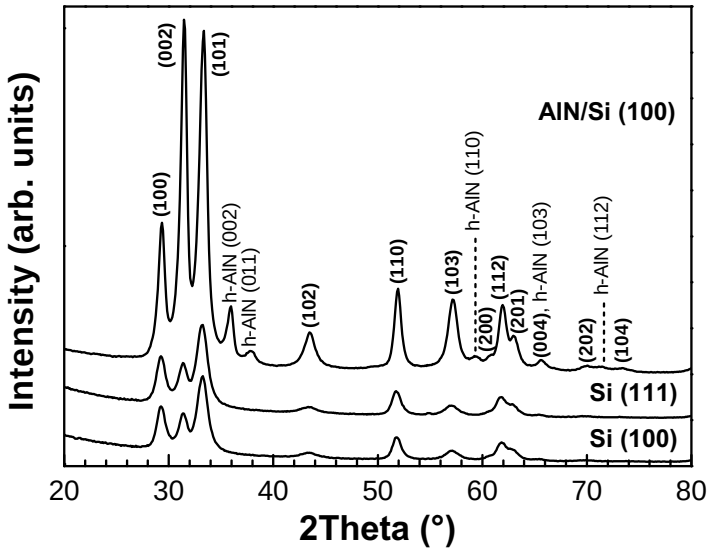

Figure 6.18: GIXRD patterns of the InN thin films deposited on Si (100), Si (111) and AlN/Si (100) substrates using the CpIn-N_2/H_2 HCPA-ALD process. GIXRD patterns indicate a hexagonal wurtzite crystal structure.

Surface morphologies of InN thin films deposited on Si (111) and AlN/Si (100) substrates are shown in Figures 6.19 and 6.20, respectively. It is seen from Figure 6.19 that InN deposited on Si (111) was discontinuous. As a result of the CpIn-N_2/H_2 HCPA-ALD process, InN islands were formed on the Si substrate. Heights of these islands were measured from Figure 6.19 as 16-18 nm. When compared to the films deposited on Si, InN thin films deposited AlN/Si (100) substrates exhibited a different morphology as seen in Figures 6.20(a) and 6.20(b). Smaller islands were coalesced to form a continuous InN layer. Rms roughness values were measured as 3.14 and 2.93 nm from 1 μm × 1 μm and 500 nm × 500 nm scan areas, respectively, which are both in good agreement with the result obtained by XRR.

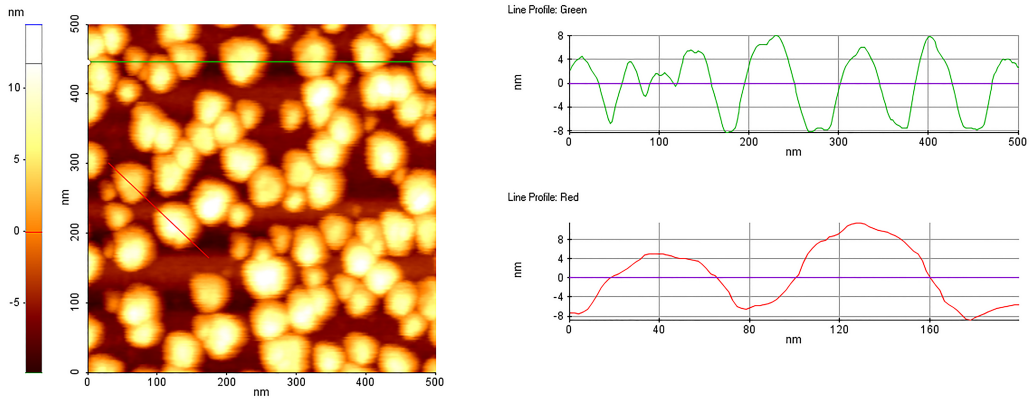

Figure 6.19: 500 nm × 500 nm 2D AFM image of InN deposited on Si (111) substrate using CpIn and N_2/H_2 plasma. Line profiles are also shown in the figure.

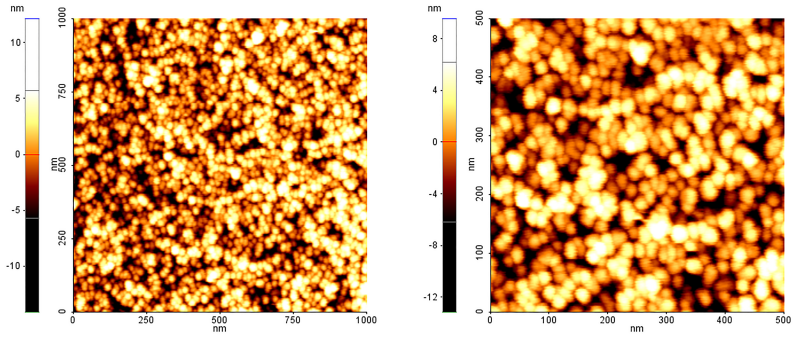

(a) (b)

Figure 6.20: (a) 1 μm × 1 μm, and (b) 500 nm × 500 nm 2D AFM images of the InN thin film deposited on AlN/Si (100) substrate using CpIn and N_2/H_2 plasma.

Chapter 7

Conclusions and Future Work

In this dissertation, plasma-assisted atomic layer deposition (PA-ALD) of III-nitride (AlN, GaN and InN) thin films was investigated with the motivation of (i) low-temperature deposition of III-nitride thin films on sensitive device layers and substrates, (ii) deposition of the ternary and quaternary alloys of III-nitride family with desired composition and hence electrical/optical properties, and (iii) template-based synthesis of III-nitride nanostructures for improved efficiency and/or sensitivity in selected applications through surface area enhancement.

We reported on the PA-ALD of randomly oriented polycrystalline wurtzite AlN thin films at temperatures ranging from 100-500 °C. PA-ALD parameters were optimized for the trimethylaluminum ($AlMe_3$)-ammonia (NH_3) plasma and $AlMe_3$-N_2/H_2 plasma processes, which exhibited constant growth growth per cycle (GPC) values of ~0.86 and ~0.55 Å, respectively, at temperatures ranging from 100 to 200 °C. Within the ALD temperature windows (i.e., 100-200 °C for both NH_3 and N_2/H_2 plasma processes), film thicknesses increased linearly with the number of deposition cycles and no incubation behavior was observed. AlN films deposited at temperatures within the ALD window were C-free and had relatively low O concentrations (<3 at.%) despite 5N-grade plasma gases were used without any further purification. Furthermore, these films exhibited low roughness values and showed decent optical and electrical characteristics.

Template-based synthesis of high surface area AlN hollow nanofibers, which might potentially be used in high temperature ambient chemical sensing applications, was also demonstrated by combining the electrospinning, PA-ALD and calcination processes. Scanning electron microscopy studies showed that there is a critical wall-thickness-to-inner-diameter ratio for AlN hollow nanofibers to preserve their shapes after the polymeric template has been removed by calcination. Transmission electron microscopy (TEM) images indicated uniform wall thicknesses along the fiber axes. Synthesized AlN hollow nanofibers were polycrystalline with a hexagonal crystal structure as determined by high-resolution TEM (HR-TEM) and selected area electron diffraction.

Our initial efforts for depositing GaN thin films using triethylgallium ($GaEt_3$) or trimethylgallium ($GaMe_3$) with NH_3 plasma resulted in amorphous thin films with high O concentrations (~20 at.%). InN trials were even worse, trimethylindium ($InMe_3$)-NH_3 plasma and cyclopentadienyl indium (CpIn)-NH_3 plasma processes both exhibited very low deposition rates and the resulting films had very high O concentrations. Although - at first - the most probable source of this contamination was presumed as the O-containing impurities in the 5N-grade NH_3 gas, subsequent experiments revealed the true source as the quartz tube of inductively coupled RF-plasma (ICP) source itself. In view of these circumstances, the choice of N-containing plasma gas (N_2, N_2/H_2 or NH_3) determined the severity of O incorporation into AlN and GaN films deposited by PA-ALD. In the case of AlN thin films, lowest O concentrations were obtained using NH_3 plasma (~1.5 at.%). O concentration in AlN films increased tremendously (i.e., >45 at.%) when N_2 or certain N_2/H_2 plasma processes were used. PA-ALD processes designed for GaN, on the other hand, showed an adverse response to the use of N_2, N_2/H_2 and NH_3 plasma gases in terms of O incorporation. Film deposited using NH_3 plasma had ~20 at.% O in the bulk film. The use of N_2 or N_2/H_2 plasma decreased this value to <5 at.%. We were able to deposit polycrystalline wurtzite GaN thin films with 4.7 at.% O and 4.2 at.% C impurities using the $GaMe_3$-N_2/H_2 PA-ALD process at 200 °C. These results suggested that the choice of N-containing plasma gas is highly precursor dependent and might not be anticipated for other PA-ALD processes.

As an effort to completely avoid plasma-related oxygen contamination problem, we replaced the original quartz-based ICP source of the ALD system with a stainless steel hollow cathode plasma (HCP) source; thereby demonstrated the hollow cathode PA-ALD (HCPA-ALD) of crystalline AlN, GaN and $Al_xGa_{1-x}N$ thin films at low temperature (i.e., 200 °C) using trimethylmetal precursors and NH_3 or N_2/H_2 plasma. Preliminary depositions carried out using non-optimized process parameters resulted with reasonably uniform AlN and GaN films with wafer-level non-uniformities less than ±1.5%. X-ray photoelectron spectroscopy (XPS) survey scans detected 2.5-3.0 and 1.5-1.7 at.% O in these AlN and GaN thin films, respectively, after they were etched *in situ* with a beam of Ar ions under ultra high vacuum conditions. C was detected only at the film surfaces and there were no C impurities in the bulk films as determined by XPS. Since the Ar ion etching may lead to substantial errors in the quantification of O and C impurities present in AlN and GaN thin films, complimentary secondary ion mass spectroscopy analyses were performed on the films deposited using NH_3 plasma, which revealed the presence of O, C (both <1 at.%) and H impurities in the films. Grazing-incidence X-ray diffraction (GIXRD) patterns exhibited polycrystalline AlN and GaN thin films with (hexagonal) wurtzite crystal structure. Crystallite sizes were 19.2 and 24.8 nm for AlN, and 10.2 and 9.3 nm for GaN films deposited using NH_3 and N_2/H_2 plasmas, respectively. HR-TEM image of the GaN thin film deposited using NH_3 plasma further revealed the existence of relatively large crystals in the film, which can extend along the film thickness.

HCPA-ALD parameters were optimized at 200 °C for the deposition of AlN and GaN thin films. Trimethylmetal precursor and N_2/H_2 saturation curves evidenced the self-limiting growth of AlN and GaN at this temperature. AlN exhibited linear growth with a slight nucleation delay. GPC of AlN was high; i.e., ~1.0 Å. In the case of GaN, GPC decreased with the increasing number of deposition cycles, which indicates substrate-enhanced growth. GPC was found to be 0.22 Å for the 900-cycle GaN deposition. 59.2 nm thick AlN and 20.1 nm thick GaN thin films deposited using optimized process parameters were characterized using spectroscopic ellipsometry, high-resolution XPS (HR-XPS), GIXRD, X-ray reflectivity (XRR), and atomic force microscopy (AFM). Refractive indices of

AlN and GaN thin films were determined as 1.94 and 2.17 at 632 nm, respectively, using the Cauchy dispersion function. Al 2p (Ga 3d) and N 1s HR-XPS spectra confirmed the metal nitride bonding states in AlN (GaN) films. The mass densities of AlN and GaN thin films were estimated as 2.82 and 5.86 g/cm^3 using XRR. Rms roughness values determined by XRR were higher than those directly measured using AFM; i.e., 1.97 and 0.64 nm for AlN and GaN thin films deposited on Si (100) substrates, respectively. Results of the depositions carried out using N_2 plasma have shown that this process results in low-quality films, and therefore is not eligible for the low-temperature deposition of AlN and GaN.

$Al_xGa_{1-x}N$ thin films were obtained via digital alloying, where the main HCPA-ALD cycle consisted of different number of AlN and GaN subcycles; i.e., AlN:GaN = 1:3, 1:1 and 3:1. Alloy compositions were determined by the Vegard's rule as 0.68 (AlN:GaN = 1:3), 0.95 (1:1) and 0.96 (3:1) using the c lattice parameters, which were roughly calculated from the (002) peak positions. The c lattice parameters of binary AlN and GaN thin films were also estimated and used for the calculations in order to minimize the errors that may arise due to the presence of strain in deposited films. Refractive index values of the $Al_xGa_{1-x}N$ thin films decreased from 2.03 to 1.96 as the Al content increased from 0.68 to 0.96. Transmissions of AlN, GaN and $Al_xGa_{1-x}N$ thin films were equal to the substrate transmission (~93%) in the visible spectrum, indicating absorption-free films. Optical band edge values of the $Al_xGa_{1-x}N$ films shifted to lower wavelengths with increasing Al content, which confirms the adjustability of band edge values with compositional digital alloying.

HCPA-ALD of InN was also studied using CpIn with NH_3 or N_2/H_2 plasma. Films deposited on Si (100) substrates immediately after the integration of HCP source were found to be composed of tetragonal In (t-In) and cubic In_2O_3 (c-In_2O_3) phases. For the sample deposited on AlN/Si (100) substrate using N_2/H_2 plasma, on the other hand, GIXRD results indicated the existence of hexagonal wurtzite InN (h-InN) phase in addition to the t-In and c-In_2O_3 phases. The high O concentrations in deposited films were found to be related to the residual water vapor on the walls of the chamber, which decays with each metalorganic pulse. CpIn-N_2/H_2 HCPA-ALD process, which was realized as the 59$^{\text{th}}$ run following

the integration of HCP source, resulted with the formation of polycrystalline, single-phase *h*-InN on Si (100), Si (111) and AlN/Si (100) substrates. The GPC of InN on Si substrates was negligible as determined by XRR. Accordingly, AFM images indicated the formation of InN islands on Si substrates. The thickness of the InN thin film deposited on AlN/Si (100) substrate was estimated using XRR as ~35 nm. Mass density was found to be 2.89 g/cm^3, which is quite low compared to the recognized value of 6.81 g/cm^3.

Our experimental studies showed the promise of PA-ALD technique for obtaining thin films and nanostructures of binary and ternary III-nitrides at relatively low temperatures. Our achievements might lead to a vast amount of materials and device research. Potential future research directions are listed below.

- Investigation of *ex situ* and *in situ* surface pretreatments, and different substrates for AlN and GaN thin films, and for promoting the GPC of InN on Si.
- HCPA-ALD of $In_xAl_{1-x}N$ and $In_xGa_{1-x}N$ thin films via digital alloying using $AlMe_3$, $GaMe_3$ and CpIn as the Al, Ga and In precursors, respectively.
- HCPA-ALD of InN thin films using $InMe_3$ as the In precursor.
- HCPA-ALD of doped III-nitride thin films using Mg and Si precursors for p- and n-type doping, respectively.
- Investigation of the electrical properties of HCPA-ALD-grown GaN and InN thin films; i.e., carrier type, concentration and mobility determined by Hall-effect measurements.
- Investigation of the effect of post-deposition annealing on the structural, optical and electrical properties of HCPA-ALD-grown III-nitride thin films.
- Demonstration of the electronic and optoelectronic device applications of HCPA-ALD-grown III-nitride thin films and their alloys; i.e., thin film transistors, resistive memories, photodetectors, etc.
- Template-based synthesis of III-nitride nanostructures for improved efficiency in selected applications.

Bibliography

[1] S. Strite and H. Morkoç, "GaN, AlN, and InN: A review," *Journal of Vacuum Science and Technology B*, vol. 10, no. 4, pp. 1237 – 1266, 1992.

[2] O. Ambacher, "Growth and applications of group III-nitrides," *Journal of Physics D: Applied Physics*, vol. 31, no. 20, pp. 2653 – 2710, 1998.

[3] S. C. Jain, M. Willander, J. Narayan, and R. van Overstraeten, "III-nitrides: Growth, characterization, and properties," *Journal of Applied Physics*, vol. 87, no. 3, pp. 965 – 1006, 2000.

[4] J. Wu, W. Walukiewicz, K. M. Yu, J. W. Ager-III, E. E. Haller, H. Lu, W. J. Schaff, Y. Saito, and Y. Nanishi, "Unusual properties of the fundamental band gap of InN," *Applied Physics Letters*, vol. 80, no. 21, pp. 3967 – 3969, 2002.

[5] A. G. Bhuiyan, A. Hashimoto, and A. Yamamoto, "Indium nitride (InN): A review on growth, characterization, and properties," *Journal of Applied Physics*, vol. 94, no. 5, pp. 2779 – 2808, 2003.

[6] J. Wu and W. Walukiewicz, "Band gaps of InN and group III nitride alloys," *Superlattices and Microstructures*, vol. 34, no. 1 - 2, pp. 63 – 75, 2003.

[7] K. S. A. Butcher and T. L. Tansley, "InN, latest development and a review of the band-gap controversy," *Superlattices and Microstructures*, vol. 38, no. 1, pp. 1 – 37, 2005.

[8] J. Wu, "When group-III nitrides go infrared: New properties and perspectives," *Journal of Applied Physics*, vol. 106, no. 1, p. 011101 (28pp), 2009.

[9] Z. Chen, S. Newman, D. Brown, R. Chung, S. Keller, U. K. Mishra, S. P. Denbaars, and S. Nakamura, "High quality AlN grown on SiC by metal organic chemical vapor deposition," *Applied Physics Letters*, vol. 93, no. 19, p. 191906 (3pp), 2008.

[10] M. Alevli, G. Durkaya, A. Weerasekara, A. G. U. Perera, N. Dietz, W. Fenwick, V. Woods, and I. Ferguson, "Characterization of InN layers grown by high-pressure chemical vapor deposition," *Applied Physics Letters*, vol. 89, no. 11, p. 112119 (3pp), 2006.

[11] M. E. Lin, B. Sverdlov, G. L. Zhou, and H. Morkoç, "A comparative study of GaN epilayers grown on sapphire and SiC substrates by plasma-assisted molecular-beam epitaxy," *Applied Physics Letters*, vol. 62, no. 26, pp. 3479 – 3481, 1993.

[12] R. L. Puurunen, "Surface chemistry of atomic layer deposition: A case study for the trimethylaluminum/water process," *Journal of Applied Physics*, vol. 97, no. 12, p. 121301 (52pp), 2005.

[13] L. Bárdoš, "Radio frequency hollow cathodes for the plasma processing technology," *Surface and Coatings Technology*, vol. 86 - 87, no. 1 - 3 (pt. 2), pp. 648 – 656, 1996.

[14] K. S. A. Butcher, B. W. Kemp, I. B. Hristov, P. Terziyska, P. W. Binsted, and D. Alexandrov, "Gallium nitride film growth using a plasma based migration enhanced afterglow chemical vapor deposition system," *Japanese Journal of Applied Physics*, vol. 51, no. 1 (pt. 2), p. 01AF02 (5pp), 2012.

[15] M. Ritala and M. Leskelä, *Handbook of Thin Film Materials: Deposition and Processing of Thin Films*, vol. 1, ch. 2. London: Academic Press, 2002.

[16] J. Antson and T. Suntola, "Method for producing compound thin films," Nov. 15 1977. US Patent 4,058,430.

[17] S. G. Lindfors, A. J. Pakkala, and T. S. Suntola, "Apparatus for performing growth of compound thin films," June 28 1983. US Patent 4,389,973.

[18] S. G. Lindfors, A. J. Pakkala, and T. S. Suntola, "Method for performing growth of compound thin films," Nov. 1 1983. US Patent 4,413,022.

[19] T. Suntola, "Atomic layer epitaxy," *Materials Science Reports*, vol. 4, no. 5, pp. 261 – 312, 1989.

[20] M. de Keijser and C. van Opdorp, "Atomic layer epitaxy of gallium arsenide with the use of atomic hydrogen," *Applied Physics Letters*, vol. 58, no. 11, pp. 1187 – 1189, 1991.

[21] A. Sherman, "Sequential chemical vapor deposition," June 29 1999. US Patent 5,916,365.

[22] H. B. Profijt, S. E. Potts, M. C. M. van de Sanden, and W. M. M. Kessels, "Plasma-assisted atomic layer deposition: Basics, opportunities, and challenges," *Journal of Vacuum Science and Technology A*, vol. 29, no. 5, p. 050801 (26pp), 2011.

[23] M. Leskelä and M. Ritala, "Atomic layer deposition (ALD): From precursors to thin film structures," *Thin Solid Films*, vol. 409, no. 1, pp. 138 – 146, 2002.

[24] S. M. George, "Atomic layer deposition: An overview," *Chemical Reviews*, vol. 110, no. 1, pp. 111 – 131, 2010.

[25] V. Miikkulainen, M. Leskelä, M. Ritala, and R. L. Puurunen, "Crystallinity of inorganic films grown by atomic layer deposition: Overview and general trends," *Journal of Applied Physics*, vol. 113, no. 2, p. 021301 (101pp), 2013.

[26] H. Kim, "Characteristics and applications of plasma enhanced-atomic layer deposition," *Thin Solid Films*, vol. 519, no. 20, pp. 6639 – 6644, 2011.

[27] J. Dendooven, D. Deduytsche, J. Musschoot, R. L. Vanmeirhaeghe, and C. Detavernier, "Conformality of Al_2O_3 and AlN deposited by plasma-enhanced atomic layer deposition," *Journal of the Electrochemical Society*, vol. 157, no. 4, pp. G111 – G116, 2010.

[28] "Material safety data sheet: Trimethyaluminium," tech. rep., SAFC Hightech, January 2007.

[29] "Material safety data sheet: Trimethygallium," tech. rep., SAFC Hightech, February 2007.

[30] "Product data sheet: Triethylgallium," tech. rep., AkzoNobel, May 2012.

[31] "Material safety data sheet: Trimethyindium," tech. rep., SAFC Hightech, February 2007.

[32] J. W. Elam, A. B. F. Martinson, M. J. Pellin, and J. T. Hupp, "Atomic layer deposition of In_2O_3 using cyclopentadienyl indium: A new synthetic route to transparent conducting oxide films," *Chemistry of Materials*, vol. 18, no. 15, pp. 3571 – 3578, 2006.

[33] J. W. Klaus, S. J. Ferro, and S. M. George, "Atomic layer deposition of tungsten nitride films using sequential surface reactions," *Journal of The Electrochemical Society*, vol. 147, no. 3, pp. 1175 – 1181, 2000.

[34] S. B. S. Heil, J. L. van Hemmen, M. C. M. van de Sanden, and W. M. M. Kessels, "Reaction mechanisms during plasma-assisted atomic layer deposition of metal oxides: A case study for Al_2O_3," *Journal of Applied Physics*, vol. 103, no. 10, p. 103302 (14pp), 2008.

[35] E. Langereis, S. B. S. Heil, H. C. M. Knoops, W. Keuning, M. C. M. van de Sanden, and W. M. M. Kessels, "In situ spectroscopic ellipsometry as a versatile tool for studying atomic layer deposition," *Journal of Physics D: Applied Physics*, vol. 42, no. 7, p. 073001 (19pp), 2009.

[36] J. W. Elam, M. Schuisky, J. D. Ferguson, and S. M. George, "Surface chemistry and film growth during TiN atomic layer deposition using TDMAT and NH_3," *Thin Solid Films*, vol. 436, no. 2, pp. 145 – 156, 2003.

[37] M. Juppo, A. Rahtu, and M. Ritala, "In situ mass spectrometry study on surface reactions in atomic layer deposition of TiN and Ti(Al)N thin films," *Chemistry of Materials*, vol. 14, no. 1, pp. 281 – 287, 2002.

[38] J. Kwon, M. Dai, M. D. Halls, E. Langereis, Y. J. Chabal, and R. G. Gordon, "In situ infrared characterization during atomic layer deposition of lanthanum oxide," *Journal of Physical Chemistry C*, vol. 113, no. 2, pp. 654 – 660, 2009.

[39] W. Lee, N. P. Dasgupta, H. J. Jung, J.-R. Lee, R. Sinclair, and F. B. Prinz, "Scanning tunneling spectroscopy of lead sulfide quantum wells fabricated by atomic layer deposition," *Nanotechnology*, vol. 21, no. 48, p. 485402 (4pp), 2010.

[40] S. Riedel, J. Neidhardt, S. Jansen, L. Wilde, J. Sundqvist, E. Erben, S. Teichert, and A. Michaelis, "Synthesis of $SrTiO_3$ by crystallization of SrO/TiO_2 superlattices prepared by atomic layer deposition," *Journal of Applied Physics*, vol. 109, no. 9, p. 094101 (8pp), 2011.

[41] J. W. Elam, Z. A. Sechrista, and S. M. George, "ZnO/Al_2O_3 nanolaminates fabricated by atomic layer deposition: Growth and surface roughness measurements," *Thin Solid Films*, vol. 414, no. 1, pp. 43 – 55, 2002.

[42] A. Szeghalmi, S. Senz, M. Bretschneider, U. Gösele, and M. Knez, "All dielectric hard x-ray mirror by atomic layer deposition," *Applied Physics Letters*, vol. 94, no. 13, p. 133111 (3pp), 2009.

[43] J. R. Bakke and S. F. Bent, "Formation of $Cd_xZn_{1-x}S$ films for photovoltaic buffer layers by atomic layer deposition," *ECS Transactions*, vol. 25, no. 4, pp. 9 – 14, 2009.

[44] J. W. Elam and S. M. George, "Growth of ZnO/Al_2O_3 alloy films using atomic layer deposition techniques," *Chemistry of Materials*, vol. 15, no. 4, pp. 1020 – 1028, 2003.

[45] P. Banerjee, W.-J. Lee, K.-R. Bae, S. B. Lee, and G. W. Rubloff, "Structural, electrical, and optical properties of atomic layer deposition Al-doped ZnO films," *Journal of Applied Physics*, vol. 108, no. 4, p. 043504 (7pp), 2010.

[46] S. J. Lim, S.-J. Kwon, H. Kim, and J.-S. Park, "High performance thin film transistor with low temperature atomic layer deposition nitrogen-doped ZnO," *Applied Physics Letters*, vol. 91, no. 18, p. 183517 (3pp), 2007.

[47] L. F. Hakim, S. M. George, and A. W. Weimer, "Conformal nanocoating of zirconia nanoparticles by atomic layer deposition in a fluidized bed reactor," *Nanotechnology*, vol. 16, no. 7, pp. S375 – S381, 2005.

[48] A. B. F. Martinson, J. W. Elam, J. T. Hupp, and M. J. Pellin, "ZnO nanotube based dye-sensitized solar cells," *Nano Letters*, vol. 7, no. 8, pp. 2183 – 2187, 2007.

[49] Y.-S. Min, E. J. Bae, K. S. Jeong, Y. J. Cho, J.-H. Lee, W. B. Choi, and G.-S. Park, "Ruthenium oxide nanotube arrays fabricated by atomic layer deposition using a carbon nanotube template," *Advanced Materials*, vol. 15, no. 12, pp. 1019 – 1022, 2003.

[50] M. D. Groner, S. M. George, R. S. McLean, and P. F. Carcia, "Gas diffusion barriers on polymers using Al_2O_3 atomic layer deposition," *Applied Physics Letters*, vol. 88, no. 5, p. 051907 (3pp), 2006.

[51] F. Kayaci, C. Ozgit-Akgun, I. Donmez, N. Biyikli, and T. Uyar, "Polymer-inorganic core-shell nanofibers by electrospinning and atomic layer deposition: Flexible nylon-ZnO core-shell nanofiber mats and their photocatalytic activity," *ACS Applied Materials and Interfaces*, vol. 4, no. 11, pp. 6185 – 6194, 2012.

[52] F. Kayaci, C. Ozgit-Akgun, N. Biyikli, and T. Uyar, "Surface-decorated ZnO nanoparticles and ZnO nanocoating on electrospun polymeric nanofibers by atomic layer deposition for flexible photocatalytic nanofibrous membranes," *RSC Advances*, vol. 3, no. 19, pp. 6817 – 6820, 2013.

[53] H. Ceylan, C. Ozgit-Akgun, T. S. Erkal, I. Donmez, R. Garifullin, A. B. Tekinay, H. Usta, N. Biyikli, and M. O. Guler, "Size-controlled conformal nanofabrication of biotemplated three-dimensional TiO_2 and ZnO nanonetworks," *Scientific Reports*, vol. 3, p. 2306 (7pp), 2013.

[54] J. Huang, X. Wang, and Z. L. Wang, "Controlled replication of butterfly wings for achieving tunable photonic properties," *Nano Letters*, vol. 6, no. 10, pp. 2325 – 2331, 2006.

[55] M. Knez, A. Kadri, C. Wege, U. Gösele, H. Jeske, and K. Nielsch, "Atomic layer deposition on biological macromolecules: Metal oxide coating of tobacco mosaic virus and ferritin," *Nano Letters*, vol. 6, no. 6, pp. 1172 – 1177, 2006.

[56] N. P. Dasgupta, H. J. Jung, O. Trejo, M. T. McDowell, A. Hryciw, M. Brongersma, R. Sinclair, and F. B. Prinz, "Atomic layer deposition of lead sulfide quantum dots on nanowire surfaces," *Nano Letters*, vol. 11, no. 3, pp. 934 – 940, 2011.

[57] S. T. Christensen, H. Feng, J. L. Libera, N. Guo, J. T. Miller, P. C. Stair, and J. W. Elam, "Supported Ru-Pt bimetallic nanoparticle catalysts prepared by atomic layer deposition," *Nano Letters*, vol. 10, no. 8, pp. 3047 – 3051, 2010.

[58] M. Knez, K. Nielsch, and L. Niinistö, "Synthesis and surface engineering of complex nanostructures by atomic layer deposition," *Advanced Materials*, vol. 19, no. 21, pp. 3425 – 3438, 2007.

[59] H. Kim, H.-B.-R. Lee, and W.-J. Maeng, "Applications of atomic layer deposition to nanofabrication and emerging nanodevices," *Thin Solid Films*, vol. 517, no. 8, pp. 2563 – 2580, 2009.

[60] X. Jiang and S. F. Bent, "Area-selective atomic layer deposition of platinum on YSZ substrates using microcontact printed SAMs," *Journal of the Electrochemical Society*, vol. 154, no. 12, pp. D648 – D656, 2007.

[61] E. Granneman, P. Fischer, D. Pierreux, H. Terhorst, and P. Zagwijn, "Batch ALD: Characteristics, comparison with single wafer ALD, and examples," *Surface and Coatings Technology*, vol. 201, pp. 8899 – 8907, 2007.

[62] G. M. Sundaram, A. Bertuch, R. Bhatia, R. Coutu, M. Dalberth, E. W. Deguns, G. Liu, M. J. Sowa, and J. S. Becker, "Large format atomic layer deposition," *ECS Transactions*, vol. 33, no. 2, pp. 429 – 440, 2010.

[63] P. Poodt, D. C. Cameron, E. Dickey, S. M. George, V. Kuznetsov, G. N. Parsons, F. Roozeboom, G. Sundaram, and A. Vermeer, "Spatial atomic layer deposition: A route towards further industrialization of atomic layer deposition," *Journal of Vacuum Science and Technology A*, vol. 30, no. 1, p. 010802 (11pp), 2012.

[64] W. M. M. E. Kessels and M. Putkonen, "Advanced process technologies: Plasma, direct-write, atmospheric pressure, and roll-to-roll ALD," *MRS Bulletin*, vol. 36, no. 11, pp. 907 – 913, 2011.

[65] K.-E. Elers, M. Ritala, M. Leskelä, and L.-S. Johansson, "Atomic layer epitaxy growth of AlN thin films," *Journal de Physique IV*, vol. 5, no. C5, pp. 1021 – 1027, 1995.

[66] J. Jokinen, P. Haussalo, J. Keinonen, M. Ritala, D. Riihelä, and M. Leskelä, "Analysis of AlN thin films by combining TOF-ERDA and NRB techniques," *Thin Solid Films*, vol. 289, no. 1 - 2, pp. 159 – 165, 1996.

[67] J. N. Kidder, J. S. Kuo, A. Ludviksson, T. P. Pearsall, J. W. Rogers, J. M. Grant, L. R. Allen, and S. T. Hsu, "Deposition of AlN at lower temperatures by atmospheric metalorganic chemical vapor deposition using dimethylethylamine alane and ammonia," *Journal of Vacuum Science and Technology A*, vol. 13, no. 3, pp. 711 – 715, 1995.

[68] J. N. Kidder, J. S. Kuo, T. P. Pearsall, and J. W. Rogers, "AlN films deposited by LP-MOCVD atomic layer deposition at lower temperatures using DMEAA and ammonia," in *Materials Research Society Symposium Proceedings*, vol. 395, pp. 249 – 254, 1996.

[69] A. Ludviksson, D. W. Robinson, and J. W. Rogers, "The interaction of dimethylethylaminealane and ammonia on clean and oxidized Al(111): Atomic layer growth of aluminum nitride," *Thin Solid Films*, vol. 289, no. 1 - 2, pp. 6 – 13, 1996.

[70] J. N. Kidder, H. K. Yun, J. W. Rogers, and T. P. Pearsall, "Chemical composition of AlN thin films deposited at 523-723 K using dimethylethylamine

alane and ammonia," *Chemistry of Materials*, vol. 10, no. 3, pp. 777 – 783, 1998.

[71] M. A. Khan, J. N. Kuznia, R. A. Skogman, D. T. Olson, M. M. Millan, and W. J. Choyke, "Low pressure metalorganic chemical vapor deposition of AlN over sapphire substrates," *Applied Physics Letters*, vol. 61, no. 21, pp. 2539 – 2541, 1992.

[72] M. A. Khan, J. N. Kuznia, D. T. Olson, T. George, and W. T. Pike, "GaN/AlN digital alloy short-period superlattices by switched atomic layer metalorganic chemical vapor deposition," *Applied Physics Letters*, vol. 63, no. 25, pp. 3470 – 3472, 1993.

[73] T. M. Mayer, J. W. Rogers, and T. A. Michalske, "Mechanism of nucleation and atomic layer growth of AlN on Si," *Chemistry of Materials*, vol. 3, no. 4, pp. 641 – 646, 1991.

[74] M. E. Bartram, T. A. Michalske, J. W. Rogers, and R. T. Paine, "Nucleation and growth of AlN: Self-limiting reactions and the regeneration of active sites using sequential exposures of trimethylaluminum and ammonia on silica at 600 K," *Chemistry of Materials*, vol. 5, no. 10, pp. 1424 – 1430, 1993.

[75] H. Liu, D. C. Bertolet, and J. W. Rogers, "Reactions of trimethylaluminum and ammonia on alumina at 600 K - surface chemical aspects of AlN thin film growth," *Surface Science*, vol. 340, no. 1 - 2, pp. 88 – 100, 1995.

[76] D. Riihelä, M. Ritala, R. Matero, M. Leskelä, and P. H. J. Jokinen, "Low temperature deposition of AlN thin films by an alternate supply of trimethyl aluminum and ammonia," *Chemical Vapor Deposition*, vol. 2, no. 6, pp. 277 – 283, 1996.

[77] F. G. McIntosh, E. L. Piner, J. C. Roberts, M. K. Behbehani, M. Aumer, N. A. El-Masry, and S. M. Bedair, "Epitaxial deposition of GaInN and InN using the rotating susceptor ALE system," *Applied Surface Science*, vol. 112, pp. 98 – 101, 1997.

[78] R. L. Puurunen, A. Root, S. Haukka, E. I. Iiskola, M. Lindblad, and A. O. I. Krause, "IR and NMR study of the chemisorption of ammonia on trimethylaluminum-modified silica," *Journal of Physical Chemistry B*, vol. 104, no. 28, pp. 6599 – 6609, 2000.

[79] R. L. Puurunen, A. Root, P. Sarv, S. Haukka, E. I. Iiskola, M. Lindblad, and A. O. I. Krause, "Growth of aluminum nitride on porous silica by atomic layer chemical vapour deposition," *Applied Surface Science*, vol. 165, no. 2, pp. 193 – 202, 2000.

[80] R. L. Puurunen, M. Lindblad, A. Root, and A. O. I. Krause, "Successive reactions of gaseous trimethylaluminium and ammonia on porous alumina," *Physical Chemistry Chemical Physics*, vol. 3, no. 6, pp. 1093 – 1102, 2001.

[81] R. L. Puurunen, A. Root, P. Sarv, M. M. Viitanen, H. H. Brongersma, M. Lindblad, and A. O. I. Krause, "Growth of aluminum nitride on porous alumina and silica through separate saturated gas-solid reactions of trimethylaluminum and ammonia," *Chemistry of Materials*, vol. 14, no. 2, pp. 720 – 729, 2002.

[82] J. P. Zhang, M. A. Khan, W. H. Sun, H. M. Wang, C. Q. Chen, Q. Fareed, E. Kuokstis, and J. W. Yang, "Pulsed atomic-layer epitaxy of ultrahigh-quality $Al_xGa_{1-x}N$ structures for deep ultraviolet emissions below 230 nm," *Applied Physics Letters*, vol. 81, no. 23, pp. 4392 – 4394, 2002.

[83] X. Liu, S. Ramanathan, E. Lee, and T. E. Seidel, "Low temperature deposition of AlN thin films by an alternate supply of trimethyl aluminum and ammonia," in *Materials Research Society Symposium Proceedings*, vol. 811, pp. 11 – 16, 2004.

[84] M. Badylevich, S. Shamuilia, V. V. Afanas'ev, A. Stesmans, Y. G. Fedorenko, and C. Zhao, "Electronic structure of the interface of aluminum nitride with Si(100)," *Journal of Applied Physics*, vol. 104, no. 9, p. 093713 (4pp), 2008.

[85] L. W. Sang, Z. X. Qin, H. Fang, T. Dai, Z. J. Yang, B. Shen, G. Y. Zhang, X. P. Zhang, J. Xu, and D. P. Yu, "Reduction in threading dislocation

densities in AlN epilayer by introducing a pulsed atomic-layer epitaxial buffer layer," *Applied Physics Letters*, vol. 93, no. 12, p. 122104 (3pp), 2008.

[86] J. Feng, Y. Chen, J. Blair, H. Kurt, R. Hao, D. S. Citrin, C. J. Summers, and Z. Zhou, "Fabrication of annular photonic crystals by atomic layer deposition and sacrificial etching," *Journal of Vacuum Science and Technology B*, vol. 27, no. 2, pp. 568 – 572, 2009.

[87] K. G. Reid, A. Dip, S. Sasaki, D. Triyoso, S. Samavedam, D. Gilmer, and C. F. H. Gondran, "Electrical and materials properties of AlN/ HfO_2 high-k stack with a metal gate," *Thin Solid Films*, vol. 517, no. 8, pp. 2712 – 2718, 2009.

[88] D. Kueck, P. Leber, A. Schmidt, G. Speranza, and E. Kohn, "AlN as passivation for surface channel FETs on H-terminated diamond," *Diamond and Related Materials*, vol. 19, no. 7-9, pp. 932 – 935, 2010.

[89] Y. Zhou, D. M. King, J. Li, K. S. Barrett, R. B. Goldfarb, and A. W. Weimer, "Synthesis of photoactive magnetic nanoparticles with atomic layer deposition," *Industrial and Engineering Chemistry Research*, vol. 49, no. 15, pp. 6964 – 6971, 2010.

[90] H. Liu and J. W. Rogers, "Molecularly engineered low temperature atomic layer growth of aluminum nitride on Si(100)," *Journal of Vacuum Science and Technology A*, vol. 17, no. 2, pp. 325 – 331, 1999.

[91] K. H. Kim, R. G. Gordon, A. Ritenour, and D. A. Antoniadis, "Atomic layer deposition of insulating nitride interfacial layers for germanium metal oxide semiconductor field effect transistors with high-κ oxide/tungsten nitride gate stacks," *Applied Physics Letters*, vol. 90, no. 21, p. 212104 (3pp), 2007.

[92] D. Shahrjerdi, T. Rotter, G. Balakrishnan, D. Huffaker, E. Tutuc, and S. K. Banerjee, "Fabrication of self-aligned enhancement-mode $In_{0.53}Ga_{0.47}As$ MOSFETs with TaN/HfO_2/AlN gate stack," *IEEE Electron Device Letters*, vol. 29, no. 6, pp. 557 – 560, 2008.

[93] G. Liu, E. W. Deguns, L. Lecordier, G. Sundaram, and J. S. Becker, "Atomic layer deposition of AlN with tris(dimethylamido)aluminum and NH_3," *ECS Transactions*, vol. 41, no. 2, pp. 219 – 225, 2011.

[94] C. Lee, C. S. Hwang, and H. J. Kim, "Boron diffusion properties and electrical characteristics of p^+ poly-$Si_{0.73}Ge_{0.27}$/AlN_x/Al_2O_3/AlN_x/n-Si (100) using in-situ ALD," *Integrated Ferroelectrics*, vol. 74, pp. 79 – 85, 2005.

[95] C. Lee, J. Park, M. Cho, S. H. Hong, C. S. Hwang, H. J. Kim, and J. Jeong, "Dopant penetration behavior of B-doped p^+ polycrystalline-$Si_{0.73}Ge_{0.27}$/Al_2O_3 or AlN-Al_2O_3/n-Si metal insulator semiconductor capacitors," *Electrochemical and Solid-State Letters*, vol. 9, no. 3, pp. G84 – G86, 2006.

[96] C. Weiland, A. K. Rumaiz, J. Price, P. Lysaght, and J. C. Woick, "Passivation of $In_{0.53}Ga_{0.47}As$/ZrO_2 interfaces by AlN atomic layer deposition process," *Journal of Applied Physics*, vol. 114, no. 3, p. 034107 (8pp), 2013.

[97] M. Usman, T. Pilvi, M. Leskelä, A. Schöner, and A. Hallén, "Characterization of Al-based high-k stacked dielectric layers deposited on 4H-SiC by atomic layer deposition," *Materials Science Forum*, vol. 679 - 680, pp. 441 – 444, 2011.

[98] M. Usman, A. Hallén, T. Pilvi, A. Schöner, and M. Leskelä, "Toward the understanding of stacked Al-based high-k dielectrics for passivation of 4H-SiC devices," *Journal of the Electrochemical Society*, vol. 158, no. 1, pp. H75 – H79, 2011.

[99] C. L. Dezelah-IV, O. M. El-Kadri, K. Kukli, K. Arstila, R. J. Baird, J. Lu, L. Niinistö, and C. H. Winter, "A low valent metalorganic precursor for the growth of tungsten nitride thin films by atomic layer deposition," *Journal of Materials Chemistry*, vol. 17, no. 11, pp. 1109 – 1116, 2007.

[100] Y. J. Lee and S.-W. Kang, "Ti-Al-N thin films prepared by the combination of metallorganic plasma-enhanced atomic layer deposition of Al and TiN," *Electrochemical and Solid-State Letters*, vol. 6, no. 5, pp. C70 – C72, 2003.

[101] Y. J. Lee and S.-W. Kang, "Controlling the composition of $Ti_{1-x}Al_xN$ thin films by modifying the number of TiN and AlN subcycles in atomic layer deposition," *Journal of Vacuum Science and Technology A*, vol. 21, no. 5, pp. L13 – L15, 2003.

[102] Y. J. Lee and S.-W. Kang, "Antioxidation properties of $Ti_{0.83}Al_{0.17}N$ prepared using plasma-enhanced atomic layer deposition," *Applied Physics Letters*, vol. 86, no. 7, p. 071919 (3pp), 2005.

[103] J. W. Lim and S. J. Yun, "Insulators with high stability for electroluminescent devices," *Japanese Journal of Applied Physics - Part 2*, vol. 42, no. 6B, pp. L663 – L665, 2003.

[104] J. W. Lim and S. J. Yun, "Electrical properties of alumina films by plasma-enhanced atomic layer deposition," *Electrochemical and Solid-State Letters*, vol. 7, no. 8, pp. F45 – F48, 2004.

[105] S. J. Yun, Y.-W. Ko, and J. W. Lim, "Passivation of organic light-emitting diodes with aluminum oxide thin films grown by plasma-enhanced atomic layer deposition," *Applied Physics Letters*, vol. 85, no. 21, pp. 4896 – 4898, 2004.

[106] Y. J. Lee and S.-W. Kang, "Growth of aluminum nitride thin films prepared by plasma-enhanced atomic layer deposition," *Thin Solid Films*, vol. 446, no. 2, pp. 227 – 231, 2004.

[107] Y. J. Lee, "Formation of aluminum nitride thin films as gate dielectrics on Si (1 0 0)," *Journal of Crystal Growth*, vol. 266, no. 4, pp. 568 – 572, 2004.

[108] D. Eom, S. Y. No, C. S. Hwang, and H. J. Kim, "Properties of aluminum nitride thin films deposited by an alternate injection of trimethylaluminum and ammonia under ultraviolet radiation," *Journal of the Electrochemical Society*, vol. 153, no. 4, pp. C229 – C234, 2006.

[109] K.-H. Kim, N.-W. Kwak, and S. H. Lee, "Fabrication and properties of AlN film on GaN substrate by using remote plasma atomic layer deposition method," *Electronic Materials Letters*, vol. 5, no. 2, pp. 83 – 86, 2009.

[110] S. Jeon and S. Park, "Fabrication of robust triple-$Ti_{1-x}Al_xN$ metal gate by atomic layer deposition," *Journal of the Electrochemical Society*, vol. 157, no. 12, pp. H1101 – H1105, 2010.

[111] Y.-R. Shin, W.-S. Kwack, Y. C. Park, J.-H. Kim, S.-Y. Shin, K. I. Moon, H.-W. Lee, and S.-H. Kwon, "Structural and electrical properties of ternary Ru-AlN thin films prepared by plasma-enhanced atomic layer deposition," *Materials Research Bulletin*, vol. 47, no. 3, pp. 790 – 793, 2012.

[112] M. Bosund, T. Sajavaara, M. Laitinen, T. Huhtio, M. Putkonen, V.-M. Airaksinen, and H. Lipsanen, "Properties of AlN grown by plasma enhanced atomic layer deposition," *Applied Surface Science*, vol. 257, no. 17, pp. 7827 – 7830, 2011.

[113] A. P. Perros, H. Hakola, T. Sajavaara, T. Huhtio, and H. Lipsanen, "Influence of plasma chemistry on impurity incorporation in AlN prepared by plasma enhanced atomic layer deposition," *Journal of Physics D: Applied Physics*, vol. 46, no. 50, p. 505502 (8pp), 2013.

[114] W. Lei and Q. Chen, "Crystal AlN deposited at low temperature by magnetic field enhanced plasma assisted atomic layer deposition," *Journal of Vacuum Science and Technology A*, vol. 31, no. 1, p. 01A114 (7pp), 2013.

[115] N. Nepal, S. B. Qadri, J. K. Hite, N. A. Mahadik, M. A. Mastro, and J. R. Eddy, "Epitaxial growth of AlN films via plasma-assisted atomic layer epitaxy," *Applied Physics Letters*, vol. 103, no. 8, p. 082110 (5pp), 2013.

[116] B. J. Choi, J. J. Yang, M.-X. Zhang, K. J. Norris, D. A. A. Ohlberg, N. P. Kobayashi, G. Medeiros-Ribeiro, and R. S. Williams, "Nitride memristors," *Applied Physics A: Materials Science and Processing*, vol. 109, no. 1, pp. 1 – 4, 2012.

[117] K. J. Chen, S. Huang, and Q. Jiang, "Low dynamic ON-resistance in AlGaN/GaN-on-Si power HEMTs obtained by AlN thin film passivation," *ECS Transactions*, vol. 50, no. 3, pp. 343 – 351, 2012.

[118] S. Huang, Q. Jiang, S. Yang, C. Zhou, and K. J. Chen, "Effective passivation of AlGaN/GaN HEMTs by ALD-grown AlN thin film," *IEEE Electron Device Letters*, vol. 33, no. 4, pp. 516 – 518, 2012.

[119] S. Huang, Q. Jiang, S. Yang, Z. Tang, and K. J. Chen, "Mechanism of PEALD-grown AlN passivation for AlGaN/GaN HEMTs: Compensation of interface traps by polarization charges," *IEEE Electron Device Letters*, vol. 34, no. 2, pp. 193 – 195, 2013.

[120] Z. Tang, S. Huang, Q. Jiang, S. Liu, C. Liu, and K. J. Chen, "High-voltage (600-V) low-leakage low-current-collapse AlGaN/GaN HEMTs with AlN/SiN_x passivation," *IEEE Electron Device Letters*, vol. 34, no. 3, pp. 366 – 368, 2013.

[121] C. Liu, S. Liu, S. Huang, and K. J. Chen, "Plasma-enhanced atomic layer deposition of AlN epitaxial thin film for AlN/GaN heterostructure TFTs," *IEEE Electron Device Letters*, vol. 34, no. 9, pp. 1106 – 1108, 2013.

[122] K. J. Chen and S. Huang, "AlN passivation by plasma-enhanced atomic layer deposition for GaN-based power switches and power amplifiers," *Semiconductor Science and Technology*, vol. 28, no. 7, p. 074015 (8pp), 2013.

[123] Y.-H. Hwang, L. Liu, C. Velez, F. Ren, B. P. Gila, D. Hays, S. J. Pearton, E. Lambers, I. I. Kravchenko, C.-F. Lo, and J. W. Johnson, "GaN metal-insulator-semiconductor high-electron-mobility transistor with plasma enhanced atomic layer deposited AlN as gate dielectric and passivation," *Journal of Vacuum Science and Technology B*, vol. 31, no. 5, p. 052201 (4pp), 2013.

[124] A. D. Koehler, N. Nepal, T. J. Anderson, M. J. Tadjer, K. D. Hobart, C. R. Eddy, and F. J. Kub, "Atomic layer epitaxy AlN for enhanced AlGaN/GaN HEMT passivation," *IEEE Electron Device Letters*, vol. 34, no. 9, pp. 1115 – 1117, 2013.

[125] M. Schmidt, C. P. Lu, H. D. B. Gottlob, and H. Kurz, "Metal gate electrodes for rare earth oxide high-k dielectrics," in *Proceedings of 3rd International Conference on Signals, Circuits and Systems*, p. 5412230 (5pp), 2009.

[126] C.-P. Lu, M. Schmidt, H. D. B. Gottlob, and H. Kurz, "Integration of ALD AlN work function tuning layers," in *Proceedings of 2010 International Symposium on VLSI Technology, System and Application*, pp. 92 – 93, 2010.

[127] M. Bosund, P. Mattila, A. Aierken, T. Hakkarainen, H. Koskenvaara, M. Sopanen, V.-M. Airaksinen, and H. Lipsanen, "GaAs surface passivation by plasma-enhanced atomic-layer-deposited aluminum nitride," *Applied Surface Science*, vol. 256, no. 24, pp. 7434 – 7437, 2010.

[128] H. Jussila, P. Mattila, J. Oksanen, A. Perros, J. Riikonen, M. Bosund, A. Varpula, T. Huhtio, H. Lipsanen, and M. Sopanen, "High-k GaAs metal insulator semiconductor capacitors passivated by *ex-situ* plasma-enhanced atomic layer deposited AlN for Fermi-level unpinning," *Applied Physics Letters*, vol. 100, no. 7, p. 071606 (4pp), 2012.

[129] P. Mattila, M. Bosund, H. Jussila, T. Tuomi, J. Riikonen, T. Huhtio, H. Lipsanen, and M. Sopanen, "Effect of atomic-layer-deposited AlN on near-surface InGaAs/GaAs structures," *Physica Status Solidi (C)*, vol. 9, no. 7, pp. 1560 – 1562, 2012.

[130] P. Mattila, M. Bosund, T. Huhtio, H. Lipsanen, and M. Sopanen, "Comparison of ammonia plasma and AlN passivation by plasma-enhanced atomic layer deposition," *Journal of Applied Physics*, vol. 111, no. 6, p. 063511 (4pp), 2012.

[131] S. Huang, K. Wei, Z. Tang, S. Yang, C. Liu, L. Guo, B. Shen, J. Zhang, X. Kong, G. Liu, Y. Zheng, X. Liu, and K. J. Chen, "Effects of interface oxidation on the transport behavior of the two-dimensional-electron-gas in AlGaN/GaN heterostructures by plasma-enhanced-atomic-layer-deposited AlN passivation," *Journal of Applied Physics*, vol. 114, no. 14, p. 144509 (6pp), 2013.

[132] A. Perros, M. Bosund, T. Sajavaara, M. Laitinen, L. Sainiemi, T. Huhtio, and H. Lipsanen, "Plasma etch characteristics of aluminum nitride mask layers grown by low-temperature plasma enhanced atomic layer deposition in SF_6 based plasmas," *Journal of Vacuum Science and Technology A*, vol. 30, no. 1, p. 011504 (5pp), 2012.

[133] W.-C. Choi, Z. Wan, J.-H. Ahn, D.-I. Kim, S.-Y. Shin, K.-I. Moon, J.-S. Park, J.-D. Kwon, and S.-H. Kwon, "Multifunctional Ru-AlN heating resistor films for high efficiency inkjet printhead," *Journal of Electroceramics*, article in press.

[134] M. A. Khan, R. A. Skogman, J. M. van Hove, D. T. Olson, and J. N. Kuznia, "Atomic layer epitaxy of GaN over sapphire using switched metalorganic chemical vapor deposition," *Applied Physics Letters*, vol. 60, no. 11, pp. 1366 – 1368, 1992.

[135] M. A. Khan, J. N. Kuznia, D. T. Olson, J. M. van Hove, M. Blasingame, and L. F. Reitz, "High-responsivity photoconductive ultraviolet sensors based on insulating single-crystal GaN epilayers," *Applied Physics Letters*, vol. 60, no. 23, pp. 2917 – 2919, 1992.

[136] C.-Y. Hwang, P. Lu, W. E. Mayo, Y. Lut, and H. Liut, "Characterization of gallium nitride grown on (0001) sapphire by plasma-enhanced atomic layer epitaxy," in *Materials Research Society Symposium Proceedings*, vol. 326, pp. 347 – 352, 1994.

[137] N. H. Karam, T. Parodos, P. Colter, D. McNulty, W. Rowland, J. Schetzina, N. El-Masry, and S. M. Bedair, "Growth of device quality GaN at 550 °c by atomic layer epitaxy," *Applied Physics Letters*, vol. 67, no. 1, pp. 94 – 96, 1995.

[138] K. S. Boutros, J. C. Roberts, F. G. McIntosh, E. L. Piner, N. A. El-Masry, and S. M. Bedair, "Low-temperature growth of high quality $In_xGa_{1-x}N$ by atomic layer epitaxy," in *Materials Research Society Symposium Proceedings*, vol. 395, pp. 213 – 218, 1996.

[139] S.-C. Huang, H.-Y. Wang, C.-J. Hsu, J.-R. Gong, C.-I. Chiang, S.-L. Tu, and H. Chang, "Growth of wurtzite GaN on (0 0 1) GaAs substrates at low temperature by atomic layer epitaxy," *Journal of Materials Science Letters*, vol. 17, no. 15, pp. 1281 – 1285, 1998.

[140] H. Y. Wang, S. C. Huang, T. Y. Yan, J. R. Gong, T. Y. Lin, and Y. F. Chen, "Growth and characterization of GaN films on (0001) sapphire substrates by alternate supply of trimethylgallium and NH_3," *Materials Science and Engineering B*, vol. 57, no. 3, pp. 218 – 223, 1999.

[141] J. Dai, Z. Wu, X. Han, Q. He, Y. Sun, C. Yu, L. Zhang, L. Tong, Y. Gao, and C. Chen, "High quality *a*-plane GaN layers grown by pulsed atomic-layer epitaxy on *r*-plane sapphire substrates," in *Proceedings of SPIE - The International Society for Optical Engineering*, vol. 7279, p. 72791B (6pp), 2009.

[142] H. Tsuchiya, M. Akamatsu, M. Ishida, and F. Hasegawa, "Layer-by-layer growth of GaN on GaAs substrates by alternate supply of $GaCl_3$ and NH_3," *Japanese Journal of Applied Physics - Part 2*, vol. 35, no. 6B, pp. L748 – L750, 1996.

[143] O. H. Kim, D. Kim, and T. Anderson, "Atomic layer deposition of GaN using $GaCl_3$ and NH_3," *Journal of Vacuum Science and Technology A*, vol. 27, no. 4, pp. 923 – 928, 2009.

[144] A. Koukitu, Y. Kumagai, T. Taki, and H. Seki, "Halogen-transport atomic-layer epitaxy of cubic GaN monitored by *in situ* gravimetric method," *Japanese Journal of Applied Physics - Part 1*, vol. 38, no. 9A, pp. 4980 – 4982, 1999.

[145] Y. Kumagai, M. Mayumi, A. Koukitu, and H. Seki, "In situ gravimetric monitoring of halogen transport atomic layer epitaxy of cubic-GaN," *Applied Surface Science*, vol. 159 - 160, pp. 427 – 431, 2000.

[146] J. Sumakeris, Z. Sitar, K. S. Ailey-Trent, K. L. More, and R. F. Davis, "Layer-by-layer epitaxial growth of GaN at low temperatures," *Thin Solid Films*, vol. 225, no. 1 - 2, pp. 244 – 249, 1993.

[147] T. R. Sharp, A. K. Peter, C. J. Hodson, B. MacKenzie, C. Pugh, M. Loveday, and R. Gunn, "Plasma-enhanced ALD and analysis of GaN deposited from triethyl gallium and H_2/N_2 plasma," presented at the 13th International Conference on Atomic Layer Deposition, July 2013.

[148] M. H. Lo, Z. Y. Li, J. R. Chen, T. S. Ko, T. C. Lu, H. C. Kuo, and S. C. Wang, "AlGaN/GaN multiple quantum wells grown by atomic layer deposition," in *Proceedings of SPIE - The International Society for Optical Engineering*, vol. 6894, p. 68941V (9pp), 2008.

[149] K. S. Boutros, F. G. McIntosh, J. C. Roberts, S. M. Bedair, E. L. Piner, and N. A. El-Masry, "High quality InGaN films by atomic layer epitaxy," *Applied Physics Letters*, vol. 67, no. 13, pp. 1856 – 1858, 1995.

[150] E. L. Piner, F. G. McIntosh, J. C. Roberts, K. S. Boutros, M. E. Aumer, V. A. Joshkin, N. A. El-Masry, S. M. Bedair, and S. X. Liu, "A model for indium incorporation in the growth of InGaN films," in *Materials Research Society Symposium Proceedings*, vol. 449, pp. 85 – 88, 1997.

[151] E. L. Piner, M. K. Behbehani, N. A. El-Masry, F. G. McIntosh, J. C. Roberts, K. S. Boutros, and S. M. Bedair, "Effect of hydrogen on the indium incorporation in InGaN epitaxial films," *Applied Physics Letters*, vol. 70, no. 4, pp. 461 – 463, 1997.

[152] C. Adelmann, E. Matinez-Guerrero, J. Barjon, J. Brault, L. S. Dang, H. Mariette, G. Mula, and B. Daudin, "Atomic layer epitaxy of hexagonal and cubic GaN nanostructures," *Physica Status Solidi (A)*, vol. 188, no. 2, pp. 673 – 676, 2001.

[153] C. Adelmann, J. Brault, J.-L. Rouvire, H. Mariette, G. Mula, and B. Daudin, "Atomic-layer epitaxy of GaN quantum wells and quantum dots on (0001) AlN," *Journal of Applied Physics*, vol. 91, no. 8, pp. 5498 – 5500, 2002.

[154] K. Higuchi, A. Unno, and T. Shiraishi, "A possibility of ALE growth of InN by using $InCl_3$," in *Materials Research Society Symposium Proceedings*, vol. 222, pp. 169 – 173, 1991.

[155] T. Inushima, T. Yaguchi, A. Nagase, A. Iso, T. Shiraishi, and S. Ooya, "Optical and electrical properties of InN grown by the atomic layer epitaxy," in *Conference Proceedings - Seventh International Conference on Indium Phosphide and Related Materials*, pp. 187 – 190, 1995.

[156] T. Inushima, T. Shiraishi, and V. Y. Davydov, "Phonon structure of InN grown by atomic layer epitaxy," *Solid State Communications*, vol. 110, no. 9, pp. 491 – 495, 1999.

[157] S. M. Bedair, F. G. McIntosh, J. C. Roberts, E. L. Piner, K. S. Boutros, and N. A. El-Masry, "Growth and characterization of In-based nitride compounds," *Journal of Crystal Growth*, vol. 178, no. 1 - 2, pp. 32 – 44, 1997.

[158] N. Nepal, N. A. Mahadik, L. O. Nyakiti, S. B. Qadri, M. J. Mehl, J. K. Hite, and C. R. Eddy, "Epitaxial growth of cubic and hexagonal InN thin films via plasma-assisted atomic layer epitaxy," *Crystal Growth and Design*, vol. 13, no. 4, pp. 1485 – 1490, 2013.

[159] V. N. Tondare, C. Balasubramanian, S. V. Shende, D. S. Joag, V. P. Godbole, S. V. Bhoraskar, and M. Bhadbhade, "Field emission from open ended aluminum nitride nanotubes," *Applied Physics Letters*, vol. 80, no. 25, pp. 4813 – 4815, 2002.

[160] Q. Wu, Z. Hu, X. Wang, Y. Lu, X. Chen, H. Xu, and Y. Chen, "Synthesis and characterization of faceted hexagonal aluminum nitride nanotubes," *Journal of the American Chemical Society*, vol. 125, no. 34, pp. 10176 – 10177, 2003.

[161] L.-W. Yin, Y. Bando, Y.-C. Zhu, D. Golberg, and M. S. Li, "A two-stage route to coaxial cubic-aluminum-nitrideboron-nitride composite nanotubes," *Advanced Materials*, vol. 16, no. 11, pp. 929 – 933, 2004.

[162] H. Morito, T. Ide, T. Karahashi, H. Orikasa, T. Yamada, and H. Yamane, "Synthesis of an AlN polycrystalline bulk layer and nanotubes by using NH_3 and Bi," *Journal of the American Ceramic Society*, vol. 92, no. 11, pp. 2578 – 2582, 2009.

[163] R. Thapa, B. Saha, N. S. Das, U. N. Maiti, and K. K. Chattopadhyay, "Self filling of Ni nanoparticles in amorphous AlN nanotubes and its field emission property," *Applied Surface Science*, vol. 256, no. 12, pp. 3988 – 3992, 2010.

[164] Y. Fan, "Formation of crystalline AlN nanotubes by a roll-up approach," *Materials Letters*, vol. 65, no. 12, pp. 1900 – 1902, 2011.

[165] Y. Sun, J. Y. Li, Y. Tan, and L. Zhang, "Fabrication of aluminum nitride (AlN) hollow fibers by carbothermal reduction and nitridation of electrospun precursor fibers," *Journal of Alloys and Compounds*, vol. 471, no. 1-2, pp. 400 – 403, 2009.

[166] Z. Zhou, J. Zhao, Y. Chen, P. von Ragué Schleyer, and Z. Chen, "Energetics and electronic structures of AlN nanotubes/wires and their potential application as ammonia sensors," *Nanotechnology*, vol. 18, no. 42, p. 424023 (7pp), 2007.

[167] A. Ahmadi, N. L. Hadipour, M. Kamfiroozi, and Z. Bagheri, "Theoretical study of aluminum nitride nanotubes for chemical sensing of formaldehyde," *Sensors and Actuators B: Chemical*, vol. 161, no. 1, pp. 1025 – 1029, 2012.

[168] L.-W. Yin, Y. Bando, Y. C. Zhu, M.-S. Li, C.-C. Tang, and D. Goldberg, "Single-crystalline AlN nanotubes with carbon-layer coatings on the outer and inner surfaces via a multiwalled-carbon-nanotube-template-induced route," *Advanced Materials*, vol. 17, no. 2, pp. 213 – 217, 2005.

[169] G. Stan, C. V. Ciobanu, T. P. Thayer, G. T. Wang, J. R. Creighton, K. P. Purushotham, L. A. Bendersky, and R. F. Cook, "Elastic moduli of faceted aluminum nitride nanotubes measured by contact resonance atomic force microscopy," *Nanotechnology*, vol. 20, no. 3, p. 035706 (6pp), 2009.

[170] A. Greiner and J. H. Wendorff, "Electrospinning: A fascinating method for the preparation of ultrathin fibers," *Angewandte Chemie International Edition*, vol. 46, no. 30, pp. 5670 – 5703, 2007.

[171] Q. Peng, X.-Y. Sun, J. C. Spagnola, G. K. Hyde, R. J. Spontak, and G. N. Parsons, "Atomic layer deposition on electrospun polymer fibers as a direct route to Al_2O_3 microtubes with precise wall thickness control," *Nano Letters*, vol. 7, no. 3, pp. 719 – 722, 2007.

[172] I. Donmez, F. Kayaci, C. Ozgit-Akgun, T. Uyar, and N. Biyikli, "Fabrication of hafnia hollow nanofibers by atomic layer deposition using electrospun nanofiber templates," *Journal of Alloys and Compounds*, vol. 559, pp. 146 – 151, 2013.

[173] B.-S. Lee, W.-S. Kim, D.-H. Kim, H.-C. Kim, S.-H. Hong, and W.-R. Yu, "Fabrication of SnO_2 nanotube microyarn and its gas sensing behavior," *Smart Materials and Structures*, vol. 20, no. 10, p. 105019 (7pp), 2011.

[174] W.-S. Kim, B.-S. Lee, D.-H. Kim, H.-C. Kim, W.-R. Yu, and S.-H. Hong, "SnO_2 nanotubes fabricated using electrospinning and atomic layer deposition and their gas sensing performance," *Nanotechnology*, vol. 21, no. 24, p. 245605 (7pp), 2010.

[175] G.-M. Kim, S.-M. Lee, G. H. Michler, H. Roggendorf, U. Gösele, and M. Knez, "Nanostructured pure anatase titania tubes replicated from electrospun polymer fiber templates by atomic layer deposition," *Chemistry of Materials*, vol. 20, no. 9, pp. 3085 – 3091, 2008.

[176] S.-W. Choi, J. Y. Park, C. Lee, J. G. Lee, and S. Kim, "Synthesis of highly crystalline hollow TiO_2 fibers using atomic layer deposition on polymer templates," *Journal of the American Ceramic Society*, vol. 94, no. 7, pp. 1974 – 1977, 2011.

[177] J. Y. Park, S.-W. Choi, and S. S. Kim, "A synthesis and sensing application of hollow ZnO nanofibers with uniform wall thicknesses grown using polymer templates," *Nanotechnology*, vol. 21, no. 47, p. 475601 (9pp), 2010.

[178] S. Cho, D.-H. Kim, B.-S. Lee, J. Jung, W.-R. Yu, S.-H. Hong, and S. Lee, "Ethanol sensors based on ZnO nanotubes with controllable wall thickness

via atomic layer deposition, an O_2 plasma process and an annealing process," *Sensors and Actuators B: Chemical*, vol. 162, no. 1, pp. 300 – 306, 2012.

[179] E. Santala, M. Kemell, M. Leskelä, and M. Ritala, "The preparation of reusable magnetic and photocatalytic composite nanofibers by electrospinning and atomic layer deposition," *Nanotechnology*, vol. 20, no. 3, p. 035602 (5pp), 2009.

[180] J. Y. Park, S.-W. Choi, J.-W. Lee, C. Lee, and S. S. Kim, "Synthesis and gas sensing properties of TiO_2-ZnO core-shell nanofibers," *Journal of the American Ceramic Society*, vol. 92, no. 11, pp. 2551 – 2554, 2009.

[181] S.-W. Choi, J. Y. Park, and S. S. Kim, "Synthesis of SnO_2-ZnO core-shell nanofibers via a novel two-step process and their gas sensing properties," *Nanotechnology*, vol. 20, no. 46, p. 465603 (6pp), 2009.

[182] Q. Peng, X.-Y. Sun, J. C. Spagnola, C. Saquing, S. A. Khan, R. J. Spontak, and G. N. Parsons, "Bi-directional Kirkendall effect in coaxial microtube nanolaminate assemblies fabricated by atomic layer deposition," *ACS Nano*, vol. 3, no. 3, pp. 546 – 554, 2009.

[183] J. R. Mileham, S. J. Pearton, C. R. Abernathy, J. D. MacKenzie, R. J. Shul, and S. P. Kilcoyne, "Wet chemical etching of AlN," *Applied Physics Letters*, vol. 67, no. 8, pp. 1119 – 1121, 1995.

[184] M. Rose, J. W. Bartha, and I. Endler, "Temperature dependence of the sticking coefficient in atomic layer deposition," *Applied Surface Science*, vol. 256, no. 12, pp. 3778 – 3782, 2010.

[185] C. C. Wang, M. C. Chiu, M. H. Shiao, and F. S. Shieu, "Characterization of AlN thin films prepared by unbalanced magnetron sputtering," *Journal of the Electrochemical Society*, vol. 151, no. 10, pp. F252 – F256, 2004.

[186] L. Rosenberger, R. Baird, E. McCullen, G. Auner, and G. Shreve, "XPS analysis of aluminum nitride films deposited by plasma source molecular beam epitaxy," *Surface and Interface Analysis*, vol. 40, no. 9, pp. 1254 – 1261, 2008.

[187] D. Manova, V. Dimitrova, W. Fukarek, and D. Karpuzov, "Investigation of d.c.-reactive magnetron-sputtered AlN thin films by electron microprobe analysis, X-ray photoelectron spectroscopy and polarised infra-red reflection," *Surface and Coatings Technology*, vol. 106, no. 2-3, pp. 205 – 208, 1998.

[188] H. M. Liao, R. N. S. Sodhi, and T. W. Coyle, "Surface composition of AlN powders studied by X-ray photoelectron spectroscopy and bremsstrahlung-excited Auger electron spectroscopy," *Journal of Vacuum Science and Technology A*, vol. 11, no. 5, pp. 2681 – 2686, 1993.

[189] H. C. Barshilia, B. Deepthi, and K. S. Rajam, "Growth and characterization of aluminum nitride coatings prepared by pulsed-direct current reactive unbalanced magnetron sputtering," *Thin Solid Films*, vol. 516, no. 12, pp. 4168 – 4174, 2008.

[190] M. Strassburg, J. Senawiratne, N. Dietz, U. Haboeck, A. Hoffmann, V. Noveski, R. Dalmau, R. Schlesser, and Z. Sitar, "The growth and optical properties of large, high-quality AlN single crystals," *Journal of Applied Physics*, vol. 96, no. 10, pp. 5870 – 5876, 2004.

[191] P. Lu, R. Collazo, R. F. Dalmau, G. Durkaya, N. Dietz, and Z. Sitar, "Different optical absorption edges in AlN bulk crystals grown in m- and c-orientations," *Applied Physics Letters*, vol. 93, no. 13, p. 131922 (3pp), 2008.

[192] R. F. Pierret, *Semiconductor Device Fundamentals*. Reading, Massachusetts: Addison-Wesley, 1996.

[193] C. L. Aardahl, J. W. Rogers, H. K. Yun, Y. Ono, D. J. Tweet, and S.-T. Hsu, "Electrical properties of AlN thin films deposited at low temperature on Si (100)," *Thin Solid Films*, vol. 346, no. 1, pp. 174 – 180, 1999.

[194] J. P. Kar, G. Bose, and S. Tuli, "Correlation of electrical and morphological properties of sputtered aluminum nitride films with deposition temperature," *Current Applied Physics*, vol. 6, no. 5, pp. 873 – 876, 2006.

[195] V. Dimitrova, D. Manova, and E. Valcheva, "Optical and dielectric properties of dc magnetron sputtered AlN thin films correlated with deposition conditions," *Materials Science and Engineering B: Solid-State Materials for Advanced Technology*, vol. 68, no. 1, pp. 1 – 4, 1999.

[196] M. C. Shih, C. W. Liang, and P. J. Chaing, "Deposition of aluminum nitride thin film on Si(1 1 1) by KrF excimer laser and its characterizations," *Applied Surface Science*, vol. 254, no. 8, pp. 2211 – 2215, 2008.

[197] B. Abdallah, S. Al-Khawaja, and A. Alkhawwam, "Electrical characteristics of insulating aluminum nitride MIS nanostructures," *Applied Surface Science*, vol. 258, no. 1, pp. 419 – 424, 2011.

[198] M. Alevli, C. Ozgit, I. Donmez, and N. Biyikli, "Structural properties of AlN films deposited by plasma-enhanced atomic layer deposition at different growth temperatures," *Physica Status Solidi (A)*, vol. 209, no. 2, pp. 266 – 271, 2012.

[199] M. Alevli, C. Ozgit, and I. Donmez, "The influence of growth temperature on the properties of AlN films grown by atomic layer deposition," *Acta Physica Polonica A*, vol. 120, no. 6A, pp. A58 – A60, 2012.

[200] M. Alevli, C. Ozgit, I. Donmez, and N. Biyikli, "Optical properties of AlN thin films grown by plasma enhanced atomic layer deposition," *Journal of Vacuum Science and Technology A*, vol. 30, no. 2, p. 021506 (6pp), 2012.

[201] Z. M. Huang, Y. Z. Zhang, M. Kotaki, and S. Ramakrishna, "A review on polymer nanofibers by electrospinning and their applications in nanocomposites," *Composites Science and Technology*, vol. 63, no. 15, pp. 2223 – 2253, 2003.

[202] T. Uyar and F. Besenbacher, "Electrospinning of uniform polystyrene fibers: The effect of solvent conductivity," *Polymer*, vol. 49, no. 24, pp. 5336 – 5343, 2008.

[203] I. Donmez, C. Ozgit, and N. Biyikli, "Low temperature deposition of Ga_2O_3 thin films using trimethylgallium and oxygen plasma," *Journal of Vacuum Science and Technology A*, vol. 31, no. 1, p. 01A110 (4pp), 2013.

[204] K. S. A. Butcher, Afifuddin, P. P.-T. Chen, and T. L. Tansley, "Studies of the plasma related oxygen contamination of gallium nitride grown by remote plasma enhanced chemical vapour deposition," *Physica Status Solidi (C)*, vol. 0, no. 1, pp. 156 – 160, 2002.

[205] I. Donmez, "Atomic layer deposition of metal oxide thin films and nanostructures," Master's thesis, Bilkent University, 2013.

[206] M. Sowa, February 2013. Private communication.

[207] G. Yu, G. Wang, H. Ishikawa, M. Umeno, T. Soga, T. Egawa, J. Watanabe, and T. Jimbo, "Optical properties of wurtzite structure GaN on sapphire around fundamental absorption edge (0.78-4.77 eV) by spectroscopic ellipsometry and the optical transmission method," *Applied Physics Letters*, vol. 70, no. 24, pp. 3209 – 3211, 1997.

[208] K. S. A. Butcher, T. L. Tansley, and X. Li, "X-ray photoelectron spectroscopy depth profiling of aluminium nitride thin films," *Surface and Interface Analysis*, vol. 25, no. 2, pp. 99 – 104, 1997.

[209] K. S. A. Butcher, Afifuddin, T. L. Tansley, N. Brack, P. J. Pigram, H. Timmers, K. E. Prince, and R. G. Elliman, "Gallium and oxygen accumulations on gallium nitride surfaces following argon ion milling in ultra-high vacuum conditions," *Applied Surface Science*, vol. 230, no. 1-4, pp. 18 – 23, 2004.

[210] J. Mayer, L. A. Giannuzzi, T. Kamino, and J. Michael, "TEM sample preparation and FIB-induced damage," *MRS Bulletin*, vol. 32, no. 5, pp. 400 – 407, 2007.

[211] S. D. Wolter, B. P. Luther, D. L. Waltemyer, C. Önneby, and S. E. Mohney, "X-ray photoelectron spectroscopy and x-ray diffraction study of the thermal oxide on gallium nitride," *Applied Physics Letters*, vol. 70, no. 16, pp. 2156 – 2158, 1997.

[212] V. Matolín, S. Fabík, J. Glosík, L. Bideux, Y. Ould-Metidji, and B. Gruzza, "Experimental system for GaN thin films growth and in situ characterisation by electron spectroscopic methods," *Vacuum*, vol. 76, no. 4, pp. 471 – 476, 2004.

[213] P. Kumar, M. Kumar, Govind, B. R. Mehta, and S. M. Shivaprasad, "XPS investigation of ion beam induced conversion of GaAs(0 0 1) surface into GaN overlayer," *Applied Surface Science*, vol. 256, no. 2, pp. 517 – 520, 2009.

[214] W. R. L. Lambrecht, B. Segall, S. Strite, G. Martin, A. Agarwal, H. Morkoç, and A. Rockett, "X-ray photoelectron spectroscopy and theory of the valence band and semicore Ga 3d states in GaN," *Physical Review B*, vol. 50, no. 19, pp. 14155 – 14160, 1994.

[215] Z. Majlinger, A. Bozanic, M. Petravic, K.-J. Kim, B. Kim, and Y.-W. Yang, "NEXAFS and XPS study of GaN formation on ion-bombarded GaAs surfaces," *Vacuum*, vol. 84, no. 1, pp. 41 – 44, 2010.

[216] G. Moldovan, I. Harrison, M. Roe, and P. D. Brown, "Correlation of electrical and structural properties of Au contacts to KOH treated n-GaN," in *Institute of Physics Conference Series*, vol. 179, pp. 115 – 118, 2004.

[217] R. Carin, J. P. Deville, and J. Werckmann, "An XPS study of GaN thin films on GaAs," *Surface and Interface Analysis*, vol. 16, no. 1-12, pp. 65 – 69, 1990.

[218] M. E. Levinshtein, S. L. Rumyantsev, and M. S. Shur, *Properties of Advanced Semiconductor Materials*. New York: Wiley, 2001.

[219] M. A. Moram and M. E. Vickers, "X-ray diffraction of III-nitrides," *Reports on Progress in Physics*, vol. 72, no. 3, p. 036502 (40pp), 2009.

[220] W. Rindner and E. Pittelli, "Effects of stress-induced band-gap widening and defects in GaAs junctions," *Journal of Applied Physics*, vol. 37, no. 12, pp. 4437 – 4439, 1966.

[221] A. N. Preschilla, S. Major, N. Kumar, I. Samajdar, and R. S. Srinivasa, "Nanocrystalline gallium nitride thin films," *Applied Physics Letters*, vol. 77, no. 12, pp. 1861 – 1863, 2000.